Title

Structure and Function in Normal and Diseased S-cone Photoreceptor Pathway

Author

Wang, Yiyi

Publication Date

2024

Structure and Function in Normal and Diseased S-cone Photoreceptor Pathway

By

Yiyi Wang

A dissertation submitted in partial satisfaction of the
requirements for the degree of
Doctor of Philosophy
in
Vision Science
in the
Graduate Division
of the
University of California, Berkeley

Committee in charge:
Professor William S. Tuten, Co-Chair
Professor Austin Roorda, Co-Chair
Professor John G. Flannery
Professor Susana Chung

Summer 2024

Abstract

Structure and Function in Normal and Diseased S-cone Photoreceptor Pathway

By

Yiyi Wang

Doctor of Philosophy in Vision Science

University of California, Berkeley

Professors William Tuten & Austin Roorda, Co-Chairs

Short-wavelength-sensitive cones, known as S-cones, constitute a small fraction (5-10%) of the photoreceptors in the human retina, playing crucial roles in color vision and regulating circadian rhythms. While their distribution is coarse, they hold potential as biomarkers for detecting structural and functional changes in retinal diseases. However, our understanding of S-cone topography remains limited, with only a few studies using histology and high-resolution imaging to explore their foveal distribution and role in supporting spatial resolution, particularly in conditions like Enhanced S-cone Syndrome. This dissertation includes three projects that share a common goal of furthering the understanding of the S-cone topography and function in healthy and diseased eyes.

The first study investigated S-cone-mediated acuity in subjects with Enhanced S-cone syndrome (ESCS), serving as a model to elucidate adaptive mechanisms to abnormally distributed photoreceptors during retinal development. By comparing S-cone acuity between ESCS subjects and normal individuals, we identified and validated supernormal S-cone acuity in Enhanced S-cone Syndrome. Our discussion delves into potential retinal re-organization mechanisms, possibly involving the recruitment of elements from the rod pathway to achieve superior S-cone acuity.

Subsequently, upon noting fixation displacement mediated by the S-cone pathway during acuity experiments, we embarked on a comprehensive exploration of oculomotor function guided by the S-cone pathway. A consistent superior displacement of the S-cone-mediated preferred retinal locus (PRL) of fixation in six normal subjects was observed.

This displacement was also found in saccade landing positions between chromatic (S-cone-mediated) and luminance (L/M-cone-mediated) systems, indicating that the S-cone pathway could mediate its own stimulus detection and saccade initiation.

Moreover, the investigation into the human S-cone topography heterogeneity entailed functional mapping of the S-cone-free zone in normal eyes using adaptive optics microperimetry. Macular pigment imaging aided in addressing the pre-receptoral blue filtering effect on S-cone sensitivity. We discussed the interplay between S-cone acuity, S-cone preferred retinal locus displacement, and S-cone scotoma size.

These findings collectively demonstrate the utility of adaptive optics imaging and psychophysics in understanding the functional topography of the S-cone pathway, shedding light on its heterogeneity and potential implications for visual function in both normal and pathological conditions.

Table of Contents

List of Figures

List of Tables

Acknowledgements

I would like to acknowledge my mentors, colleagues, and friends at UC Berkeley and UCSF for their support in my journey to becoming a scientist.

First and foremost, I extend my heartfelt gratitude to Dr. Austin Roorda for believing in me and welcoming me into his lab as an optometry student researcher through the T35 summer research program in 2016. This invaluable experience sparked my passion for research in Adaptive Optics (AO) retinal imaging and psychophysics. His ongoing mentorship and collaboration during my nine years of clinical and research training at UC Berkeley have profoundly shaped my career.

I am deeply appreciative of Dr. William Tuten, my PhD co-advisor, for his endless support and inspiration. His guidance, mentorship and encouragement have made me the scientist I am today.

I am fortunate to have worked with Dr. Jacque Duncan at UCSF, who has been an exemplary mentor and role model, significantly advancing my research and career aspirations as a clinician scientist.

I am grateful for having built close friendships with Dr. Susana Chung, Dr. Meredith Whiteside, and Dr. Katie Litts, whose mentorship and support across academia, clinic, and industry have made me a well-rounded scientist and clinician.

I am also thankful for the opportunity to work with an incredible group of colleagues from the Roorda, Tuten, and Duncan labs over the past four years. I would like to express my appreciation to the current and past members of the Roorda lab: Josephine D’Angelo, Leah Johnston, Jason Wong, Dr. Shangbang Luo, Hannah Doyle, James Fong, Pavan Tiruveedhula, Dr. Congli Wang, Dr. David Merino, Dr. Zohreh Hosseinaee, Dr. Khang Huynh, Dr. Fabio Feroldi, Dr. John Erik Vanston, Dr. Norick Bowers, Dr. Gareth Hastings, Dr. Sanam Mozaffari, Dr. Ethan Bensinger, and Swati Bhargava, for their support and friendship.

I am also grateful for being a part of the Tuten lab and working with Dr. Jingyi He, Maxwell Greene, JT Pirog, Lauren Sigda, Angeline Yang, BaoChau Vu, Dr. Alisa Braun, and Dr. Alexandra Boehm.

Additionally, I am extremely fortunate to have worked with members and collaborators of the UCSF Duncan lab: Jessica Wong, Stephanie Duret, Dr. Erika Mae Reyes, Roxanna Rabiee, Dr. Felice Dunn, Dr. Scott Harris and Jeremiah John.

Most importantly, I am thankful to my parents, Dr. Wangbi Yan and Dr. Zheng Wang, and my sister, Chloe Shiyan Wang, for their unconditional love and being my rock through all my life pursuits.

A special thank you to George Qiuzhi Ji. Your loving support and encouragement have been a constant source of strength. You inspire me every day to be a better person, and your belief in my potential is a driving force in my journey onward.

I would also like to recognize my close friends who have supported me through the ups and downs: Dr. Yujia Zhang, Dr. Xiao Li, Dr. Celia Sze Kei Yeung, Dr. Charlie Ngo, Dr. Guanghan Meng, Dr. Vivien Tse, Janerra Allen, Dr. Vivian Look, Kelsey Ding, Dr. Aaron Gong, Dr. Sheila Soltani, Dr. Joan Astorino, Stephanie Reeves, Dr. Angelica Godinez, Chenyu Wang, Jianglong Huang, Dr. Julia Xiong, Dr. Ivy Yi Yang, Dr. Katharina Foote, and Yuning Liu. Your friendship has been invaluable to me.

Last but not least, I would like to extend profound gratitude to the UC Berkeley Herbert Wertheim School of Optometry and Vision Science where I completed my Doctor of Optometry, Residency, and Vision Science PhD. The academic environment, combined with the guidance of dedicated faculty and mentors, has played a pivotal role in shaping my career and research journey. I am deeply thankful for the opportunities, knowledge, and skills I have gained during my time at this institution.

1 Chapter 1 | Introduction

1.1 Introduction

A normal human eye contains around 120 million rod photoreceptors and 6 million cone photoreceptors. In the mature retina, rods and cones exhibit distinct topographical density profiles, the result of complex and finely orchestrated developmental processes that are initiated during gestation and continue postnatally until roughly 4 years of age (Yuodelis & Hendrickson, 1986). Rods – which are sensitive to dim light and responsible for scotopic vision – are absent at the foveola, and outside the fovea their packing density rises steadily with eccentricity, reaching a peak between 10° and 20° before declining again in the peripheral retina (Curcio et al., 1990; Lee et al., 2019). Despite the large number and high spatial density of rods, visual acuity is comparatively poor under scotopic conditions due to spatial convergence in rod-driven circuits (Lee et al., 2019; Lennie & Fairchild, 1994; Wilkinson et al., 2020). The packing density of cone photoreceptors peaks at the foveal center and falls sharply with increasing eccentricity (Curcio et al., 1990; Y. Wang et al., 2019).

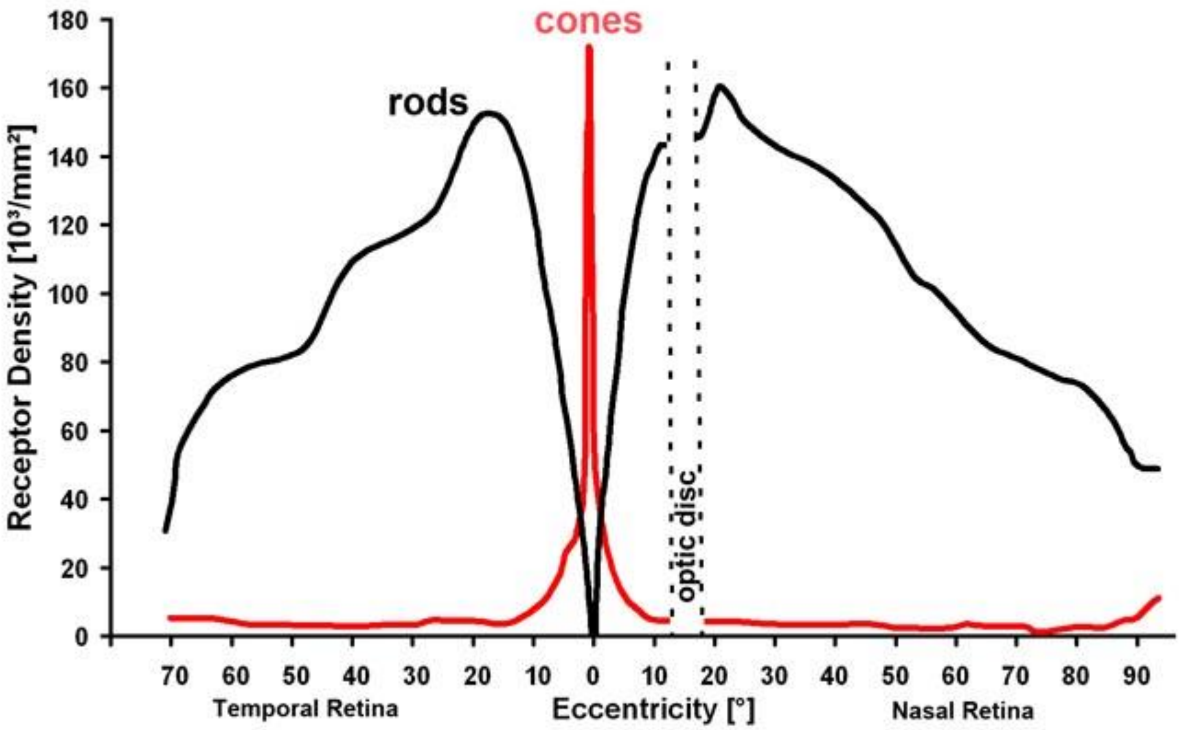

Figure 1.1 Rods and Cones Density as a Function of Retinal Eccentricity

The densities of human rod and cone photoreceptors along the horizontal meridian are illustrated. Rods are absent at the fovea but reach their highest density around 20° eccentricity. Cones exhibit the highest density at the fovea, with their density decreasing rapidly beyond the foveal center. This figure is adapted from (Østerberg, 1937).

1.2 S-cone Structure and Topography

Humans with normal color vision have three cone types, sensitive to long, medium, and short wavelengths of light and referred to as L-, M-, and S-cones, respectively. Like rods, S-cones are also likely excluded from the centralmost fovea and follow a non-monotonic density profile, with a peak spatial density occurring near 1° eccentricity (Curcio et al., 1991). Another histology report indicates a decrease in S-cone density at the foveola without a region completely devoid of S-cones (Ahnelt, 1998). Nevertheless, the fraction

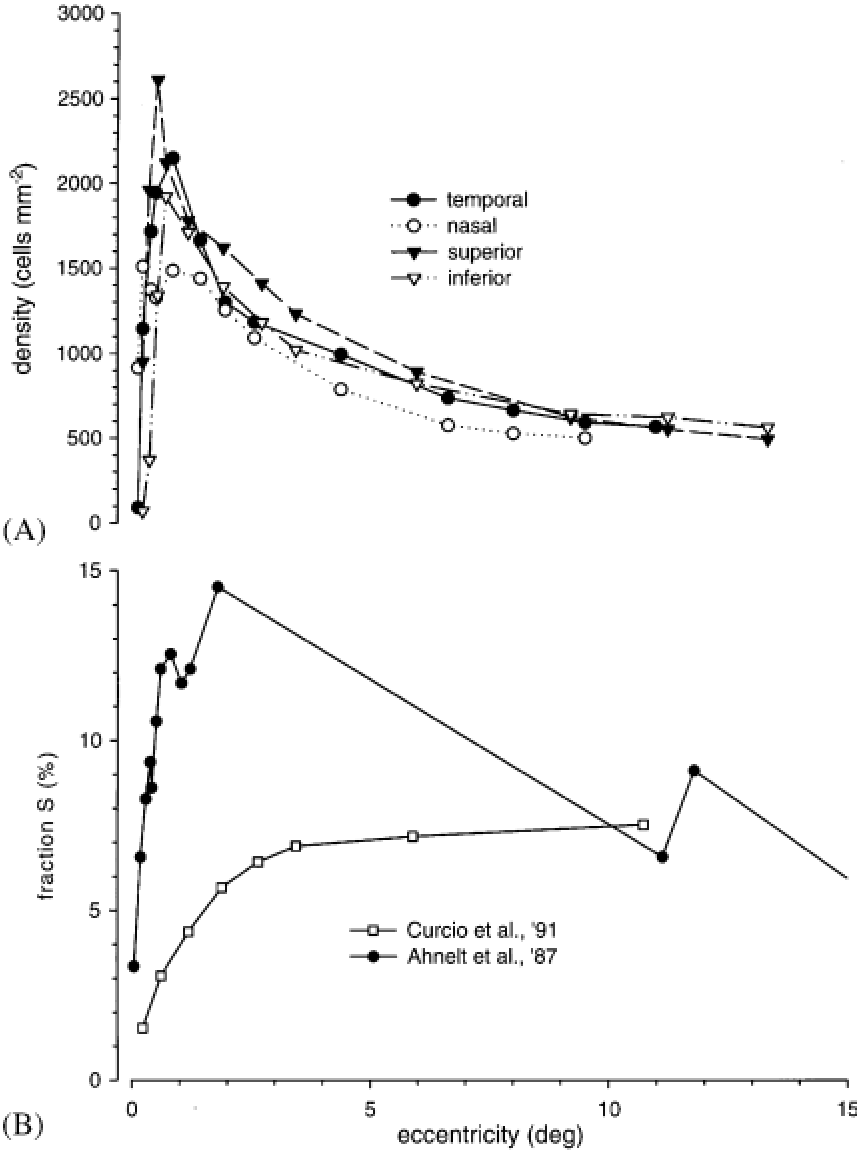

Figure 1.2 S-cone Density in the Human Retina from (Calkins, 2001)

(A) Measurements of the density of S-cones stained using opsin-specific antibodies along the cardinal meridians, modified from (Curcio et al., 1991). (B) The fraction of S-cones based on immunocytochemical identification (Curcio et al., 1991) and morphological identification (Ahnelt et al., 1987) .

of S-cones is lowest at the foveal center and gradually increases with greater retinal eccentricity.

S-cones comprise 5-10% of the overall cone photoreceptor population, with L/M-cones making up the remaining 90-95%. L/M-cones are mostly densely packed at the foveal center. Consistent with their high packing density, L/M-cones in the central retina are wired into specialized neural circuits canonically associated with high-resolution spatial vision (Rossi & Roorda, 2010; Zhang et al., 2020), whereas S-cones primarily feed into chromatic pathways with lower resolving capacity (Anderson et al., 2002; Sekiguchi et al., 1993). Among all types of photoreceptors including rods, S-cones represent a mere ~0.2% of all photoreceptors in normal eyes (Roorda & Williams, 1999).

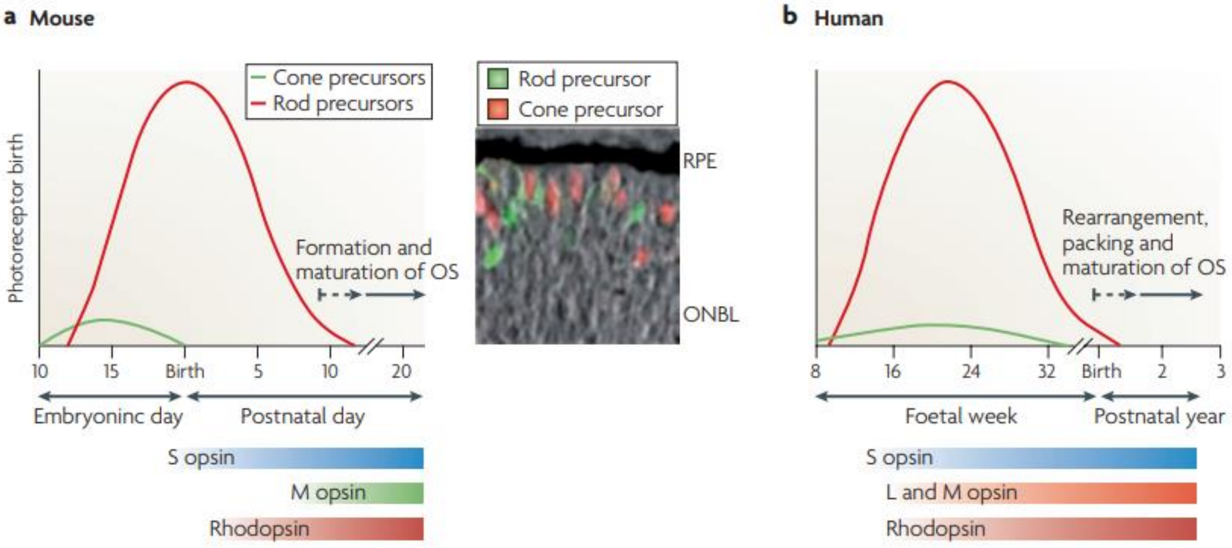

Figure 1.3 Mouse and Human Photoreceptor Development

The photoreceptor development paths of mice and human are shown. In humans, cones and rods are generated around fetal week (Fwk) 8 and Fwk 10, respectively. The generation of cones is completed prenatally, whereas the generation of rods continues into the early postnatal period. Expression of S-opsin is observed around Fwk 12, while the expression of L-opsin, M-opsin, and rhodopsin occurs around Fwk 15. Functional maturation of photoreceptors continues postnatally. Figure from (Swaroop et al., 2010).

The outer segment of S-cones contains the photopigment cyanolabe, or S-opsin, which is sensitive to blue light, with a peak sensitivity around 420-440 nm. S-cones have taller inner segments than rods and L/M-cones, with a more posteriorly located inner/outer segment junction (Calkins, 2001; Curcio et al., 1991). This morphological difference in S-cones is used for cell identification in histology (Ahnelt et al., 1987; Curcio et al., 1991) and in modern optical imaging tools such as adaptive optics optical coherence tomography (AO-OCT), which identify S-cones by their shorter outer segment length, longer inner segment length, bigger IS/OS junction diameter and more posteriorly located IS/OS junction layer (Ji et al., 2023; Jonnal et al., 2007; Miller & Kurokawa, 2020; Pandiyan et al., 2021).

Reports on S-cone foveal topography have been limited to histological studies. Adaptive optics-based densitometry and OCT-based optoretinography have limited resolution at the foveal center, making foveal cone classification challenging (Sabesan et al., 2015; Schleufer et al., 2022).

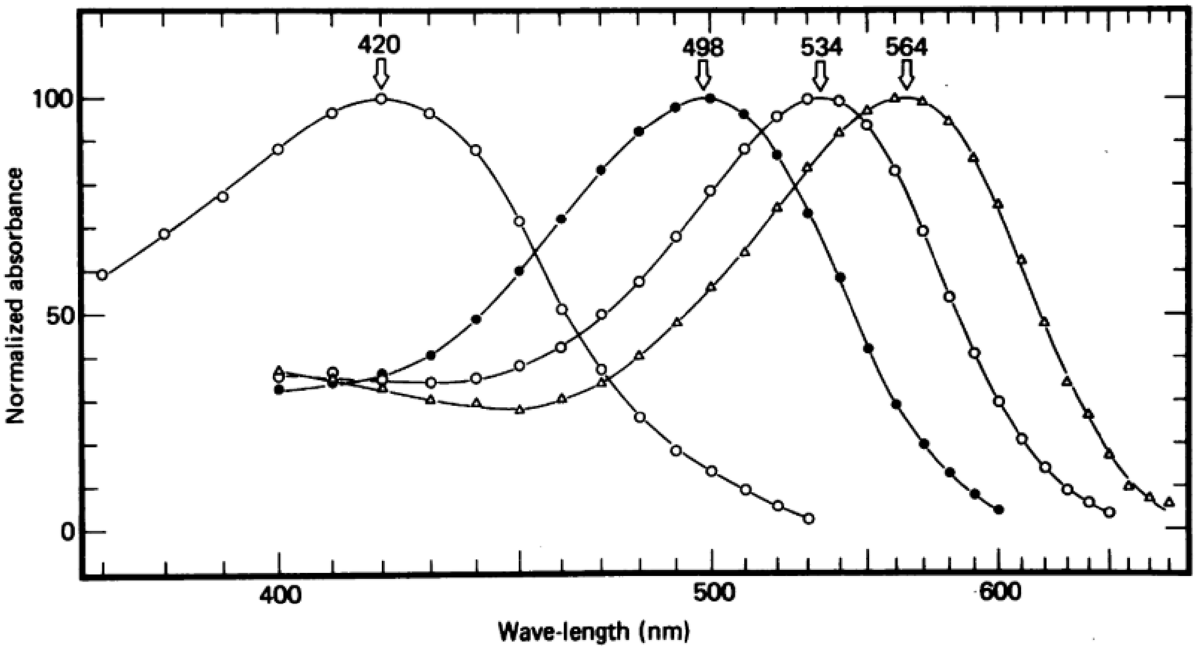

Figure 1.4 Photoceptor Absorbance Spectra

The absorbance spectra of photoreceptors include rods, which peak at 498 nm (indicated by filled circles), and cone outer segments. The cones are categorized into three types based on their peak absorbance: S-cones peak at 420 nm, M-cones peak at 534 nm, and L-cones peak at 564 nm. This figure was adapted from (Bowmaker & Dartnall, 1980).

1.3 S-cone Photoreceptor Development

S-cones are the default primordial cone cells, and they develop before L/M-cones. S opsin is expressed about a month before L/M opsin, and the same expression pattern is observed for both mRNA and protein (Xiao & Hendrickson, 2000). S opsin first appears near the fovea at fetal week 10.9 and covers more than 90% of the retina by fetal week 18–19. However, L/M opsin protein does not appear until fetal week 14–15 in the fovea and reaches the retinal edge by fetal week 34–37 (Xiao & Hendrickson, 2000). Rhodopsin is produced after S-opsin but around the same time as L/M opsin expression, which is present in fetal week 15. The S-cone density in human fetal retina was reported three times as adult level at fetal week 14-18, and the ratio of S-cones to L/M-cones changes significantly as other photoreceptor types are developed, suggesting an identity switch from the S-opsin to L- or M-opsin expression by the precursor cells (Swaroop et al., 2010; Xiao & Hendrickson, 2000). Furthermore, S-opsins are expressed first before a portion of precursor cells changes to M-cones in rodent retinas (Szél et al., 1994).

1.4 S-cone Function

The neural sampling limit for human vision is governed by the retinal ganglion cells (RGCs) that convey signals from the retina to the brain (Dacey, 1993). At the fovea, there is minimal convergence from cones to midget retinal ganglion cells, as one cone photoreceptor connects to at least one ON-ganglion cell and one OFF-ganglion cell. This preserves visual information such that central foveal vision is limited by optical aberrations and the sampling of the cone photoreceptors (Dacey, 1993). Just outside of the fovea, spatial vision becomes poorer than predicted by the sampling limit of the photoreceptors, and better matches the sampling limit of midget ganglion cells as they collect signals from multiple cones (Anderson et al., 2002, 1992; Rossi & Roorda, 2010; Thibos et al., 1987).

S-cones are generally considered not to contribute significantly to the pathways that support fine spatial vision for several reasons. First, S-cones are not present in the foveal center (Curcio et al., 1991; Williams et al., 1981b). Second, they are quite sparse elsewhere in the retina comprising only 10% of the cones at most. Third, S-cone excitatory signals are transmitted by a different class of retinal ganglion cells, the small bistratified retinal ganglion cells (Dacey & Lee, 1994). In a normal eye, S-cone mediated spatial resolution is very poor, and closely correlates with the sampling limit of the small bistratified cells (Anderson et al., 2002; Dacey, 1993). The density range of the human small bistratified retinal ganglion cells (sbRGCs) is estimated to range from 400 cells/mm^2 centrally to 20 cells/mm^2 peripherally (Dacey, 1993). Given maximal density of around 400 cells/mm^2 centrally, the predicted maximal S-cone acuity guided by sbRGCs is around 3 cycles/deg. The S-cone mediated acuity reported in several psychophysical studies are generally below 8 cycles/degree in the central and peripheral retina (Anderson et al., 2002; Coates & Chung, 2016; Metha & Lennie, 2001).

1.5 Adaptive Optics Retinal Imaging and Psychophysics

Studying the relationship between photoreceptor structure and function requires a high-resolution tool that can visualize cell topography and deliver stimuli accurately to specific regions of the retina. Imaging individual cone photoreceptor structures in living eyes, especially near the fovea, necessitates the correction of optical aberrations within the imaging system. Even when spectacles and contacts lenses can correct for defocus and astigmatism, higher-order aberrations still prevent diffraction-limited imaging of the retinal cells.

Adaptive optics (AO) addresses the optical imperfections of the human eye. It measures the optical aberrations of the eye using a wavefront sensor and converts the wavefront information into voltage signals for the actuators of a deformable mirror. The mirror then actively compensates for the aberrated wavefront by pushing and pulling as needed (Liang et al., 1997).

The adaptive optics scanning laser ophthalmoscope (AOSLO) system is a point-scanning laser system that uses AO to achieve near diffraction-limited imaging of individual cone photoreceptors, even at their densest packing in the fovea (Roorda et al., 2002; Y. Wang et al., 2019). AOSLO systems are used in multiple laboratories worldwide and are extensively employed for both basic and clinical research (Litts et al., 2017; Roorda & Duncan, 2015; Sincich et al., 2016).

In addition to structural imaging, AO-based instruments enable several key functional measurements. These include the assessment of the preferred retinal locus (PRL), AO-corrected visual acuity, and AO-microperimetry.

Preferred Retinal Locus (PRL) Assessment

Evaluation of the PRL can be achieved by modulating the visible light channel, often using 543 nm or 680 nm light, or a decrement stimulus in the 840 nm channel. The duty cycle and size of the stimulus can be pre-determined and fixed within the imaging raster. While the subject fixates on the PRL stimulus, a retinal video is recorded simultaneously. The exact retinal locations where the stimulus lands during fixation, as captured in the video, are used to determine the mean PRL and fixation stability.

AO-Corrected Visual Acuity

Foveal acuity is guided by the sampling limit of the cone photoreceptors and optical factors (Tuten & Harmening, 2021). Normal human vision can achieve a mean acuity of 20/9.8 when optical aberrations are bypassed, with the best recorded acuity being 20/7 in one normal subject (Rossi et al., 2007). AO-corrected visual acuity measures spatial resolution primarily limited by photoreceptor spacing, minimizing the optical factors. These measurements are made on the AOSLO system, where an AO-corrected decrement letter is delivered on a dark red background by modulating the 840 nm laser raster at appropriate times within the scan (Foote et al., 2018). The psychophysical method for determining the acuity threshold can be customized using QUEST adaptive staircase and a 4-alternative forced choice, tumbling-E paradigm (Watson & Pelli, 1983).

AO-Microperimetry (AOMP)

Retinal sensitivity is commonly evaluated with visual field and perimetry methods in clinical settings. Individual variability and eye motion can cause measurement errors. AO-based microperimetry (AOMP) with real-time eye tracking can examine the retinal sensitivity of targeted areas using small, retinally stabilized increment stimuli (Tuten et al., 2012). AOMP measurements are made on the same AOSLO platform, with simultaneous imaging and tracking with infrared light and visible-light stimulus presented at targeted locations via the same raster scan. The vergence of the visible-light channel is set to offset the eye's native longitudinal chromatic aberration, ensuring the AOMP stimulus is focused on the same plane as the infrared imaging light (Harmening et al., 2012). Test locations are manually selected by experimenters, and the intensity of the test stimuli can be guided by a customized adaptive staircase procedure.

S-cone AO-Psychophysics

A monochromatic short-wavelength laser can be incorporated into the AOSLO stimulation system to achieve S-cone-mediated psychophysical measurements. Chromatic adaptation is utilized to desensitize L/M-cones while S-cones are stimulated with short-wavelength light, or blue light. Utilizing AOSLO ensures accurate stimulation, correction of longitudinal and transverse chromatic aberrations, and allows customization of the spatial, temporal, and chromatic aspects of the experimental stimuli.

The S-cone AOMP uses a blue-on-yellow paradigm along with real-time eye tracking to allow psychophysical measurements of the S-cone pathway. More details of this method will be elaborated in Chapter 4.

AOSLO has limited application in measuring S-cone acuity primarily due to the size of the S-cone threshold letter, which averages 20/200. The typical AOSLO raster size is about 1°, constrained by the human isoplanatic patch, which limits consistent wavefront sensing (Bedggood et al., 2008). Since a 20/200 Snellen letter nearly spans a 1° visual field, the AOSLO system alone is insufficient for this task. Therefore, an additional projector display is required to deliver the appropriately sized stimuli for accurate S-cone acuity measurements.

2 Chapter 2 | Structure and Function in Patients with Enhanced S-cone Syndrome

2.1 Abstract

We provided the first measures of S-cone spatial resolution as a function of retinal eccentricity in patients with Enhanced S-cone Syndrome (ESCS) and discussed the possible mechanisms supporting their supernormal S-cone acuity.

We used an adaptive optics scanning laser ophthalmoscope (AOSLO) to characterize photoreceptor packing. A custom non-AO display channel was used to measure L/M- and S-cone mediated visual acuity during AOSLO imaging. Acuity measurements were obtained using a 4-alternative forced choice, tumbling-E paradigm, along the temporal meridian between the fovea and 4° eccentricity in 5 of 6 ESCS patients and in 7 control subjects. L/M-cone acuity was tested by presenting long-pass-filtered optotypes on a black background, excluding wavelengths to which S-cones are sensitive. S-cone isolation was achieved using a two-color, blue-on-yellow chromatic adaptation method that was validated on 3 control subjects.

Inter-cone spacing measurements revealed a near-uniform cone density profile (ranging from 0.9-1.5 arcmin spacing) throughout the macula in ESCS. For comparison, normal cone density decreases by a factor of 14 from the fovea to 6°. Cone spacing of ESCS subjects was higher than normal in the fovea and subnormal beyond 2°. Compared to control subjects (N=7), S-cone-mediated acuities in ESCS patients were normal near the fovea and became increasingly supernormal with retinal eccentricity. Beyond 2°, S-cone acuities were superior to L/M-cone-mediated acuity in the ESCS cohort, a reversal of the trend observed in normal retinas.

Higher-than-normal parafoveal cone densities (presumably dominated by S-cones) confer better-than-normal S-cone mediated acuity in ESCS subjects.

2.2 Introduction

As described in Chapter 1, humans with normal color vision have three types of cones (L-, M-, and S-cones). S-cones, excluded from the central fovea, peak near 1° eccentricity and increase in proportion up to 10° eccentricity, comprising 5-10% of the cone population (Curcio et al., 1991; Schleufer et al., 2022). L/M-cones make up 90-95% and are wired for high-resolution spatial vision (Marcos & Navarro, 1997; Rossi & Roorda, 2010; Thibos et al., 1987; Williams & Coletta, 1987; Zhang et al., 2020). S-cones primarily contribute to chromatic pathways with lower resolving capacity (Anderson et al., 2002; Dacey, 1993; Sekiguchi et al., 1993), representing ~0.2% of all photoreceptors.

Enhanced S-cone Syndrome (ESCS) is a rare inherited retinal degeneration in which photoreceptor differentiation is disrupted during development and rod precursors are misdirected to form photoreceptors that express opsin typically associated with S-cones. ESCS was first described in 1989 with pathognomonic electroretinogram (ERG) findings and its name came from the enhanced short-wavelength-sensitive cone function measured with ERG and psychophysics (Jacobson et al., 1990; Marmor, 1989; Marmor et al., 1990). Together, these results point towards a supernormal complement of S-cones in patients with ESCS (Audo et al., 2008; Garafalo et al., 2018; Roman et al., 2019).

ESCS is mostly associated with biallelic disease-causing variants in the nuclear receptor subfamily 2, group E, member 3 (NR2E3) gene, which encodes a transcription factor that promotes rod differentiation and suppresses the cone-expressing genes in the photoreceptor progenitor cells, as shown in the rd7 mutant mouse, a model for human ESCS (Corbo & Cepko, 2005). Other NR2E3 gene mutations that solely affect rod photoreceptor transactivation result in autosomal dominant retinitis pigmentosa (adRP) instead (Coppieters et al., 2007). ESCS can also be associated with mutations in the NRL (neural retina leucine zipper) gene, a transcription factor upstream of NR2E3 (Littink et al., 2018; Mears et al., 2001). Biallelic pathogenic variants in the NRL or the NR2E3 gene misdirect rod precursors to produce S-cones. More details of the ESCS structure and function can be found in this review article (Wang et al., 2023a).

Characterizing outer retinal cellular topography in ESCS is an important first step toward understanding the structural and functional consequences of disruptions to the regulatory networks that determine photoreceptor fate. In the simplest scenario, where precursor cells fated to become rods instead develop into S-cones, and no other developmental processes are affected, the S-cone density profile should mirror that of rods in the normal retina, with supernormal cone densities outside the fovea. Postmortem findings from a 77-year-old ESCS donor eye confirmed the absence of rod photoreceptors and showed a twofold increase in overall cone density at a mid-peripheral retinal location (~15° nasal) analyzed via immunohistochemistry, with S-cones comprising 92% of the remaining photoreceptors (Milam et al., 2002). More recently, high-resolution retinal imaging studies using adaptive optics have shown in a small number of subjects that the supernormal cone densities observed histologically are also present in vivo at eccentricities as low as 3° (Ammar et al., 2021; Roorda et al., 2010), although overall cone counts at some parafoveal eccentricities were lower than the combined number of rods and cones that would normally be present in a healthy eye (Roorda et al., 2010). Furthermore, cone densities at the foveola, where S-cones and rods are excluded, were reduced compared to normal (Roorda et al., 2010). Currently, it remains unclear if the genetic mutation(s) underlying ESCS also interfere with the development of the L/M-cone subsystem, or if the reduced cone densities observed previously are the consequence of an ongoing diffuse degenerative process that causes cell loss in all extant receptor types.

The supernormal cone densities observed in these previous studies raise the intriguing possibility that patients with ESCS may, under certain conditions, be equipped with supernormal visual capacities. Realizing this possibility requires that the post-receptoral visual system can take advantage of the information encoded by the abnormally dense receptor array. While prior studies have shown that the supernumerary complement of S-cones in ESCS confers improved performance on tasks such as contrast detection

(Garafalo et al., 2018; Greenstein et al., 1996), and flicker perception (Ripamonti et al., 2014), the extent to which these benefits extend to the spatial domain is less clear. Greenstein and colleagues measured S-cone-isolated grating acuity at 6° eccentricity in three ESCS patients and reported a twofold improvement compared to normal (Greenstein et al., 1996), although the underlying receptor distribution at their test location was not known. In this study, we use a custom high-resolution retinal imaging and visual function testing platform to characterize cone topography across the central retina in ESCS subjects while simultaneously measuring L/M- and S-cone-mediated visual acuity. Understanding the structure-function relationship in the ESCS retina could shed light on the potential benefits of NR2E3 gene-related therapeutic treatments (Haider et al., 2006; Nakamura et al., 2016; Upadhyay et al., 2020), as well as the possibility of retinal remodeling during development when photoreceptors are abnormally distributed.

Subject	Exam Year	Age	Gender	Genetics	Visual Acuity	Color Vision	Note
10055	2009	59	Female	*NR2E3:* c.373C>T (p.Arg125Ter) *NR2E3:* c.626dup (p.Tyr209Ter)	20/200 20/200	Not measured	
10054	2009	35	Male	*NR2E3:* c.229C>T (p.Arg77Trp) *NR2E3:* c.373C>T (p.Arg125Ter)	20/32 20/32	Normal	Nephew of 10055
	2022	48			$20/32^{-1}$ $20/40^{-1}$	Normal	
40188	2019	19	Female	*NR2E3*: c.932G>A (p.Arg311Gln) homozygous	20/20 20/20	Normal	
	2021	21			$20/16^{-2}$ $20/20^{+1}$		
40231	2021	22	Male	*NR2E3*: c.932G>A (p.Arg311Gln) homozygous	$20/30^{+2}$ $20/40^{+2}$	Normal	
40234	2022	20	Female	*NR2E3*: c.932G>A (p.Arg311Gln) homozygous	$20/60^{-}$ 20/40	Normal	Sister of 40231
40133	2015	16	Male	*NR2E3:* c.702G>A, p.(Trp234*) *NR2E3*: c.223G>T (p.Val75Leu) VUS	20/25 20/25	Normal	
	2021	22			20/25 20/25		

Table 2.1 Demographics and Clinical Data of 6 ESCS Subjects

The age, genetics, best-corrected visual acuity, and color vision results are from the clinical eye examination of the corresponding years. The visual acuities of the right eye (upper) and left eye (lower) were reported in two separate rows.

2.3 Materials and Methods

2.3.1 Subjects

Retinal structure of 6 and function of 5 ESCS subjects were measured at University of California, San Francisco (UCSF). ESCS subjects' results were compared with age-matched normal subjects (N = 7) recruited and imaged at the University of California, Berkeley (UCB). Informed consent was obtained from all subjects after explaining the purpose and possible consequences. The research protocol was approved by the institutional review boards of the University of California, San Francisco and the University of California, Berkeley.

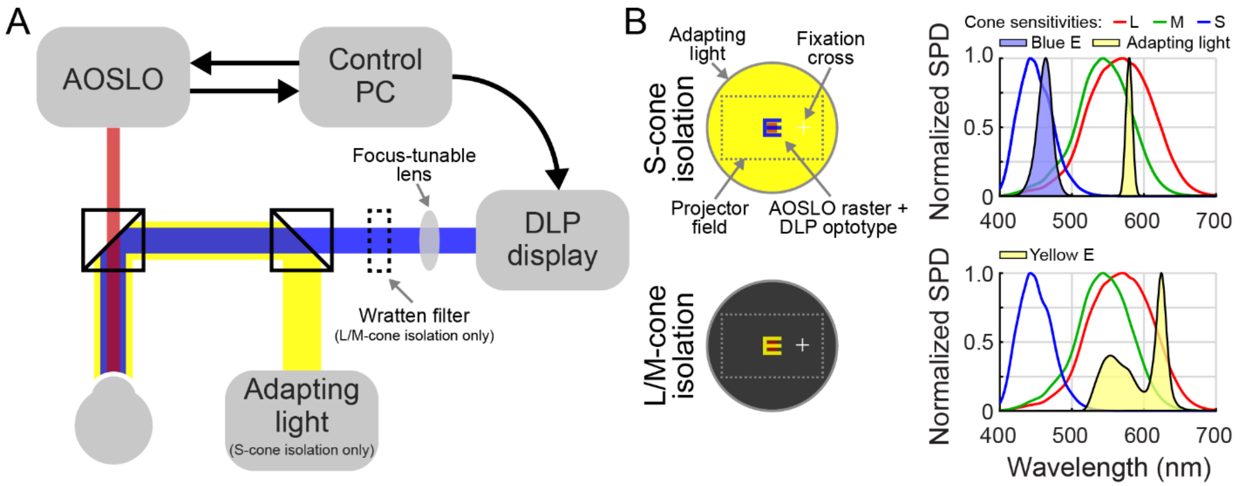

Figure 2.1 Imaging and Psychophysics System Schematic

(A) The psychophysical Optotype E is delivered from the high-resolution Digital Light Processing (DLP) projector display through a different light path coaligned with the AOSLO beam. The focus of the letter E is adjusted with a focus-tunable lens subjectively. In the S-cone isolation condition, a background adapting light is created from an external light source coaligned with the projector path and AOSLO beam. The yellow adapting light is turned bright enough to desensitize the L/M-cones during S-cone acuity measurement. In the L/M-cone isolating condition, a yellow letter E is created by filtering a white light through a long-pass Wratten 16 filter whose spectrum is outside of the sensitive region of the S-cones. (B) Cone isolation is achieved utilizing differences in spectral sensitivities (Stockman & Sharpe, 2000). In the S-cone isolation condition, the subject views a blue letter E against a bright yellow background. In the L/M-cone isolation condition, the subject views a yellow letter E against a black background. The red AOSLO infrared raster is present and centered with the letter in both conditions.

All ESCS subjects had clinical eye examinations prior to the research visits and consented to release their medical records. Full-field ERG testing in all subjects showed characteristic findings (Marmor et al., 1990), and genetic testing results revealed biallelic disease-causing variants in the NR2E3 gene and confirmed the diagnosis of ESCS in all subjects. Best-corrected visual acuity was measured during clinical eye examination based on the Early Treatment of Diabetic Retinopathy Study (ETDRS) protocol (Ferris et al., 1982). Color vision was assessed in all subjects with Farnsworth D-15 Dichotomous Color Blindness Test (Cole, 2007). Cross-sectional scans of the retinas were obtained with spectral-domain OCT (SD-OCT; Spectralis HRA+OCT system [Heidelberg Engineering, Vista, CA, USA]). For each subject, the eye with better-appearing retinal structure integrity on OCT was selected to perform adaptive optics scanning laser ophthalmoscope (AOSLO) retinal imaging and psychophysical measurements. In some cases, AOSLO images of the fellow eye were also obtained, but time constraints prevented additional psychophysical testing. Subject 10055 was not recalled for updated

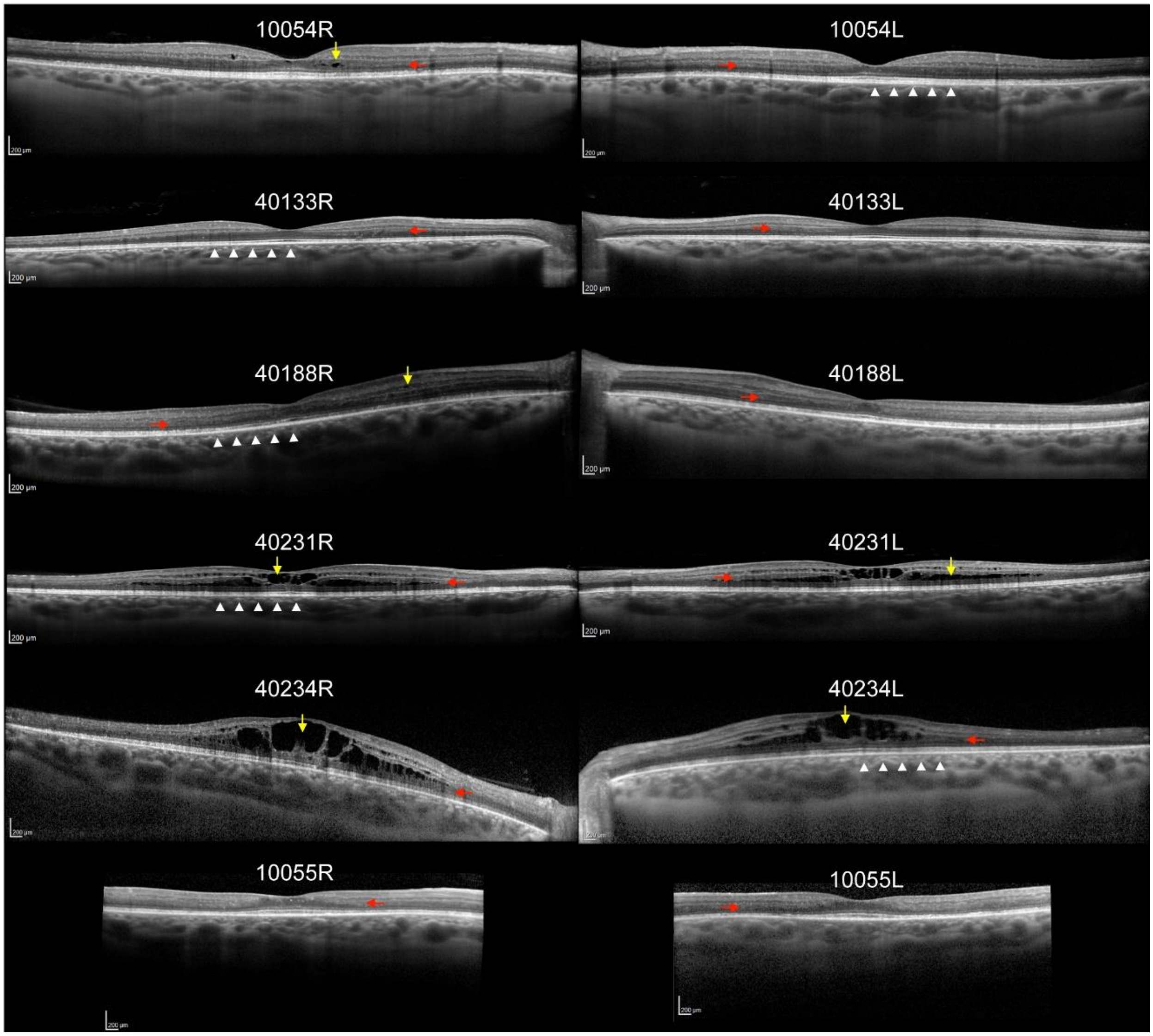

Figure 2.2 Optical Coherence Tomography (OCT) images of 6 ESCS subjects

Both eyes of all subjects are shown. Each OCT scan is 30 degrees except for 10055 (20 degrees). All subjects showed abnormal retinal lamination in the outer nuclear layer where an additional hyperreflective band (indicated by red arrows) is observed, possibly representing abnormally visible Henle's fiber layer (Ammar et al., 2021). 10054R, 40188R, 40231R&L, and 40234R&L showed intraretinal cysts (indicated by yellow arrows). 5 eyes of 6 subjects were measured with cone-type-isolated acuity, and the presumed test locations are indicated by the white arrowheads from fovea to 4° temporal retina.

AOSLO imaging and additional psychophysical measurements due to extensive retinal degeneration and poor visual acuity found in 2009.

2.3.2 High Resolution Retinal Imaging and Analysis

All subjects were dilated with 1% tropicamide and 2.5% phenylephrine in both eyes before their research visits. AOSLO images of were acquired using the systems at UCSF and UCB (Duncan et al., 2007; Y. Wang et al., 2019). Both systems have similar optical design and identical software controls. Retinal videos at 512 × 512 pixels of ESCS subjects were acquired at 30 frames per second over a 1.2° × 1.2° field of view on the retina (0.9° x 0.9° field of view for normal subjects using the UCB system). We imaged ESCS subjects in the central 5° area and extended the horizontal meridians out to 8° eccentricities with the UCSF system; whereas normal subjects at UCB were imaged out to 4° along the temporal meridian where visual acuity was measured. High-resolution retinal images were generated offline with custom software after correcting for distortion caused by fixational eye movements (Stevenson et al., 2010). All images at the macula and along the horizontal meridian were stitched together (Photoshop; Adobe Systems, Inc, Mountain View, CA, USA) into a single montage using custom software (Chen et al., 2016).

In each ESCS retinal montage in areas where contiguous arrays of cones were well-resolved, 0.2° x 0.2° regions of interest (ROIs) were manually selected. Cone spacing was analyzed within these ROIs using custom software (Mosaic Analytics, Translational Imaging Innovations, Hickory, NC, USA) designed to analyze cell mosaics from AOSLO images, as previously described (Cooper et al., 2016). The Z-score value of each ROI's cone spacing was reported as standard deviations from a normal database at the measured eccentricity (Duncan et al., 2023).

2.3.3 Measuring S- and L/M-Cone Isolated Visual Acuity

S-cone isolation was achieved using a two-color, "blue-on-yellow” chromatic adaptation method, which leveraged the distinct spectral sensitivities of the S- and L/M-cone types to suppress the sensitivity of L/M-cones while preserving S-cone contrast (Anderson et al., 2002; Coates & Chung, 2016; Figure 2.1A). A modified high-resolution (136 pixels/degree) Digital Light Processing (DLP) projector (TI DLP LightCrafter 4500, Texas Instruments Inc., Dallas, TX, USA) was used to present the blue S-cone-isolating letter E in a Maxwellian view configuration. The spectral power distribution of the DLP's blue primary is shown in Figure 2.1B. The focus of the DLP display was controlled by an electrically tunable liquid lens (EL-3-10, Optotune Switzerland AG, Dietikon, Switzerland) placed in a plane conjugate to the subject's pupil; the aperture of the liquid lens formed a 2.5-mm artificial pupil through which the subject viewed the acuity stimulus. The focus of the DLP display was adjusted manually by the experimenter while the subject judged the sharpness of an ETDRS acuity chart rendered with the blue projector primary. A cylindrical trial lens was placed adjacent to the liquid lens to correct for any residual astigmatism based on the subject's refractive error.

To create a long-wavelength adapting background, broadband light from a fiber optic illuminator source was passed through a narrowband filter (λ_{center} = 580 nm, FB580-10, Thorlabs Inc., Newton, NJ, USA; Figure 2.1B) and delivered to the retina in Maxwellian view; the adapting field subtended approximately 18° and was coaligned to the projector display and AOSLO imaging raster. The luminance of the stimulus and adapting channels was measured using a spectroradiometer (PR-650 Spectra Scan, Photo Research Inc., Chatsworth, CA, USA). On average, the luminance of the projector with blue stimulus was 21.4 cd/m^2, and the yellow background was set to be ≥ 6400 cd/m^2 to produce the ≥300:1 luminance ratio previously demonstrated to achieve S-cone isolation (Coates & Chung, 2016). Measurements obtained from three out of seven control subjects at UCB confirmed that blue-on-yellow acuity performance plateaued at a similar luminance ratio in our apparatus, indicative of S-cone isolation (Figure 2.3).

Prior to data collection, all study participants completed a practice run of 15 trials following the procedures described below. These trials were intended to familiarize participants with the experimental procedure and were discarded from subsequent analyses. At the beginning of each block of trials, the subject first aligned a reticle target presented in the DLP display to the AOSLO imaging raster. This step ensured that DLP stimuli could be presented spatially coincident to the imaging raster, thereby permitting the recovery of the retinal location stimulated on each trial by analyzing retinal videos recording during each trial (see below). Next, the subject adapted for 60 seconds to the yellow background to induce adaptation in L/M-cones. Once the adaptation period concluded, visual acuity was measured using a 4-alternative forced choice (4AFC) tumbling-E paradigm. Each trial consisted of a one-second interval during which a blue letter E was presented for 200 milliseconds (N = 4) or 500 milliseconds (N = 1; see below) against the bright yellow background. We note that subject 40234, whose clinical acuities were reduced due to macular edema, required a longer stimulus duration (500 milliseconds) to reliably detect the acuity stimulus. Targeted retinal locations were selected for acuity testing along the temporal meridian between the fovea and 4° eccentricity in 1° increments. At each eccentricity, acuity was estimated using two 25-trial QUEST staircases collected in succession (Watson & Pelli, 1983). Staircase data were then fitted with a psychometric function (Prins & Kingdom, 2018) to determine the letter size at which the subject was able to correctly identify its orientation 62.5% of the time. The subject initiated each trial and submitted their responses via keypress. All experimental procedures were written in Matlab (Mathworks, Natick, MA) using routines available in the Psychtoolbox (Brainard, 1997).

Because ESCS is a degenerative condition that could produce an overall reduction in visual acuity, L/M-cone-isolated acuities were also measured at each test location to serve as a control against which S-cone acuities could be compared. L/M-cone acuities were obtained following the procedures described above with two exceptions. First, no adapting light was used to suppress the sensitivity of a particular cone class. Second, a yellow optotype was created by filtering a white letter E from the projector system with a long-pass filter (Wratten 16, Eastman Kodak Company, Rochester, NY, USA) to create a stimulus that excluded the part of the spectrum to which S-cones are sensitive. The focus of the DLP display arm was adjusted to optimize the sharpness of a white ETDRS chart viewed through this filter. The mean luminance of the yellow E stimulus was 13.94 cd/m^2, and its spectral power distribution is shown in the lower right panel of Figure 2.1B.

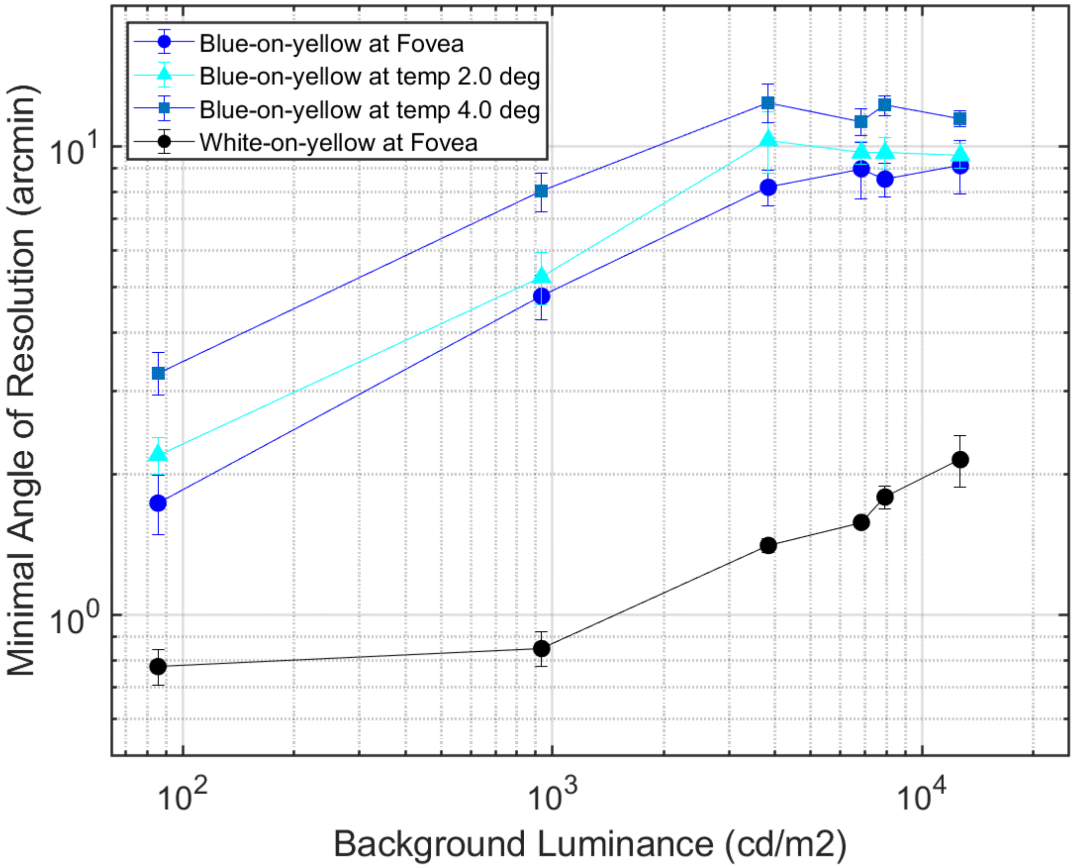

Figure 2.3 Normal S-cone Acuity as a Function of Background Luminance

The blue-on-yellow acuity of 3 out of 7 normal subjects was measured with increasing yellow background luminance until a plateau was reached. Measured retinal locations include fovea, 2° and 4° eccentricities. The black curve shows the control experiment using white letter instead of blue. Error bars are standard errors of the mean.

The targets used to control fixation depended on test eccentricity but were otherwise kept consistent between measurement conditions and subject groups. When measuring acuities away from the fovea, a white square (20 x 20 arcmin) delivered via the projector display was used as a fixation marker. A relatively large marker was chosen to ensure visibility when the bright yellow adapting field was present. For foveal measurements, a large (~3° x 3°) white square outline was presented concentric to the AOSLO imaging raster; the subject was instructed to fixate at the center of this box during the foveal task.

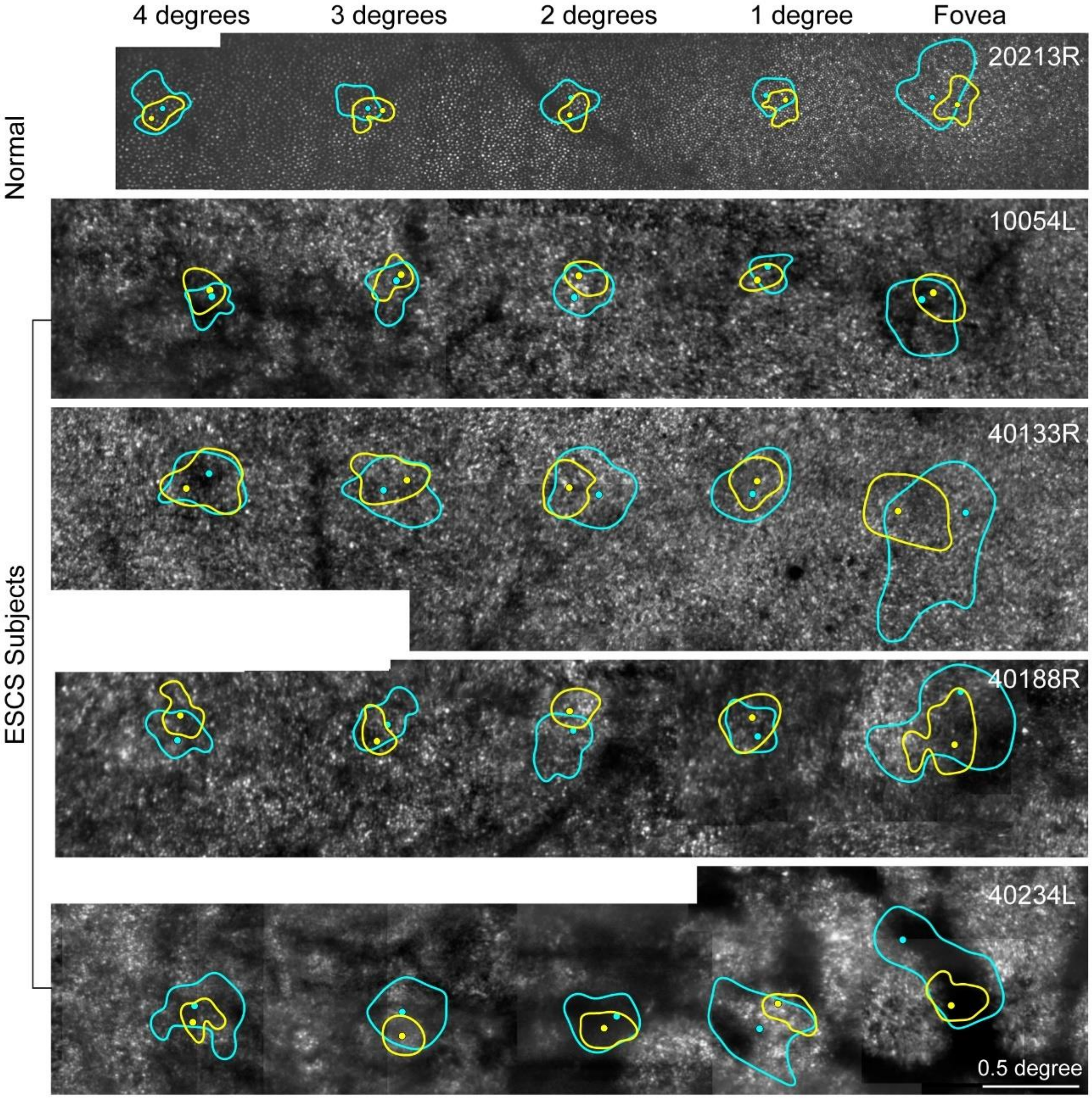

Figure 2.4 AOSLO Images with Fixation Contours during Psychophysics

Each image shows a patch of retina from the fovea to 4° temporal retina. The images of 10054L and 40234L are horizontally mirrored to position the fovea on the right side. The white bar indicates a 0.5° scale. Yellow and cyan contours show 68% fixation distribution from the L/M-cone and the S-cone acuity task, respectively. Within each contour, one large dot indicates the peak density location of the fixation distribution.

For all test conditions, a one-second AOSLO retinal video was recorded concurrently with each psychophysical trial. To synchronize the image acquisition with stimulus presentation on the DLP, a digital marker was added to the AOSLO video frames corresponding to the onset and offset of the acuity stimulus delivered via the projector. AOSLO video frames on which the DLP stimulus was present were extracted and combined into a master video file for each test condition and eccentricity. A reference frame was manually selected from this master video, and all other frames were registered to it with the cross-correlation function in MATLAB; the displacements required to register frames in the master video provide an estimate of eye position during stimulus delivery. An isoline contour analysis algorithm was used to determine the retinal region that encircled 68% of stimulus deliveries (Bowers et al., 2021; Castet & Crossland, 2012). The isoline contour image was then aligned manually to the AOSLO image montage generated as described in the preceding section.

2.4 Results

2.4.1 Structural Analysis

6 ESCS patients had retinal eye examinations and 5 of them underwent high-resolution retinal imaging along with visual psychophysics in 2021 and 2022. The detailed subject profile is shown in Table 2.1. Optical Coherence Tomography (OCT) scans showed abnormal lamination in the outer nuclear layer (ONL) in all the ESCS patients, and cystoid spaces in both eyes of 40231 and 40234, and in the right eye of 40188 (Figure 2.2), similar to findings reported previously (de Carvalho et al., 2021; Jacobson et al., 2004; Yzer et al., 2013). In eyes without macular edema, the foveal pit appeared normal even though the photoreceptor packing in and around the fovea was atypical.

Cone spacing was measured from manually selected regions in the AOSLO images that had contiguous mosaics of unambiguous cones. However, the mosaics in the ESCS patients were not uniform, containing regions with no discernable cones (Figure 2.4). This could reflect cone degeneration (supported by nonuniformity of the photoreceptor lamination in the OCT images), reduced cone reflectivity, or shadows and scattering from edema and the boundaries of the cystoid spaces in the inner retina. Given this uncertainty, one should not use local spacing estimates to infer total cone counts. Rather the cone spacing represents the local maximum density at each eccentricity (Figure 2.5A).

Figure 2.5A shows the cone spacing as a function of eccentricity for 40 normal eyes (Duncan et al., 2023; Y. Wang et al., 2019) and the 7 ESCS eyes. In normal subjects, cone spacing increases with eccentricity, as cone density declines. Cone spacing in 5 ESCS subjects is higher in the fovea than normal but remains uniform with increased eccentricity, with lower-than-normal cone spacing (higher cone density) outside of the fovea. Subject 10055 has increased cone spacing (lower cone density) within 2° of the macular region due to more advanced retinal degeneration, but cone spacing falls within the normal range beginning 3° from the fovea. In the remaining subjects, the majority of cone spacing measurements fall between 1.0 and 1.5 arcmin. Using a previously described approach (Rossi & Roorda, 2010), their cone spacing corresponds to a Nyquist sampling limit of 0.87 and 1.30 arcmin, respectively, for a hexagonally packed cone mosaic. These values correspond to Snellen acuities of 20/17 and 20/25, respectively. To compare the ESCS cone spacing profile with normal subjects, Figure 2.5B shows the Z-scores of the cone spacing in ESCS subjects across different eccentricities. Z-score values are below zero beyond 2° eccentricity in 5 subjects. 10055L has a higher-than-normal Z-score around the fovea (outside of the y-axis range of Figure 2.5B) with normal Z-scores at eccentricities greater than 2°.

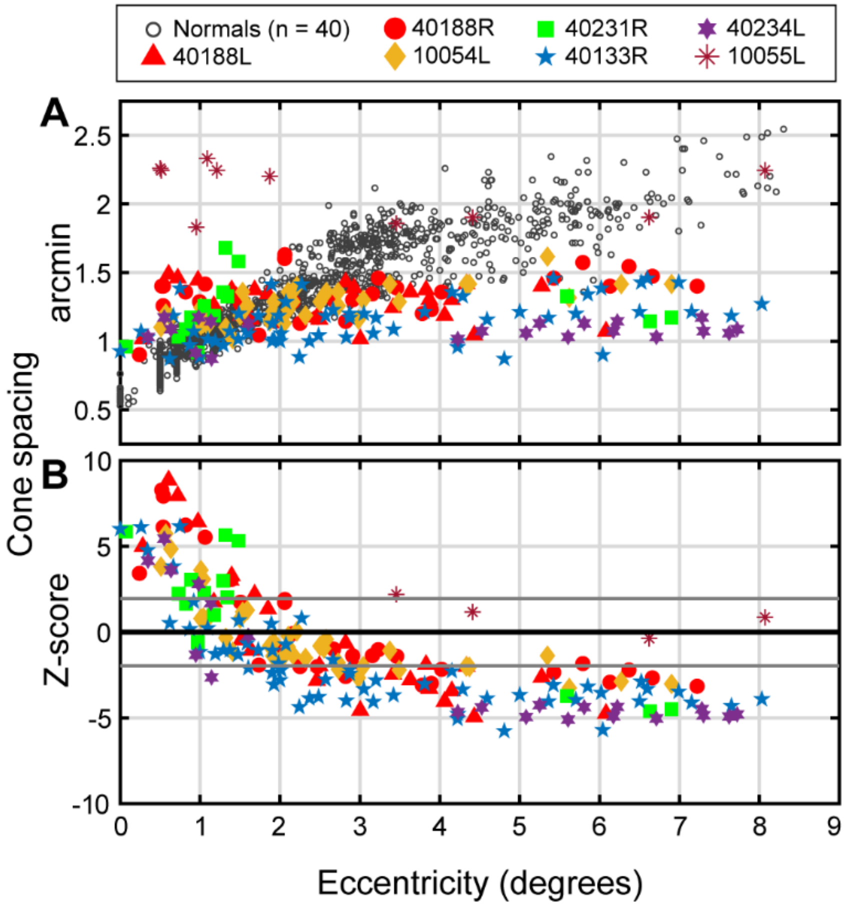

Figure 2.5 ESCS Cone Spacing Analysis

(A) Cone spacing as a function of retinal eccentricity. Normal data (Duncan et al., 2023; Y. Wang et al., 2019) is plotted with black circles on a common eccentricity axis. (B) Cone spacing Z-score as a function of retinal eccentricity. The Z-scores are computed considering retinal locations at four major meridians (Duncan et al., 2023). The horizontal zero line shows a Z-score of 0 and the grey lines show ±1.96 standard deviation from the mean (95% confidence interval). Cone spacing Z-scores outside of the y-axis range (which all come from 10055) are not shown in the plot.

2.4.2 S- and L/M-cone Isolated Visual Acuity

AOSLO retinal images obtained simultaneously with psychophysical testing allow us to recover the trial-by-trial location of stimulus delivery for each test condition from the fovea to 4° eccentricity in the temporal retina (Figure 2.4). Although the stimulus delivery

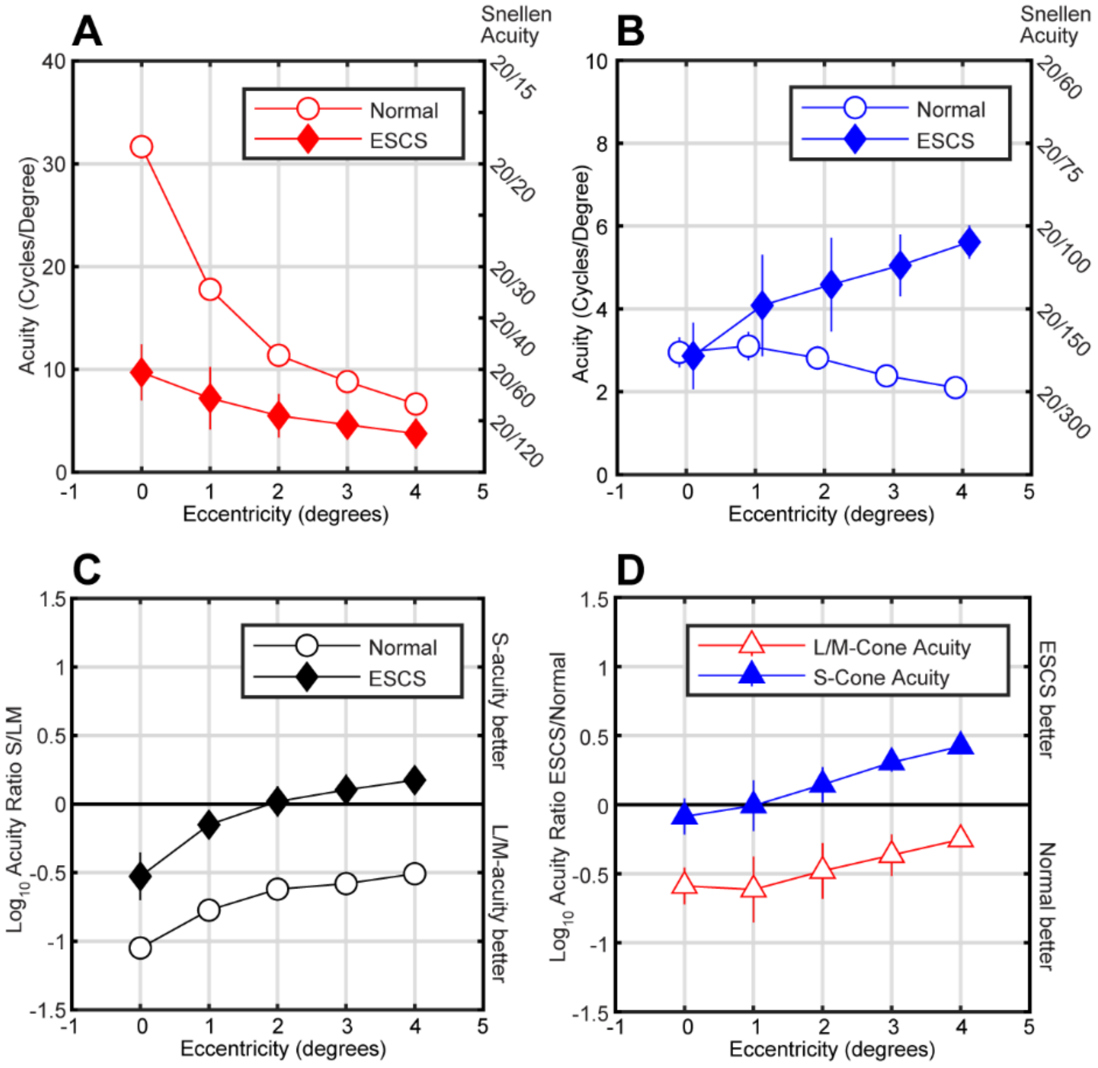

Figure 2.6 ESCS Visual Acuity Analysis

(A) L/M-cone acuity performance as a function of retinal eccentricity in ESCS and normal subjects. Red open circles show averaged L/M-cone acuity in 7 normal subjects and red diamonds show averaged L/M-cone acuity in 5 ESCS subjects. Error bars are standard error of the mean. (B) S-cone acuity performance as a function of retinal eccentricity in ESCS and normal subjects. The Y-axis is adjusted to show low-spatial-frequency region, and data are shifted laterally to minimize overlap. Blue open circles show S-cone acuity in 7 normal subjects, and the blue filled diamonds represent averaged S-cone acuity in 5 ESCS subjects. Error bars are standard error of the mean. (C) Log$_{10}$ Acuity ratio as a function of retinal eccentricity in ESCS and normal subjects. The horizontal zero line represents equal S-cone and L/M-cone acuity. The area above the horizontal zero line shows where S-cone acuity is better than L/M-cone acuity at the targeted eccentricity. Error bars are standard error of the mean. (D) Normalized Log$_{10}$ acuity ratio in cycles per degree. The horizontal zero line represents equal acuity in ESCS and normal subjects. The area above the horizontal zero line shows when ESCS acuity is better than normal subjects.

through the DLP projector was not contingent on eye positions, the regular spacing of the isoline contours confirms that subjects were maintaining their gaze on the fixation target during the psychophysical task, and acuity measures were obtained at the intended eccentricities. Moreover, the stimuli in both conditions appear to be landing on the same part of the retina at all eccentricities except for the fovea, where S-cone-isolating conditions tend to produce larger and sometimes displaced fixation patterns. A similar trend is observed in the foveal S-cone-isolating data from normal subjects (Figure 2.4, top row) and may reflect a behavioral adaptation to the absence of S-cones in the central fovea (Curcio et al., 1991). Due to poor retinal video quality along the horizontal meridians in 40231R from intraretinal cysts, the eye positions of 40231R were not analyzable and thus the retinal image with incomplete fixation plots were not shown in Figure 2.4.

Figure 2.6A shows the average L/M-cone acuity as a function of retinal eccentricity in 7 normal subjects and 5 subjects with ESCS. In all 7 normal subjects, L/M-cone acuity is 20/20 or better at the fovea and declines with increasing eccentricity, consistent with previous findings (Anderson et al., 1991; Rossi & Roorda, 2010). In the ESCS cohort, the average L/M-mediated acuity is about 20/60 at the fovea – reduced approximately threefold compared to normal – and exhibits a monotonic decline across the parafovea, approaching near-normal levels by 4° eccentricity (Figure 2.6A).

The relationship between S-cone-isolating acuity and retinal eccentricity is shown in Figure 2.6B. In normal subjects, the average S-cone acuity is about 20/200 at the fovea and 1° eccentricity, and then declines to 20/300 by 4° eccentricity. The averaged normal S-cone acuity results we obtained at the fovea agree well with previous measurements in normal subjects (Anderson et al., 2002). By contrast, S-cone acuities in the ESCS patients are near normal at the fovea and improve steadily with increasing eccentricity. At 4°, ESCS patients perform nearly three times better than normal subjects measured under the same conditions (Figure 2.6B). In fact, the average S-cone acuity for ESCS subjects (20/107) is similar to the mean L/M-cone acuity in normal subjects (20/90) at the 4° location, while S-cone acuity in normal subjects at 4° is reduced to 20/300.

To compare our subjects' performance more quantitively across the tested eccentricities, we show performance ratios between test conditions (S- vs L/M-cone acuity; Figure 2.6C) and between subject groups (ESCS vs Normal; Figure 2.6D). Figure 2.6C shows the $\log_{10}$ acuity ratio of S-cone acuity against the L/M-cone acuity for normal subjects (open circles) and patients with ESCS (black diamonds). Data below the horizontal zero line indicates that S-cone acuity is worse than L/M-cone acuity, whereas points above the zero line correspond to locations where S-cone acuity is superior to that mediated by L/M-cones. As expected, normal subjects have worse S-cone acuity than L/M-cone acuity at all eccentricities we measured, consistent with the idea that L- and M-cones provide the primary inputs to retinal pathways involved in high acuity vision (Marcos & Navarro, 1997; Thibos et al., 1987; Williams & Coletta, 1987; Zhang et al., 2020). By contrast, in ESCS subjects, the discrepancy between L/M- and S-cone mediated acuity in the central fovea is smaller, and beyond 2° eccentricity, the S-cone pathway slightly outperforms its L/M counterpart. Together, these data suggest S-cones make a greater contribution to the pathway(s) subserving spatial vision throughout the central retina in ESCS.

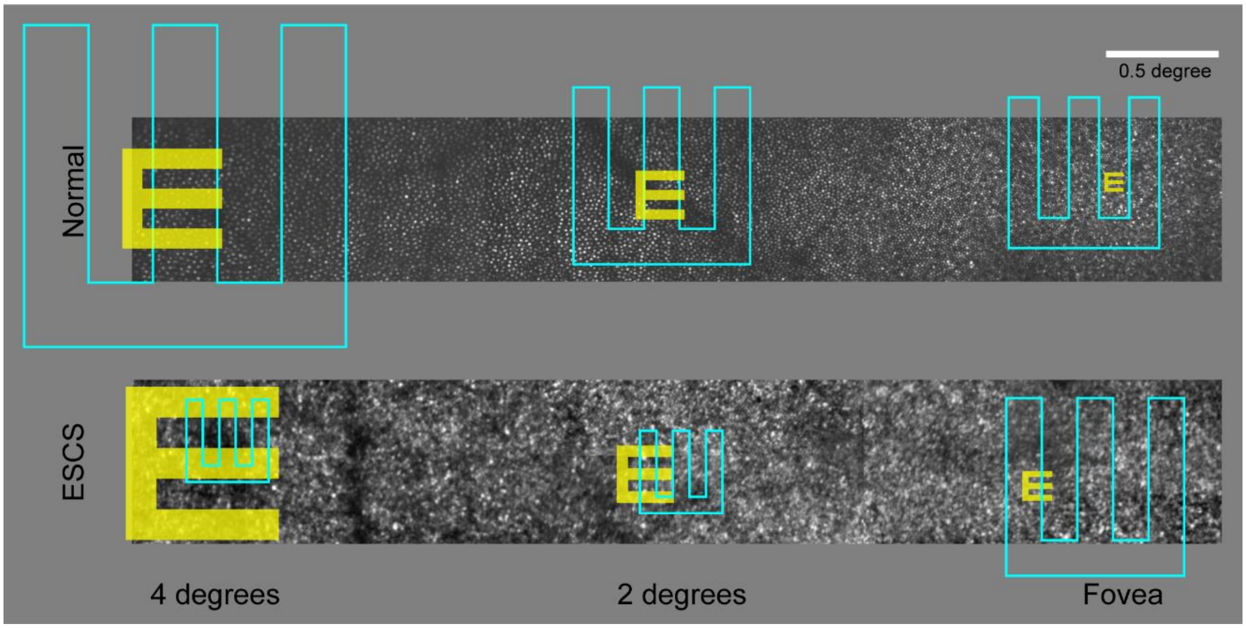

Figure 2.7 Structure-Function Relationship of ESCS

Data of one normal (upper panel) and one ESCS subject (lower panel) are shown. From right to left, the retinal images show the fovea to 4° temporal region. White bar shows 0.5° scale. The acuity threshold letter size of each retinal location and S- and L/M-cone-isolating condition is represented by the cyan and yellow letters, respectively. Each letter E is centered at the stimulus delivery location. In the normal eye (top image), L/M-cone threshold letter size (yellow) is small at fovea and increased with eccentricity; similar trend was seen in S-cone task, but S-cone threshold letter size (cyan) is significantly larger. In an ESCS subject (lower image), L/M-cone acuity threshold size is slightly larger than normal but follows the same trend. Most noticeably, the S-cone acuity of this ESCS subject is worse than normal at fovea but gradually improves from 1° to 4° eccentricity, showing the exact opposite trend as normal S-cone acuity.

Figure 2.6D quantifies ESCS performance relative to normal for the S- and L/M-cone-mediated acuity tasks. Near the fovea, S-cone acuity is similar across the two groups, while L/M-cone acuity is significantly diminished in ESCS compared to normal. At 4° eccentricity, however, the disparity in L/M performance between the two groups appears to be less severe, and ESCS patients exhibit supernormal S-cone acuity. Finally, to illustrate qualitatively how the relationship between structure and function varies between normal subjects and patients with ESCS, Figure 2.7 shows how threshold E letter size for the two cone-isolating conditions scales with outer retinal structure for exemplary subjects from each cohort.

We note here that our L/M-cone acuities measured at the fovea in ESCS are generally lower than the corresponding clinical acuities reported in Table 2.1, although differences in measurement conditions may have contributed to the discrepancies in the performance we observed. Specifically, the acuity stimuli used in the experimental and clinical measurements differed in their spectral content (S-cone-excluding vs. broadband), temporal characteristics (200 milliseconds presentation vs. unlimited viewing), and spatial frequency composition (similar Fourier spectra in the 4AFC task vs. more varied spectra in the ETDRS optotypes (Marmor et al., 1999). Subjects 40231 and 40234 have bilateral macular edema shown in Figure 2, which could have contributed to the poorer L/M-cone foveal acuities compared to the other three subjects with relatively less disrupted foveal architecture (Table 2.1).

2.5 Discussion

While all inherited retinal degenerations are characterized by a progressive loss of one or more specific visual functions, ESCS is unusual in the sense that its atypical phenotype also has the potential to confer a gain in function along another dimension of human vision. We confirm the findings from previous histological (Milam et al., 2002) and imaging studies (Ammar et al., 2021; Roorda et al., 2010) supporting the notion that ESCS retinas are equipped with a surplus of S-cone-like photoreceptors (at the expense of rods and thus scotopic vision). A detailed understanding, however, of how younger ESCS patients capitalize on this excess number of S-cones has until now remained largely unknown, particularly at the cellular scale. Specifically, the functional consequences associated with this unusual phenotype have been studied primarily using electroretinographic (Hood et al., 1995; Marmor, 1989; Marmor et al., 1990, 1999) and psychophysical perimetric techniques (Garafalo et al., 2018; Jacobson et al., 1990; Roman et al., 2019; Sohn et al., 2010), which provide no information about how, or whether, post-excitation mechanisms might leverage the supernormal complement of cones to improve spatial vision.

In this study, we combined high-resolution adaptive optics retinal imaging with simultaneous visual function testing to examine cone topography and spatial vision across the fovea and parafovea in ESCS. Our imaging results reveal subnormal cone densities occurring within the central 2° and supernormal cone densities beyond 2°, out as far as 8° (Figure 2.5A). For L/M-cone-mediated acuity, the largest difference between our study groups was observed at the fovea, where ESCS patients performed roughly threefold worse than the control group (Figure 2.6A). For S-cone-mediated acuity, the ESCS and control groups performed similarly at the fovea and 1°. At greater eccentricities, performance between the two groups diverged, with ESCS patients exhibiting increasingly supernormal acuities out to the largest eccentricity studied (4°; Figure 2.6B). This finding extends the results of Greenstein and colleagues (Greenstein et al., 1996), who found a twofold improvement in S-cone grating acuity at 6° eccentricity in a group of 3 ESCS patients whose cone mosaic topography was unknown. Below we discuss the implications of our results for receptoral and post-receptoral organization in ESCS.

2.5.1 Arrangement of L/M and S-cone Submosaics.

While the abundance of S-cones in the retinas of ESCS patients is well established, the organization of L/M- and S-cone submosaics is less clear, particularly in and around the fovea. Young ESCS patients often have normal color vision, which suggests that L/M-cones are present in some number (Marmor et al., 1999). Clinical visual acuity measurements in ESCS are highly variable between subjects, ranging from 20/20 to 20/1000 depending on different disease stages (de Carvalho et al., 2021). In the normal retina, L/M-cones are concentrated in the foveal center, and acuity is ultimately limited by the L/M-cone mosaic sampling. AOSLO imaging showed reduced foveal cone densities in our ESCS subjects (Figure 2.5A), presumably due to reduced densities of L/M-cones. The reduced photoreceptor density we observed in our retinal images is consistent with the slightly reduced foveal L/M-mediated visual acuities in our ESCS subjects without macular edema (10054, 40133 and 40188; Table 2.1). Unlike L/M-cone acuity, foveal measurements of S-cone acuity in the ESCS group were similar to the normal cohort (Figure 2.6B), suggesting that ESCS retinas develop an S-cone-free foveola similar to that found in normal eyes. Collectively, our imaging and psychophysical results imply that the central fovea in ESCS is characterized by an overall reduction in cone density but features an otherwise normal spectral topography.

Away from the foveal center, L/M-mediated acuity was also worse in the ESCS group compared to normal, although the two curves appeared to converge with increasing eccentricity (Figure 2.6A). While it is tempting to view this confluence as evidence of a relatively normal parafoveal L/M-cone mosaic, it is important to point out that visual acuity at these eccentricities is likely limited by spatial pooling in the midget retinal ganglion cell (mRGC) pathway rather than by the packing density of the cone mosaic (Rossi & Roorda, 2010). As such, our imaging and psychophysical results do not exclude the possibility that the reduction in cone density observed at the fovea does not extend to the L/M-cone submosaic in the parafovea as well. Whether the reduced L/M-cone densities suggested by our data exist from birth or are the consequence of ongoing degeneration is not known, although the progressive loss of L/M-cone function observed in longitudinal perimetry studies support the latter interpretation (Garafalo et al., 2018). In contrast to L/M-cone acuity, S-cone acuities in the ESCS group became increasingly supernormal with increasing eccentricity (Figure 2.6B), presumably due to the rise in cone numbers we observed via high-resolution imaging (Figures 2.4 and 2.5).

The fact that the elevated cone counts in ESCS did not extend to the foveal center is consistent with the histological finding that rod precursors are already excluded from the incipient fovea when the earliest expression of NR2E3 occurs around fetal week 12 (O’Brien et al., 2004). The apparently limited role in NR2E3 for foveal specialization is consistent with a framework wherein the development of the normal trichromatic cone mosaic is initiated prior to rod precursors being misdirected to form the surplus S-cones. This leads to the prediction that the excess S-cones fill in the band of retinal eccentricities normally inhabited by rods. Our data are broadly consistent with this view, which is also supported by previous work that shows cone photoreceptors develop before rods

(Hendrickson et al., 2008; Swaroop et al., 2010), that NR2E3 expression pattern follows the eccentricities normally occupied by rods (Garafalo et al., 2018), and that the topography of S-cone sensitivity in ESCS subjects resembles that of the normal rod system (Hood et al., 1995; Jacobson et al., 1990). Whether the genetic mutations that underpin ESCS interfere with foveal photoreceptor development could be clarified by applying in vivo imaging techniques to characterize cone packing in younger carriers of NR2E3 mutations, whose retinas would presumably be less affected by degeneration. If foveal cone density is normal in younger ESCS patients, that would suggest the primordial cone mosaic develops normally but is then afflicted with degeneration secondary to the aberrant development of rod precursors.

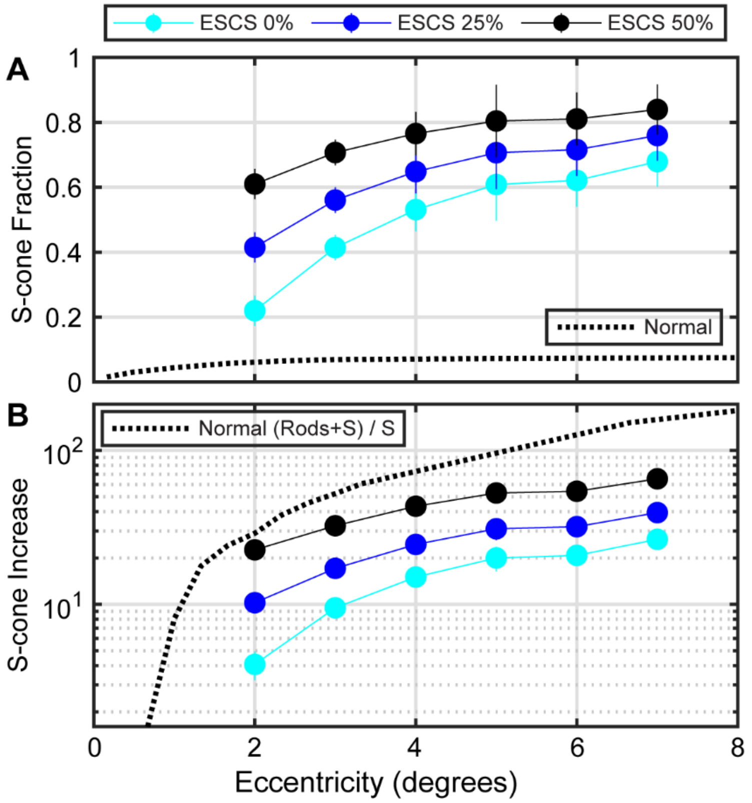

Figure 2.8 S-cone Fraction Change in ESCS

(A) S-cone percentage as a function of retinal eccentricity in different levels of retinal degeneration models. Normal S-cone percentage is shown in the black curve from normal S-cone topography data (Curcio et al., 1991). ESCS subjects show significantly higher S-cone density across all eccentricities modeled with 0% retinal degeneration (cyan), 25% degeneration (blue) and 50% degeneration (black). (B) S-cone density increases as a function of eccentricity with different degrees of retinal degeneration described in (A). Assuming no degeneration, S-cones are increased 28-fold at 7° eccentricity in ESCS subjects. And with 50% degeneration, the S-cones at 7° is increased by 65-fold. If all rods become S-cones, the maximum ratio of S-cone density increase is shown in the black curve calculated from normal photoreceptor topography (Curcio et al., 1990, 1991). Error bars are standard error of the mean.

The measurements of cone spacing we derived from our retinal images enabled us to estimate local cone counts and, by extension, to place bounds on the relative increase in S-cone numbers found in the ESCS retina. Assuming hexagonal cone packing and varying degrees of degeneration of the L/M-cone submosaic, we estimated the overall S-cone percentage and S-cone increase (relative to normal S-cone counts) in ESCS at each eccentricity based on previously reported normal database and methods (Curcio et al., 1991; Duncan et al., 2023; Rossi & Roorda, 2010; Y. Wang et al., 2019). In the normal eye, S-cones make up 5-7% of the cone mosaic at the non-foveal eccentricities studied here (Curcio et al., 1991). By contrast, if no degeneration of the L/M-cone mosaic is assumed in ESCS retinas, we estimate that S-cones constitute 22% of the cone mosaic at 2°; by 7° eccentricity, this number rises to 68% of the receptor array (Figure 2.8A). Note that these estimates should be considered a lower bound since they assume a normal number of L/M-cones – any loss of the L/M-cone mosaic would necessarily push these estimates higher. For comparison, the ESCS histology study reported a 92% S-cone percentage and an abnormally reduced number of L/M-cones. Because ESCS retinas exhibit supernormal parafoveal cone densities, the increase in S-cone numbers relative to normal counts are even more striking: at 7° eccentricity, we estimate the increase in S-cones to be anywhere from 26-fold (assuming no L/M-cone degeneration) to 65-fold (assuming a uniform 50% cone degeneration; Figure 2.8B). These estimates lie within the wide range reported in the literature, which range from the 11-fold increase estimated from the temporal acuity study 30 to the 75-fold increase derived from analysis of full-field ERG responses (Hood et al., 1995).

2.5.2 What is mediating S-cone acuity?

The S-cone acuities obtained from the control subjects in our study are broadly consistent with previous measurements in which a similar blue-on-yellow chromatic adaptation method was used to isolate S-cones (Anderson et al., 2002; Coates & Chung, 2016; Redmond et al., 2013; Zlatkova et al., 2003). Although under normal circumstances the S-cone submosaic is sparsely distributed, S-cone acuity falls well below their sampling limit imposed in the outer retina, implying that resolution in the S-cone pathway is instead limited by the spatial density of post-receptoral neurons – most likely the small bistratified retinal ganglion cells (sbRGCs) that receive direct excitatory input from multiple S-cones (Anderson et al., 2002; Curcio et al., 1991; Dacey, 1993; Dacey & Lee, 1994). In ESCS, we observed a supernormal number of cone photoreceptors – the bulk of which are presumably S-cones – and a resultant increase in S-cone-mediated acuity. The neural basis for this enhanced resolving capacity is not known, although it implies a departure from how S-cone signals are normally processed by post-excitation mechanisms. Here, we present three hypotheses for how supernormal spatial vision in ESCS may arise.

<u>Small bistratified retinal ganglion cell pathway:</u> The sampling limit of the sbRGC mosaic has been shown to agree well with S-cone acuity measurements obtained from 0 to 40° eccentricity (Anderson et al., 2002). If the same pathway supported the supernormal S-

cone acuity we observed in ESCS subjects, there would have to be a concomitant increase in sbRGC density. Such an increase of sbRGCs in ESCS subjects was previously suggested (Greenstein et al., 1996) but not confirmed. Although visual experiences seem to shape the synaptic connections established during retinal development (Dunn et al., 2013), it has also been shown that RGCs develop before photoreceptors and bipolar cells (Xu & Tian, 2004), and RGCs can maintain normal morphology and projections in the absence of normal outer retinal inputs (Mazzoni et al., 2008). Considering the order of retinal development, it seems most likely that normal numbers of sbRGCs develop and differentiate prior to the aberrant specification of photoreceptor fate in ESCS, and that the excess S-cones in these retinas instead gain access to other retinogeniculate pathway(s) with higher spatial resolution.

<u>Direct input to the Midget RGC pathway</u>: Could the supernormal S-cone acuity in ESCS subjects be mediated directly by the midget pathway? Midget RGCs primarily receive input from L- and M-cones and are widely believed to be the cell class meditating achromatic visual acuity across the visual field (Marcos & Navarro, 1997; Rossi & Roorda, 2010; Thibos et al., 1987; Williams & Coletta, 1987). However, anatomical and physiological data from animal models indicate that a small portion of S-cone signals are also carried by the midget RGC pathway (Field et al., 2010; Klug et al., 2003; Patterson et al., 2019). If the weak S-cone signal observed in mRGCs is due to the low proportion of S-cones in a normal eye, then it stands to reason that a larger proportion of S-cones would give rise to a proportional increase in that signal. In fact, our results indicate that S-cone acuity in ESCS starts to approach the L/M-mediated acuities we obtained from our normal cohort at 4° eccentricity, suggesting that two functions might be limited by a common neural pathway in the band of eccentricities where S-cones may predominate in the ESCS retina.

<u>Midget RGCs via the rod pathway:</u> In normal eyes, rod photoreceptors and rod bipolar cells gain access to the cone-driven ganglion cell pathway primary through the connection to the AII amacrine cells (Lee et al., 2019). In patients with ESCS, multifocal ERG findings demonstrate a significant delayed b-wave in response to blue light, suggesting that the signals from the misdirected rod precursors may still feed into the relatively sluggish pathway (Marmor et al., 1999). This implication is supported by histological and electrophysiological evidence from the *nrl* knockout mice, which shows that the excess S-cones establish functional connections with conventional rod-driven circuits (Bush et al., 2019; Strettoi et al., 2004).

The spatial resolution of rod-mediated vision across the central 15°-20° of the retina matches the Nyquist sampling limit of the AII amacrine cells, the coarsest array in the rod pathway, with psychophysical measurements of rod grating acuity reported to be 5-7 cycles/degree at 5° eccentricity (Lee et al., 2019; Wilkinson et al., 2020). This is better than the normal S-cone grating acuity of 2 cycles/degree (Anderson et al., 2002) and the averaged normal S-cone resolution acuity of 2.1 cycles/degree at 4° eccentricity found in our study (Figure 2.6B). In addition, the AII sampling density increases with retinal eccentricities in the central retina, which aligns with the similar trend in the S-cone acuity found in our ESCS subjects (Figure 2.6B). The AII amacrine cell array sampling limit could potentially support the supernormal S-cone acuity found in our ESCS subjects, which reached 5.6 cycles/degree at the 4° temporal retinal location.

The latter two hypotheses presented above require that S-cones in ESCS infiltrate retinal pathways ordinarily driven by L/M-cones. The strongest evidence to support this notion comes from a study in which a flicker perception task was used to examine the temporal characteristics of S-cone processing (Ripamonti et al., 2014). The critical flicker fusion (CFF) frequencies obtained from a cohort of ESCS patients were consistent with a sluggish, but amplified, signal carried by the traditional S-cone pathway (i.e., sbRGCs) existing alongside a sizable, faster, phase-shifted component that could originate in a "luminance" pathway ordinarily driven by L/M-cones. Although the study authors did not speculate on the neural substrate of this achromatic pathway, physiological and psychophysical experiments have demonstrated that primate mRGCs are responsive to fast high-contrast flicker and could contribute psychophysical CFF measurements (Lee et al., 1989; Merigan & Maunsell, 1990). It is also noted that the authors of the temporal contrast sensitivity testing study (Ripamonti et al., 2014) did not rule out the faster phase-shifted component in their temporal contrast sensitivity function as being due to the S-cones connecting to the conventional rod pathway rather than via direct input. To distinguish between these two hypotheses, it would be of interest to measure S-cone mediated acuity in an even younger cohort of ESCS subjects with little to no outer retinal degeneration. Within the central 5° to 20°, scotopic acuity is limited by the AII amacrine cell mosaic, whose spatial sampling is coarser than the mRGC mosaic (Lee et al., 2019). If the S-cone acuity in early-stage ESCS mirrors the Nyquist sampling limit imposed by the AII amacrine cells across the parafovea, it would support the hypothesis that the conventional rod pathway provides an alternate conduit for S-cone signals in ESCS.

2.5.3 How could we learn more?

Previous structural analysis of the ESCS retinas showed an absence of rods, but cones - presumably S-cones - were the dominant cone type in retinal areas outside of the fovea (Ammar et al., 2021; Milam et al., 2002; Roorda et al., 2010). Our structural and functional results further establish that S-cones are in the majority in the parafoveal retina in ESCS. To objectively confirm the abnormal distribution of the L/M and S-cone photoreceptors in ESCS eyes, however, a retinal densitometry (Roorda & Williams, 1999; Sabesan et al., 2015) or an optoretinogram-based cone classification method (Pandiyan et al., 2020; Zhang et al., 2019) could be used. In addition to providing a cellular-scale spectral classification of the outer retina, optoretinography could also be used to characterize the responsivity of individual cones to light flashes (Lassoued et al., 2021), which could aid in directly assaying cellular dysfunction that might be difficult to reveal psychophysically due to potential compensatory adaptations in post-receptoral circuits.

Further study is also needed to confirm the exact retinal wiring that supports the supernormal S-cone acuity we observed in patients with ESCS. New retinal connectomics tools such as serial block-face scanning electron microscopy have been used to elucidate the functional connectivity between cone photoreceptors and their downstream synaptic partners (Patterson et al., 2020; Wool et al., 2019; Zhang et al., 2020). Similar techniques could be applied to ESCS donor tissue to determine whether the abundant S-cone signal is primarily conveyed by an increased number of sbRGCs (which can be readily identified by their morphology), if those short-wavelength signals instead infiltrate ordinarily L/M-driven pathways with higher spatial resolution (i.e., mRGCs), or if novel wiring schemes emerge in the presence of a highly atypical set of outer retinal inputs.

In this study, we used a blue-on-yellow procedure to measure S-cone-isolated visual acuity. While the long-wavelength adapting field is effectively unabsorbed by the S-cone opsin, it can indirectly influence S-cone signals by polarizing cone-opponent circuits downstream, leading to perceptual phenomena such as transient tritanopia (Mollon & Polden, 1977; Stiles, 1949) and changes in the shape of the S-cone contrast sensitivity function (CSF) with increasing background intensity (Humanski & Wilson, 1992; Stromeyer et al., 1984; Swanson, 1996). While transient tritanopia has been demonstrated in ESCS (Kellner et al., 1993), the extent to which S-cone-mediated spatial vision depends on the adaptation state of L- and M-cones is unknown. Examining the S-cone CSF across a range of background intensities may provide additional insights into post-receptoral organization in ESCS.

In conclusion, ESCS subjects exhibit higher than normal S-cone density and supernormal S-cone acuity outside the fovea. The supernormal S-cone acuity in ESCS could indicate retinal plasticity during development where abnormally increased numbers of S-cones re-establish connectivity to the downstream pathways ordinarily driven by L/M-cones.

Contents of this chapter have been published as a journal article:

Wang, Y., Wong, J., Duncan, J. L., Roorda, A., & Tuten, W. S. (2023). Enhanced S-Cone Syndrome: Elevated Cone Counts Confer Supernormal Visual Acuity in the S-Cone Pathway. Investigative Ophthalmology and Visual Science, 64(10). https://doi.org/10.1167/iovs.64.10.17

3 Chapter 3 | Preferred Retinal Locus of Fixation in the S-cone Pathway

3.1 Abstract

The unique anatomy of the fovea is leveraged by the oculomotor system to sample our visual environment with high resolution. Under normal conditions, the preferred retinal locus (PRL) of fixation is in the foveola, but non-foveal PRLs can develop in cases where central vision is lost. The role of S-cone signals in guiding visuomotor behavior is not fully understood. We investigate whether a similar shift in the PRL exists in the S-cone pathway of normal subjects, where a small natural scotoma is present due to the absence of S-cones in the foveola. We also present an analysis of saccadic landing behavior under these same conditions.

We used an adaptive optics scanning laser ophthalmoscope (AOSLO) to record retinal videos while subjects (N = 6) viewed a tumbling-E stimulus presented under L/M- and S-cone isolating conditions through a custom RGB display channel coaligned with the AOSLO raster (as described in Chapter 2). For each condition, the size of the letter E was set to match the subject's acuity threshold measured in a preliminary experiment in Chapter 2. In the main experiment, trials consisted of a 5-second window during which the optotype was presented randomly at 1 of 9 positions in a 2x2 square grid (grid spacing = 0.5°) centered on the imaging raster. Subjects were instructed to direct their gaze at the letter and report its orientation via keypress. Once the response was logged, the stimulus disappeared for 200 ms before moving to a new location, where it was shown until the subject responded again. This process repeated until the 5-second trial concluded. AOSLO videos were recorded during each trial to monitor eye position. For each cone-isolating condition, 60 trials (300 seconds of video) were obtained, corresponding to ~200 stimulus presentations. All trial videos were registered to a seamless retinal map generated using custom software, enabling the determination of the retinal landing points for every stimulus delivery. For each condition, the PRL was defined as the mean stimulated retinal locus during the 233 ms preceding each response. Saccade landing positions were computed from the post-saccadic retinal landing positions one video frame (33 ms) after the saccadic eye movement.

Relative to the L/M-cone PRL, the S-cone PRL was shifted superiorly in most subjects by an average of 9.79 ± 1.57 arcmins. The magnitude of this shift varied between subjects, with smaller shifts observed in subjects who exhibited better S-cone acuities. The average displacement between the L/M- and S-cone saccade PRL was 10.51 ± 1.72 arcmin, similar to that reported previously for fixation. The mean (± SEM) saccade landing areas were 220.66 ± 19.29 arcmin^2 and 735.22 ± 176.41 arcmin^2 for the L/M- and S-cone conditions, respectively ($p<0.01$; paired t test). For both conditions, the post-saccadic isoline area (ISOA) reduced over the course of ~300 ms.

These results suggest there may be heterogeneity in the foveal topography of S-cones in normal individuals, and the retinal locus directed to a target of interest depends on the visual pathway mediating its detection.

3.2 Introduction

The acquisition of visual information is an active process. The oculomotor system directs our gaze to objects in the environment so that they are sampled by the fovea, a specialized retinal region with neuroanatomical features that facilitate the perception of spatial detail. Hallmarks of foveal anatomy include a densely packed array of photoreceptors (Curcio & Allen, 1990; Y. Wang et al., 2019), private-line connections to downstream bipolar and ganglion cells (Zhang et al., 2020), and laterally displaced post-receptoral layers that give rise to its characteristic pit-like appearance (Bringmann et al., 2018; Polyak, 1941; Provis et al., 2013).

The preferred retinal locus (PRL) is the subregion within the fovea used during fixation. The advent of high-resolution retinal imaging and stimulation techniques has enabled precise characterization of the extent to which the PRL co-localizes with other foveal landmarks (Wilk et al., 2017). In the healthy eye, the PRL is usually located within a few arcminutes of the locus of maximum cone density (Putnam et al., 2005; Reiniger et al., 2021; Y. Wang et al., 2019; Wilk et al., 2017), thus ensuring spatial information in the retinal image is sampled near-optimally by the cone mosaic. Further, the PRL is generally robust to the visual task used to measure it (Bowers et al., 2021), is repeatable over time (Kilpeläinen et al., 2021), and exhibits positional symmetry between the right and left eyes (Reiniger et al., 2021). These results indicate the PRL is an important and stable reference point for the oculomotor system, with its development presumably orchestrated to leverage the fine neural grain of the foveola (Poletti et al., 2013).

Characterizing how oculomotor behavior changes when signals from the habitual PRL are no longer available may provide insights into the organization and plasticity of the brain areas involved in controlling fixation (Krauzlis et al., 2017). In patients with central vision loss due to macular disease, for example, a new PRL often forms at an eccentric retinal location (Crossland et al., 2005; White & Bedell, 1990). Likewise, healthy individuals viewing a gaze-contingent display with an artificial central scotoma can learn to fixate eccentrically after a training period (Agaoglu et al., 2022; Kwon et al., 2013; Prahalad & Coates, 2020; Rose & Bex, 2017). In both cases, changes to oculomotor behavior take time to manifest, as the visual system learns to adjust its strategies for visual exploration following the loss of information from the central retina.

Although much attention has been devoted to understanding how pathological disruption of the central visual field affects the PRL, it is interesting to consider that natural blind spots also exist in the healthy retina. For example, a small central scotoma emerges in dim light conditions due to the nonuniform spatial distribution of rod photoreceptors. In stark contrast to cones, rods are largely absent from the central 1.25° (Curcio et al., 1990)

Instead, rod density reaches its peak between 15° and 20° eccentricity, with a slight bias toward the superior meridian (Curcio et al., 1990). Previous work has shown that humans and other primates tend to adjust their gaze direction upwards when performing visual tasks in scotopic light levels. This adjustment places targets on the superior retina and positions the scotoma in the upper visual field (Barash et al., 1998; Goffart et al., 2006; Paulun et al., 2015; Snodderly, 1987). This finding suggests the healthy visual system may be capable of actively adjusting its oculomotor strategies to achieve optimal retinal sampling under the prevailing conditions (Najemnik & Geisler, 2005).

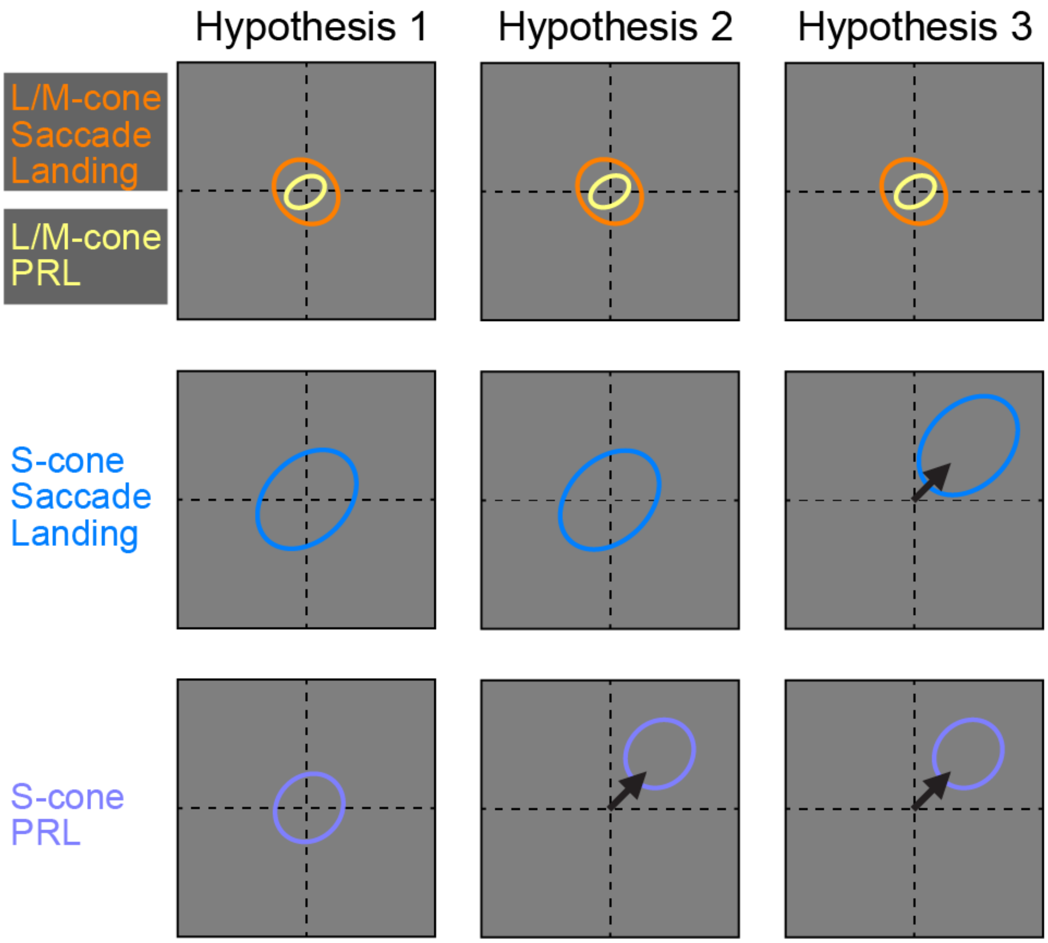

Figure 3.1 Proposed Hypotheses of the Influence of the S-cone System on Saccades and Fixations

The L/M-cone saccade landing position (orange) and L/M-cone PRL (yellow) are centered on the fovea, indicated as (0,0). Hypothesis 1 suggests an alignment of both the S-cone saccade landing (blue) and S-cone PRL (violet) with the L/M-cone PRL. Hypothesis 2 proposes an initial foveating S-cone saccade landing followed by displacing the S-cone PRL. Hypothesis 3 shows an innate S-cone PRL location, directing both S-cone saccade landing and S-cone PRL away from the L/M-PRL.

In this study, we examine the visuomotor consequences of a second natural scotoma associated with the human fovea, one that is roughly an order of magnitude smaller than the foveal rod-free zone. Within the central ~20 arcmin, short-wavelength-sensitive (S) cone photoreceptors are thought to be excluded in favor of long- (L) and middle-wavelength (M) sensitive cones which provide input to the high-resolution parvocellular pathway. Previous investigators have drawn an explicit link between the so-called “fixation area” of the foveola and the tritanopic zone, implying the habitual PRL would be located in a region devoid of S-cones (Wald, 1967).

It is currently unknown whether the PRL measured under S-cone-isolating conditions would differ from that obtained using targets that selectively activate L and M cones. We propose three hypotheses regarding the oculomotor behavior mediated by the S-cone system (Figure 3.1). Hypothesis 1 suggests that there are no differences in saccade landing positions or preferred retinal locus (PRL) between L/M-cone and S-cone conditions. White and colleagues examined saccadic eye movements made to near peripheral (3° to 12° eccentricity) equiluminant targets with chromaticities situated along the four cardinal axes of DKL color space (White et al., 2006). Compared to saccades made to luminance-defined targets, they found no systematic difference in the accuracy of visually guided eye movements to stimuli on the S-cone-isolating DKL axis, which may match the first hypothesis, although the spatial accuracy of the video-based eye tracker used in the study may have been too coarse to reveal subtle functional differences associated with the minute S-cone-free zone. Hypothesis 2 proposes that the eye will initially make a foveating saccade upon stimulation with an S-cone stimulus but will eventually land on a non-foveal location for fixation. This phenomenon was observed in studies utilizing artificial scotoma induced by a gaze-contingent display in normal-sighted individuals (Agaoglu et al., 2022) . Hypothesis 3 suggests that both the saccade landing positions and PRL locations are eccentric, implying the involvement of a separate chromatic system for detection and initiating eye movements.

In the present study, we tracked retinal position with high resolution using an adaptive optics scanning laser ophthalmoscope (AOSLO; Roorda et al., 2002) while color-normal subjects completed a visual-search-and-identification task. Specifically, subjects were asked to make eye movements to identify the orientation of tumbling-E stimuli presented in the central visual field. The retinal landing positions of the tumbling-E stimuli during the visual-search-and-identification task were used to determine the saccade landing endpoints and pre-response PRLs for targets that favored either the L/M- or S-cone pathways.

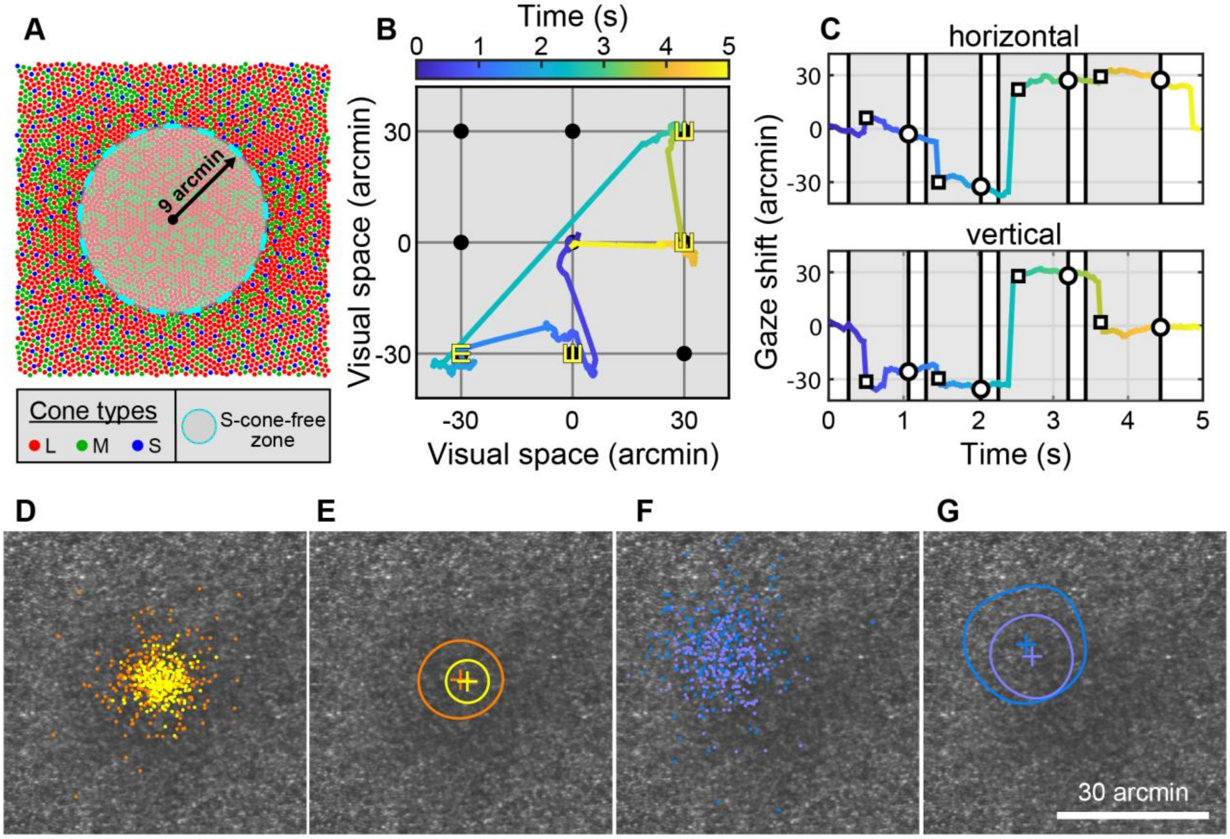

Figure 3.2 S-cone Fixation Experiment and Data Analysis Pipeline

(A) An artificially representative foveal cone mosaic displaying L-cones (red), M-cones (green), and S-cones (blue). Suggested 0.3° S-cone-free zone in enclosed with a cyan dashed circle. (B) Spatial coordinates for psychophysical experiments while using scanning laser ophthalmoscopy for retinal video recording. Subjects (N = 6) made small saccades to tumbling-E stimuli within a 2x2 square grid (0.5° spacing). Tumbling-E stimuli (yellow, drawn to scale) appear from time 1 to 4 with orientation and location indicated, each labeled with colors corresponding to eye traces in C. (C) Eye traces in horizontal (x, upper panel) and vertical (y, lower panel) directions analyzed from retinal video stabilization. Grey-shaded areas indicate stimulus duration. The left edge of the grey rectangle marks the frame of stimulus onset, while the black circle on the right edge indicates stimulus offset triggered by a keyboard response, defined as the frame of response. Black squares represent detected maximal eye movements, indicating the frame of saccade. The lower row D-G shows the retinal locations analysis overlayed with a retinal map from subject 20114R. (D) Scatter plots show all data points of L/M-cone condition with yellow representing PRL locations, and orange showing the saccade landing endpoints. (E) Application of 68% isoline contour with weighted centroid method to data points with a contour encompassing 68% of data, and the centroid location identified by a cross. (F) Saccade landing endpoints (blue) and PRL locations (violet) of the S-cone isolating condition. (G) Overlay of isoline contour and centroid locations of S-cone PRL (violet) and saccade landing endpoints (blue).

3.3 Methods

3.3.1 Human subjects

Six participants without any known medical or ocular conditions were enrolled in the study and underwent imaging and psychophysical procedures at the University of California, Berkeley. All research activities adhered to the ethical principles outlined in the 2008 Declaration of Helsinki. Prior to their participation, each subject provided informed consent, which included an explanation of the study's objectives and potential outcomes. The research protocol received approval from the Institutional Review Board at the University of California, Berkeley.

3.3.2 Experimental procedures

All subjects were dilated with 1% tropicamide and 2.5% phenylephrine in the study eye before retinal imaging and psychophysical experiments.

We developed the psychophysical paradigm with a modified high-resolution (136 pixels/degree) digital light processing (DLP) projector (TI DLP LightCrafter 4500, Texas Instruments Inc., Dallas, TX, USA) that was co-aligned with an adaptive optics scanning laser ophthalmoscope (Wang et al., 2023b). Utilizing the difference in spectral sensitivities between S-cones and L/M-cones, each pathway was isolated to study the fixation behavior Coates & Chung, 2016; Wang et al., 2023b. The retinal videos were recorded during the psychophysical experiments using AOSLO with a frame rate of 30 Hz. The wavefront sensing laser was 940 nm, and the imaging light was 840 nm. All experiment scripts controlling the projector screen were developed in MATLAB (Mathworks, Natick, MA) and Psychtoolbox (Brainard, 1997).

Subject ID	Eye	Visit Date	S-acuity logMAR	S-PRL Contour arcmin^2	LM-PRL Contour arcmin^2	S-PRL displacement arcmin	S-sac Contour arcmin^2	LM-sac Contour arcmin^2	S-sac displacement arcmin
10001	Right	12/2022	0.82	165.37	59.50	2.35	309.54	176.19	3.30
10003	Left	11/2022	1.02	756.54	52.16	12.05	1486.7	225.45	13.60
20114	Right	12/2022	1.06	335.28	45.39	9.90	489.33	153.56	11.44
20212	Left	11/2022	0.94	472.74	99.58	10.92	725.18	276.02	13.94
20217	Left	10/2022	1.00	399.47	156.85	13.25	950.24	257.91	13.10
20230	Right	11/2022	0.98	425.16	81.14	10.24	450.45	234.86	7.70

Table 3.1 Comprehensive Data from One Visit of All Six Subjects

Information includes subject ID, study eye, S-cone acuity in logMAR, S-cone and L/M-cone PRL 68% contour area size, displacement between S- and L/M-cone PRL centroid locations, and S-cone and L/M-cone saccade 68% contour area sizes, along with the displacement of the saccade landing centroid location.

As outlined previously in Chapters 2 and 3, in the S-cone-isolating condition, the blue letter E optotype was presented using a high-resolution projector display, accompanied by adapting light from an external fiber illuminator to desensitize the L/M-cones. To achieve L/M-cone desensitization for the experiment involving S-cone-isolating targets, subjects adapted to a background yellow light generated by passing broadband light from a fiber optic illuminator through a narrowband filter (λcenter = 580 nm, FB580-10, Thorlabs Inc., Newton, NJ, USA) for 60 seconds before each experiment block. In the L/M-cone-isolating condition, a broad-band white letter E was projected from the display, filtered through a long-pass yellow Wratten filter. To address longitudinal chromatic aberration, the focus of the projector targets under different color conditions was optimized using an electrically tunable liquid OptoTune lens (EL-3-10, Optotune Switzerland AG, Dietikon, Switzerland). Transverse chromatic aberrations were subjectively measured during the final visit by aligning a colored target (2x2 grid pattern) in the projector with a decrement target (a black cross) in the imaging raster five times. The average displacement between the yellow and blue projector targets during this assessment was recorded as the subjective transverse chromatic aberration (TCA) for each subject. The S-cone acuity threshold was measured during the first visit of the fixation experiment or previously measured in the study described in Chapter 2 (Wang et al., 2023b).

At the beginning of the experiment, the subject used a keyboard to subjectively center a grid target from the projector with another alignment target from the 1.4° AOSLO raster to ensure the centration and alignment of imaging and stimulus paths. Upon initiating the trial, a blue Tumbling-E target with an adapting yellow background was utilized to selectively target S-cones. The adaptive optics ophthalmoscope recorded retinal videos as normal subjects (N = 6) made small saccadic eye movements to observe a tumbling-E stimulus appearing at random locations within a 2 x 2 square grid with 0.5° spacing. The stimulus remained visible until the subject reported the letter orientation via keypress. Subsequently, the target moved to a new random location within the central 1° field. The same psychophysical paradigm was applied for the L/M-cone isolating condition, with adjustments to the stimulus profile targeting L/M-cones exclusively (threshold letter size for L/M-cones and wavelength profile outside of the S-cone sensitivity curve). Temporal synchronization of projector target delivery and eye motions was achieved through a digital marker added to the AOSLO video frames corresponding to the projector stimulus onset and keyboard press, respectively.

An additional control experiment was added at the last visit of 5 subjects when the S-cone-targeted letter size was interleaved randomly using the subject's own S-cone acuity threshold size (20/200 on average) with a smaller size of 20/130 (threshold of subject 10001R). A total of 60 five-second videos were collected for each cone-isolating condition for most visits. 120 five-second videos were collected in the S-cone condition using interleaved letter sizes.

3.3.3 Data Analysis

Following each experiment, the positions of stimuli were recorded in a MATLAB file, documenting the target location that initiated saccadic eye movement. Retinal videos captured during each experiment were utilized to extract eye position traces and pinpoint stimuli in retinal coordinates.

A specialized software, Retinal-based Simultaneous Localization and Mapping (R-SLAM), as described by Shenoy and colleagues, was employed to generate a seamless 3° retinal map (Shenoy et al., 2021). The second generation of R-SLAM facilitated the stabilization of multiple videos onto a common retinal map, producing output displaying frame-to-frame eye position displacements.

The duration from trial onset to keyboard response varied across trials for each stimulus delivery. The first saccade frame was identified by the maximal frame-to-frame displacement in the first half of each stimulus duration. Saccade landing positions were computed using the eye positions of one frame immediately after the saccade frame. Preferred retinal locus (PRL) analysis encompassed 5 frames (167 ms) during each stimulus delivery, with the selected frames being 2 frames prior to the response frame to reduce noise observed at the trial's conclusion. The average of these 5 frames was employed to compute the PRL, representing one location per stimulus delivery.

Saccade landing positions can be noisy and variable immediately after the first saccade, which is identified from maximal retinal motion in the 30 Hz video. However, the first frame after the saccade is crucial for analyzing saccade landing endpoints. Fixation stability was considered when determining the number and selection of frames for fixation PRL analysis per stimulus. Subjects tended to drift their gaze as they input their response via keyboard press, resulting in larger ISOA from 0 to 2 frames before response, as shown in Figure 3.3. Averaging 5 frames per stimulus delivery demonstrated better fixation stability compared to including only 1 frame, a trend observed in both the L/M-cone (Figure 3.3, top panel) and S-cone (Figure 3.3, lower panel).

As described above, the eye positions for saccade landing endpoints were determined immediately following the initial saccade, and fixation locations were identified just before the subject's response. For each condition (saccade versus fixation, L/M- versus S-cone), around 200 eye positions (one position per stimulus delivery) were analyzed. The saccade landing PRL and fixation PRL locations were calculated by processing the eye position density map with a 2-D Gaussian filter with a fixed 5-arcmin smoothing size. A non-uniform contour was fitted to encircle 68% of the eye positions, and the centroid location of these eye positions within the contour was computed to determine the PRL locations. The 68% contour was also used to calculate the isoline area (ISOA) as described previously (Bowers et al., 2021; Castet & Crossland, 2012). The ISOA contours and centroid locations of saccade landing positions and fixation PRLs in each cone-isolating condition were visually presented and overlaid on the seamless retinal map, depicting the locations in retinal coordinates (created using Illustrator; Adobe Systems, Inc, Mountain View, CA, USA). The fixation displacement between L/M-cone and S-cone conditions, as well as between saccade landing and PRL locations, was quantified by measuring the distance between the centroid locations. Additionally, linear regression of

S-cone acuity and the displacements in saccade landing PRL and fixation PRL was performed using the Pearson correlation function in MATLAB.

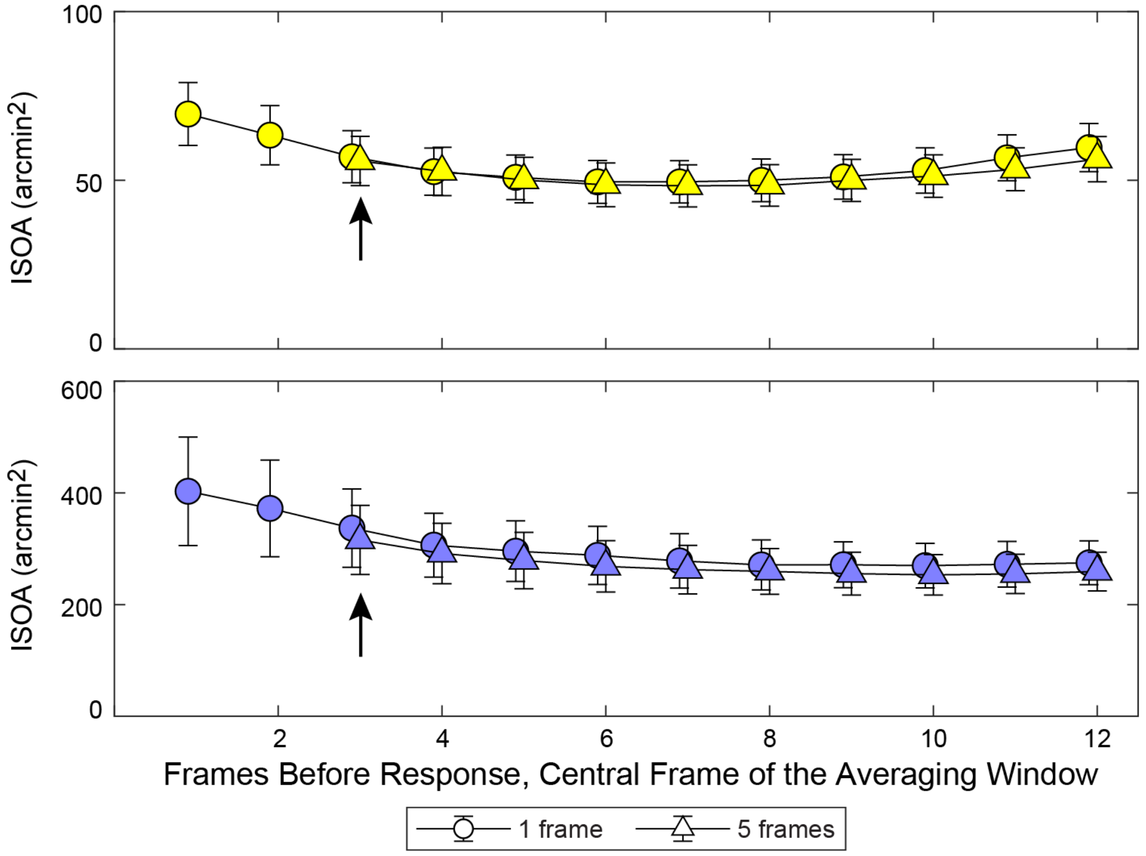

Figure 3.3 Isoline Area Size with Different Frame Sample Sizes

The Isoline Area Size (ISOA) was analyzed as a function of different frame sample sizes to determine the optimal number of frames for fixation PRL analysis per stimulus. The ISOA was largest at the response moment (0 on the x-axis). When analyzing just 1 frame per stimulus, the ISOA started to stabilize after looking back at least 2 frames. Additionally, averaging 5 frames showed better fixation stability compared to including only 1 frame. This trend was consistent in both the L/M-cone (top panel) and S-cone (lower panel) conditions. The black arrows indicate the middle frame of the 5 frames used in the PRL analysis.

3.4 Results

Table 3.1 presents comprehensive data from one visit of all six subjects, encompassing subject ID, study eye, S-cone acuity in logMAR, S-cone and L/M-cone PRL ISOA, displacement between S- and L/M-cone centroid PRL locations, and S-cone and L/M-cone saccade ISOA, along with the displacement of the saccade centroid location.

The average threshold letter size for S-cones in 6 normal subjects was 47.3 ± 3.43 arcminutes (Mean ± SEM), corresponding to a logMAR of 0.970 ± 0.034 (Mean ± SEM). Additionally, the average threshold letter size for L/M-cones was 5.88 ± 0.67 arcminutes (Mean ± SEM), with a logMAR of 0.063 ± 0.037 (Mean ± SEM).

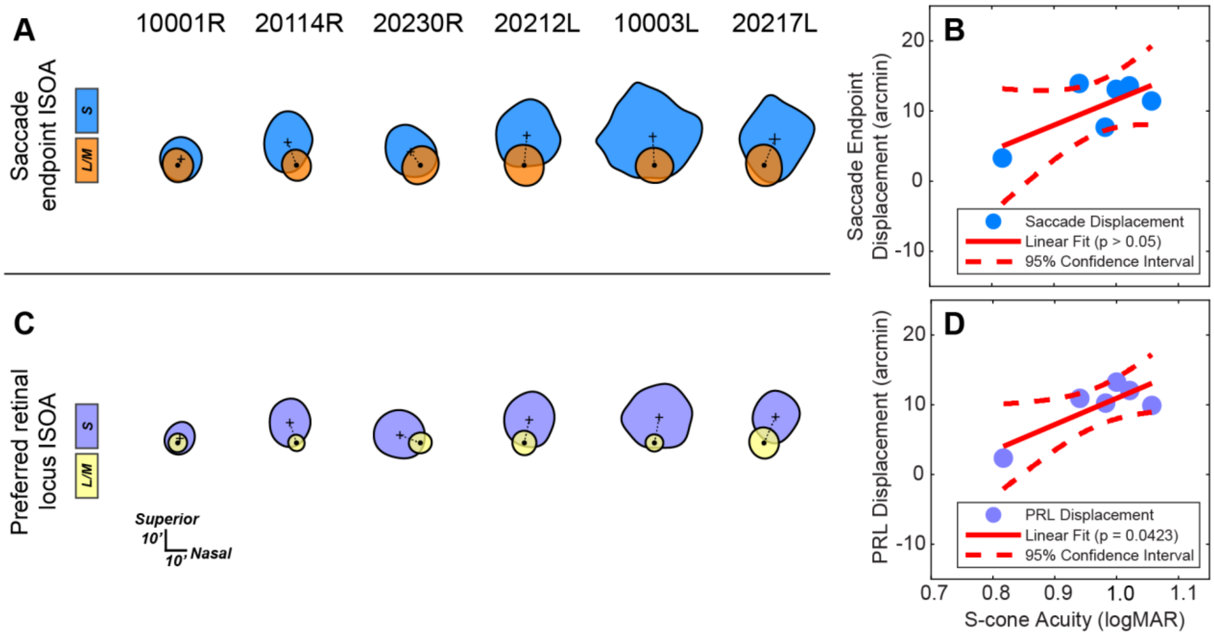

Figure 3.4 Results of Saccade Landing and PRL from one 2022 Visit

(A) Saccade landing 68% isoline area (ISOA) contours for L/M-cone (orange) and S-cone (blue) conditions are centered on the L/M-saccade endpoint centroid, with a black cross indicating the centroid location of the S-cone saccade landing position. (B) Linear regression plot illustrating the relationship between S-cone acuity in LogMAR and S-cone saccade endpoint displacement using Pearson correlation. The solid red line indicates the linear fit (not statistically significant), and dashed curved red lines represent the 95% confidence intervals. (C) PRL 68% ISOA contours for L/M-cone (yellow) and S-cone (violet) conditions are centered on the L/M-PRL centroid location, with a black cross indicating the centroid location of the S-cone PRL. (D) Linear regression plot showing the correlation between S-cone acuity in LogMAR and S-cone PRL displacement from L/M-cone PRL using Pearson correlation. The solid red line indicates the statistically significant linear fit, with dashed curved red lines representing the 95% confidence intervals.

Figure 3.2D-G shows the retinal location analysis from one visit of subject 20114R. In Figure 3.2D, the scatter plot illustrates the distribution of L/M-cone fixation PRL locations (yellow dots) and L/M-cone saccade landing positions (orange). Simplified contour plots with centroid locations (cross) for L/M-cone saccade landing position (orange) and PRL location (yellow) are presented in Figure 3.2 E, revealing significant overlap and minimal displacement. A similar pattern is observed in the S-cone condition between saccade landing endpoints in blue and PRL locations in violet (Figure 3.2F&G).

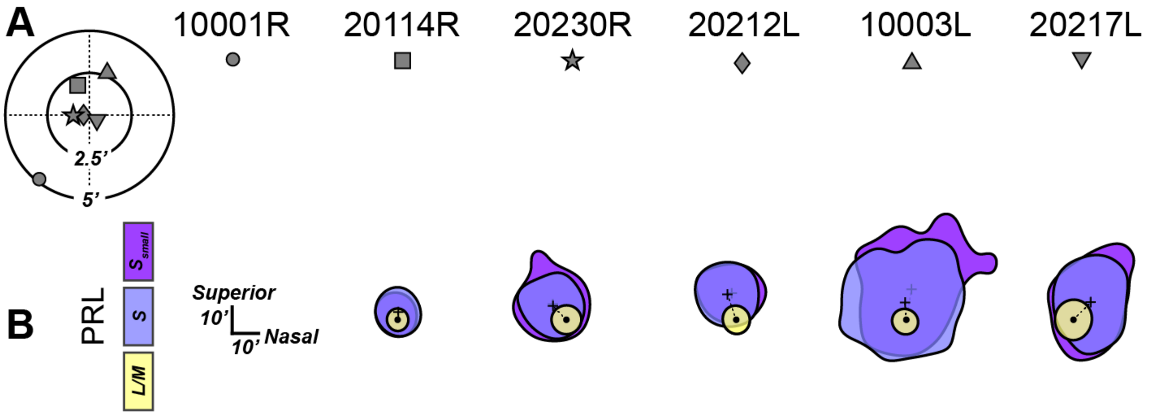

Figure 3.5 Results of Control Experiment using Interleaved S-cone Letter Sizes

(A) The left figure illustrates the transverse chromatic aberration subjectively measured from each subject during a control visit in October 2023. (B) The overlay depicts S-cone PRL contour and centroid locations measured with interleaving letter sizes of the subject’s threshold S-cone letter size (violet) and a small S-cone letter size from 10001R (purple). Subject 10001R did not participate in this task.

Figure 3.4A & C visually represents PRL and saccade landing displacements from one visit across all 6 subjects, same visit shown in Table 3.1. Figure 3.4A illustrates the saccade landing endpoints of each subject, with the L/M-cone condition represented in orange and the S-cone condition in blue. The averaged size of the of L/M-cone saccade landing positions (orange) contours is 220.66 ± 19.29 arcminutes^2. The S-cone saccade landing positions (blue) are superiorly displaced from the L/M-cone saccade landing positions, with a mean displacement of 10.51 ± 1.72 arcminutes and a 68% isoline contour size of 735.22 ± 176.41 arcminutes^2. The 68% ISOA of the S-cone saccade landing positions is significantly larger than the L/M-cone saccade ISOA (Paired t-test $p=0.0288$). The linear regression analysis between saccade landing displacement and S-cone LogMAR does not reveal statistical significance (Figure 3.4B).

Figure 3.4C shows the relative displacement between the L/M-cone PRL (yellow) and sPRL (violet). The L/M-cone PRL is situated in the foveal region, with consistent fixation stability (L/M-PRL ISOA: 83.44 ± 16.98 arcminutes^2) among all subjects. In contrast, the sPRL location (violet cross) is superiorly displaced in all subjects, accompanied by variable S-cone 68% contour (violet) sizes (sPRL ISOA: 425.76 ± 79.23 arcminutes^2). The sizes of the PRL ISOA contours between LM-PRL and sPRL are significantly different (Paired t-test $p=0.0085$). The mean displacement between L/M-cone and sPRL centroid locations is 9.79 ± 1.57 arcminutes. This displacement magnitude is significantly correlated with S-cone-mediated logMAR (Pearson correlation, $R^2 = 0.605$; $p=0.0423$), with smaller shifts observed in subjects exhibiting better S-cone acuities (Figure 3.4D).

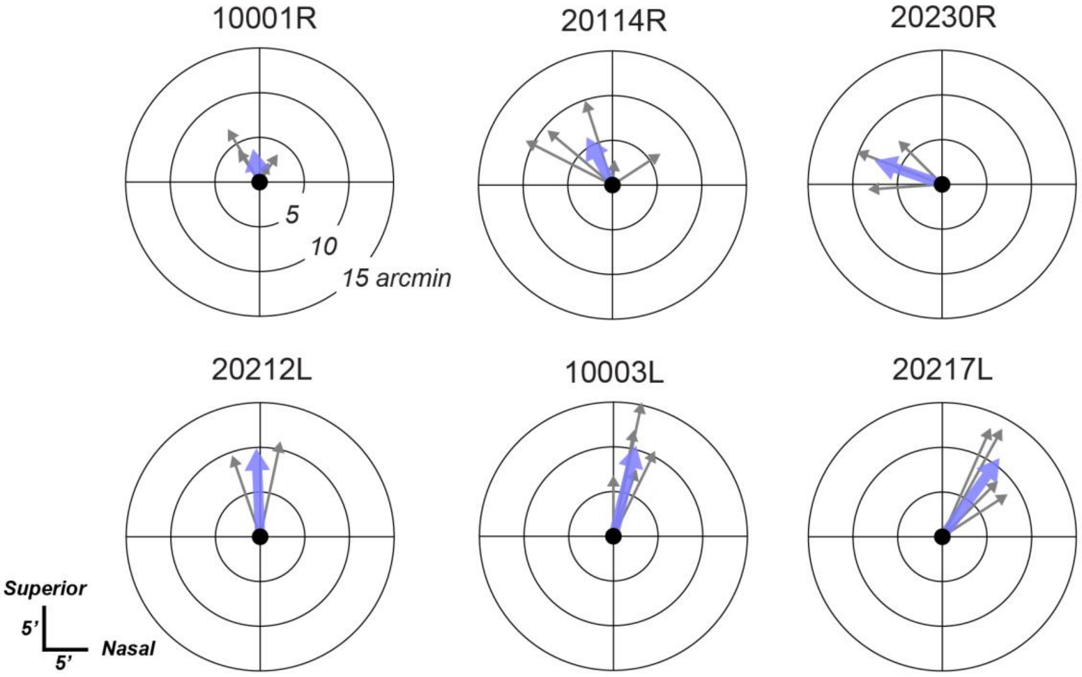

Figure 3.6 The Illustration of PRL Displacement from All Visits

Data from left eyes were mirrored to align with the direction on the scale (rightward-nasal). Concentric rings represent retinal eccentricity in 5-arcmin steps, with the L/M-cone PRL as the center. Each grey arrow represents sPRL displacement from one experiment date, spanning from 2021 to 2023. Violet arrows denote the mean vector for each subject, indicating the average S-cone PRL displacement magnitude and direction across all visits.

To investigate whether letter size could influence sPRL displacement, a control experiment was conducted during the final visit in 2023 (Figure 3.5B). In this experiment, five normal subjects performed the S-cone fixation task with interleaved letter sizes: their own threshold S-cone letter size (approximately 20/200) and 10001R's S-cone letter size (MAR=6.56, 20/130 Snellen letter). The average percentage of correctly identifying letter orientation visualizing the threshold letter size versus the small letter size was 77.38% and 53.45%, respectively. The sPRL contour with small letter size (purple) overlaying with the threshold letter condition (violet), showing largely overlapping fixation areas between two conditions. The appearance of the sPRL displacement and its 68% contour was similar to that observed during the 2022 visit (Figure 3.4C). The Transverse Chromatic Aberration (TCA) measurement performed in all six subjects included in Figure 3.5A shows that such S-cone displacement is not driven by the TCA effect between yellow and blue stimuli.

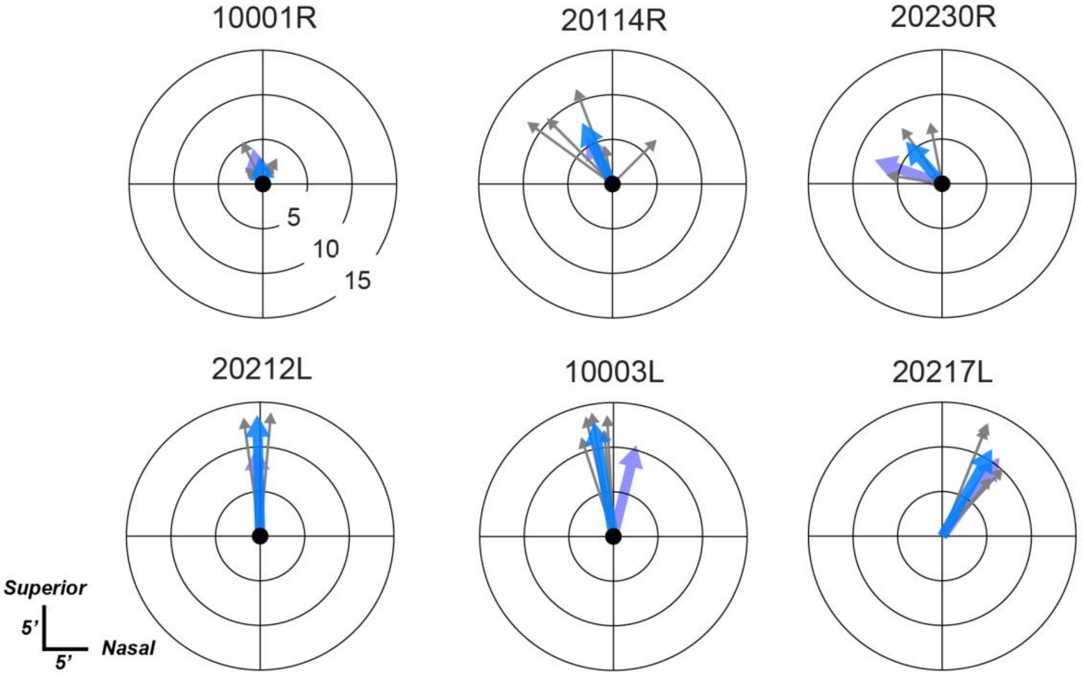

Figure 3.7 The Illustration of Saccade Landing Endpoint from All Visits

Data from left eyes were mirrored to align with the direction on the scale (rightward-nasal). Concentric rings represent retinal eccentricity, with the fovea as the center. Each grey arrow represents S-saccade landing displacement from each experiment date, spanning from 2021 to 2023. Blue arrows indicate the mean vector for each subject, representing the average S-cone saccade landing displacement magnitude and direction across all visits. Additionally, the averaged S-cone PRL displacement (violet arrow), as reported in Figure 3, is retained in these plots, demonstrating consistent superior displacement in both the saccade landing and PRL comparison between L/M- and S-cone conditions.

The repeatability of observed findings was assessed by measuring sPRL displacement across at least two visits in all subjects, conducted between 2021 and 2023, with a minimum one-month interval between visits. Figure 3.6 visually represents the sPRL displacement data from all visits. Grey arrows in the figure depict the sPRL displacement for each visit, with the L/M-cone PRL location measured at the same session as the reference point. The violet arrow illustrates the vector average of all visits. Notably, all subjects consistently exhibit superior displacement of the sPRL. Furthermore, the repeatability of saccade landing endpoints also demonstrated consistency across different visits, with the vector average (blue arrows) indicating superior displacement, as shown in Figure 3.7.

3.5 Discussion

Our study investigated the fixation behavior in the isolated S-cone pathway, in which we found superiorly displaced S-cone PRL as well as S-cone saccade landing position when comparing with the L/M-cone, luminance pathway. The magnitude of the S-cone PRL displacement was variable among subjects and significantly correlated with individual variation in S-cone acuity. The S-cone saccade landing position was spatially coincident with the S-cone PRL and therefore displaced from the L/M-cone PRL.

Is the displacement of the S-cone PRL genuine?

Subjective measurement of transverse chromatic aberration (TCA) revealed minimal spatial displacement between S-cone and L/M-cone targets, affirming that the observed PRL displacement is not attributable to TCA (Figure 3.5A).

The S-cone letter size was, on average, ten times larger than the L/M-cone target, with individual variations in S-cone threshold letter sizes ranging from 33 to 57 arcminutes. In the final visit for five out of six subjects, S-cone fixation behavior was assessed by interleaving the smallest 33 arcmin letter (20/130 Snellen size) with the subject's own threshold letter during the experiment. When analyzed separately, the S-cone PRL locations using both letter sizes were largely consistent (Figure 3.5B).

Moreover, all six individuals repeated the experiment at least six months after their initial visit, demonstrating consistent results for both S-cone PRL locations and S-cone saccade landing positions.

Why is S-cone PRL superiorly displaced?

Normal PRLs do not coincide with the area of peak cone density at the fovea, showing an average displacement of 5-6 arcminutes, more often superior than inferior (Reiniger et al., 2021; Y. Wang et al., 2019). Eccentric PRLs were investigated in patients with macular diseases that resulted in central vision loss, revealing that the eccentric PRL developed after the onset of central vision loss most showed superior displacement from the lesion areas (Crossland et al., 2005b; Greenstein et al., 2008; Krishnan & Bedell, 2018; Messias et al., 2007; Reinhard et al., 2007; Rohrschneider et al., 2008; Timberlake et al., 2005; Verdina et al., 2017). These studies show considerable individual variability in patients with different sizes of macular lesions and disease stages. The structure-function relationship of eccentric PRL in patients with central vision loss were not fully understood as the location of PRL is not always correlated with retinal sensitivity or visual acuity (Greenstein et al., 2008; Krishnan & Bedell, 2018; Verdina et al., 2017).

The S-cone PRL in our subject cohort consistently exhibited a superior or superior temporal displacement. Histological examination of human donor retinas revealed a 0.3°

S-cone-free zone (Curcio et al., 1991). On the horizontal meridian, S-cone density is higher in the temporal meridian compared to the nasal, and vertically, the superior retina has a greater S-cone density than the inferior retina (Curcio et al., 1991). While a recent publication utilizing adaptive optics optoretinography to classify cone photoreceptor types near the fovea did not observe such meridional differences in S-cone density (Schleufer et al., 2023), the tendency for the sPRL to be displaced superiorly could be attributed to the spatial distributions of S-cones around the fovea, possibly indicating an area of the highest density of S-cones immediately outside the S-cone-free zone.

Other studies investigating fixation behaviors under scotopic conditions, where a natural functional scotoma (rod-free zone) exists, have observed an upward shift in fixation location during visual tasks in both humans (Paulun et al., 2015) and Macaca fascicularis monkeys (Barash et al., 1998). Two possible hypotheses are proposed to explain this upward shift in scotopic conditions: differences in visual capabilities and oculomotor control. Barash and colleagues suggested that the superior region in the parafovea, characterized by the highest density of rods (a rod hotspot), likely possesses enhanced visual capacity for scotopic vision compared to other meridians (Barash et al., 1998).

Why does the S-cone saccade landing positions spatially coincide with S-cone PRL, but not with the L/M-PRL?

The saccadic eye movement is known to be generated and controlled by the superior colliculus (SC), an essential structure in the midbrain involved in the visual control of eye movements (Dorris et al., 1997). The neurons in the SC are organized topographically, with specialized regions in the SC corresponding to specific areas of the visual field (Lock et al., 2003). As a visual target was recognized, based on the location in the visual field and the characteristics of this target, specific neurons in the SC were activated and would generate motor commands to initiate appropriate saccadic eye movements. Other regions of the brain such as oculomotor nuclei in the brainstem, were communicated and coordinated to control the eye movement precisely. It was previously believed that the signals transmitted by the S-cones were invisible to the SC neurons due to the lack of direct projection from the color-opponent cells to the SC shown in monkey studies (De Monasterio, 1978; Marrocco & Li, 1977; Schiller & Malpeli, 1977). Consequently, the absence of direct projection suggested that S-cone-isolating targets might not induce the initiation and precise adjustment of saccadic eye movements. However, S-cone stimuli could induce normal attentional effect, indicating that a direct collicular pathway was not required in the involuntary attentional shifts (Sumner et al., 2002). Furthermore, studies have demonstrated that even S-cones signals which bypassed the retinotectal pathway could cause saccade distraction, or the Remote Distractor Effect (RDE), contrary to the prior understanding that only signals within the retinotectal pathway contributed to saccade distraction (Bompas & Sumner, 2009).

3.6 Conclusion

The PRL and saccade landing mediated by S-cone pathway are both superiorly displaced, although the magnitude of this shift varied between subjects. These results suggest there may be heterogeneity in the foveal topography of S-cones in normal individuals. The S-cone saccade landing positions coincide with the S-cone PRL instead of the L/M-cone PRL suggest that the S-cone system mediates its own stimulus detection, and saccade initiation.

Contents of this chapter have been published as conference abstracts:

Wang, Y., Wang, C., Ng, R., Tuten, W. S. (2023).High-Resolution Assessment of Saccadic Landing Positions for S-Cone-Isolating Targets. Journal of Vision, 23(15), 74.

Wang, Y., Vu, B. T., Wang, C., Ng, R., & Tuten, W. S. (2023). Preferred Retinal Locus of Fixation in the S-cone Pathway. Investigative Ophthalmology & Visual Science, 64(8), 468.

4 Chapter 4 | Human S-cone Topography and Function

4.1 Abstract

The human fovea is a highly specialized retinal region characterized by densely packed photoreceptors, laterally displaced post-receptoral neurons, and an absence of short-wavelength-sensitive receptors in the central ~20 arcmin. High-resolution retinal imaging systems have enabled cellular-scale assessments of foveal structure and function, revealing significant variation in peak cone density and foveal pit morphology within the normal population. In this study, we used an adaptive optics platform to examine whether individual differences extend to the spatial properties of the foveolar S-cone scotoma.

We assessed S-cone-mediated sensitivity across the central fovea of six color-normal subjects (same subjects from Chapter 3) using a two-color increment threshold paradigm. Square flashes (λ = 460±10 nm; diameter = 10 arcmin; duration = 200 ms) were delivered to targeted retinal locations via a multi-wavelength adaptive optics scanning laser ophthalmoscope (AOSLO). These test increments were superimposed on a bright yellow background (CIEx,y = [0.545, 0.451]) from an external projector. Threshold-versus-intensity curves in a subset of subjects confirmed S-cone isolation. Retinal-stabilized stimuli were presented in a pseudorandom order to a 5x5 grid of retinal targets, mapping short-wavelength sensitivity over the central 50x50 arcmin area. An adaptive staircase guided by the QUEST algorithm estimated detection thresholds at each location. Transverse chromatic aberration between test and imaging wavelengths was psychophysically corrected to align the sensitivity map with the high-resolution retinal image.

We compared individual short-wavelength sensitivity patterns to measurements of the preferred retinal locus of fixation (PRL) under S-cone isolating conditions from an earlier study (Wang, Vu, et al., 2023; Wang, Wang, et al., 2023). Macular pigments were imaged using dual-wavelength measurements guided by AOSLO visible light imaging, employing interleaved low-power imaging with 840-nm light at odd pixel lines and visible light (543-nm or 488-nm) at even pixel lines. This paradigm allowed tracking in the 840-nm channel and imaging in the green or blue channel, with defocus and intensity optimized using a per-pixel rolling average of stabilized frames.

All subjects showed a central region with reduced sensitivity to short-wavelength stimuli. The number of scotomatous loci (areas unable to detect the highest stimulus intensity) varied among subjects and correlated with the distance between their S- and L/M-cone PRLs. Specifically, greater displacement between the S-cone and L/M-cone PRLs was associated with larger S-cone scotomas. Additionally, macular pigment optical density analysis revealed a central region with dense macular pigments. However, the peak location of these pigments did not always align with the S-cone scotoma regions.

Our findings reveal individual differences in foveal sensitivity to short-wavelength light, suggesting variability in S-cone distribution patterns among subjects. High-resolution short-wavelength imaging to map macular pigment optical density (MPOD) indicates that

macular pigment distribution does not always correlate with retinal sensitivity to blue light. These techniques collectively enhance our understanding of how preretinal filtering and S-cone topography affect foveal vision.

4.2 Introduction

S-cones, a type of cone photoreceptor sensitive to short-wavelength light, constitute 5-10% of the retina, exhibiting the lowest cell density at the fovea compared to parafoveal regions (Calkins, 2001; Curcio et al., 1991). Studies have revealed variations in the distribution of S-cones at the foveal center, with histology studies suggesting a small S-cone-free zone of about 0.35° (Curcio et al., 1991), while others indicate a decrease in S-cone density without complete absence at the foveola (Ahnelt, 1998). This individual variability was observed in early psychophysical studies as well, with reports of foveal tritanopic areas ranging from 8 to 25 arcmin (Wald, 1967; Williams et al., 1981b; Willmer, 1944; Willmer & Wright, 1945). Additional techniques such as retinal densitometry and optoretinogram-based cone classification have been employed to classify cone photoreceptor types, yet they have limitations in resolving the spectral profiles of foveal cones within the central 0.5° (Pandiyan et al., 2020; Roorda & Williams, 1999; Sabesan et al., 2015; Zhang et al., 2019).

Previous psychophysical studies using short-duration, small-spot stimuli have outlined a central region of reduced sensitivity to blue stimulus, indicating a potential foveal S-cone-free zone (Williams et al., 1981a). Our study aims to further investigate individual variability in S-cone topography by mapping the foveal S-cone distribution using adaptive optics microperimetry (AOMP) with real-time eye tracking. To address pre-receptoral blue filtering effects by macular pigments, we have developed imaging tools to quantify the distribution of macular pigment optical density in our subject cohort.

Macular pigments, carotenoids present in photoreceptor axons, exhibit blue filtering properties, absorbing light within the range of 400-520 nm with peak absorbance at 460 nm (Whitehead et al., 2006). This absorption is most pronounced at the fovea and diminishes beyond 3° retinal eccentricity, with differences in retinal reflectance between green and blue light serving as a measure of blue light absorption by macular pigments (Lima et al., 2016; Nolan et al., 2008).

4.3 Methods

4.3.1 Adaptive Optics Microperimetry

We conducted high-resolution retinal imaging of the outer retinal structure in and around the fovea using an adaptive optics scanning laser ophthalmoscope (AOSLO) equipped with a confocal detector configuration. This system allowed us to achieve high-resolution imaging of the cone photoreceptor mosaic by measuring and optically correcting for blurcausing aberrations in the eye. We utilized 840-nm light to record a series of 1.7° x 1.7° videos of the macula.

Assessment of the preferred retinal locus (PRL) was carried out by recording an AOSLO video with 840-nm light while the patient fixated on a small, blinking decrement-spot delivered via the same AOSLO raster scan. The mean PRL and fixation stability were determined based on the retinal locations where the stimulus landed during fixation over the course of the video. Subsequently, using the retinal video recorded during the PRL measurement, we generated a stabilized retinal map as a reference frame for retinal tracking. The estimated foveal center was manually selected at a location close to the PRL, characterized by the smallest foveal cones and a darker region on the retinal map. A 5 x 5 test grid with 10-arcmin spacing was then centered on the selected foveal center for the subsequent microperimetry procedure (Figure 4.1A).

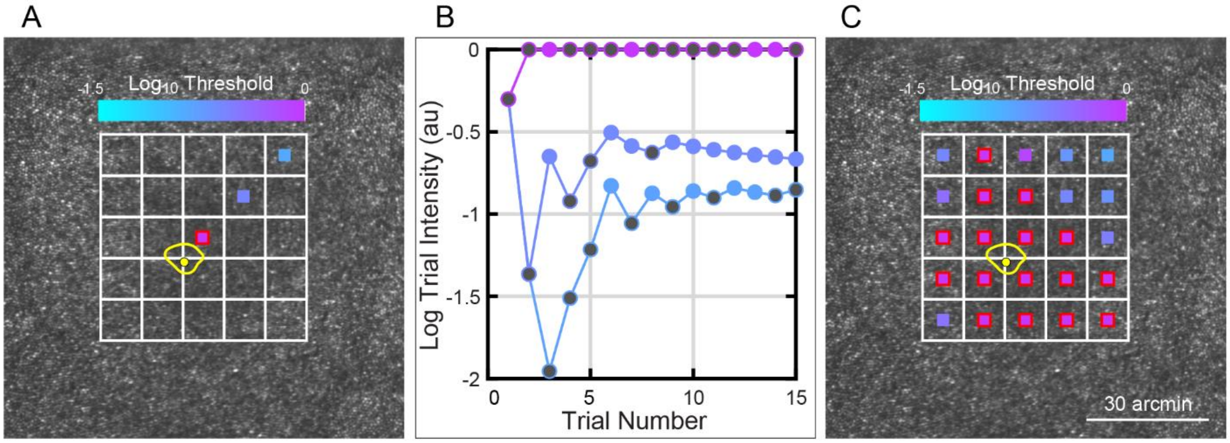

Figure 4.1 Adaptive Optics Microperimetry Experiment in One Normal Subject

(A) The preferred retinal locus (PRL) was measured at the fovea, shown as a yellow dot with a contour compassing 68% of fixation distribution. The location of the foveola was manually chosen near the PRL location based on the foveal cone appearance. The 5 x 5 test grid was centered on the selected foveolar location. The blue stimulus, with a 200-ms duration, was delivered to interleaved spatial locations. The intensity of the blue stimulus was guided by a QUEST staircase algorithm and controlled linearly, with possible values spanning 3 log units from 0.1% to 100% intensity. The color of each location indicates sensitivity to the blue stimulus, with bluer areas representing higher sensitivity. The purple box with a red outline indicates an area with unmeasurable threshold. Threshold results from 3 test locations are shown. (B) The QUEST-guided staircases for the 3 test locations corresponding to those in (A) are shown. Test spots in solid grey indicate a response of "not seen". Differences in detection thresholds among the 3 spatial locations are visualized. (C) The detection threshold for all 25 test locations was determined using a psychometric function set to 75% visibility. Among the 25 locations, 16 areas show an unmeasurable threshold, outlined by a red box within these regions.

We employed AO-based microperimetry (AOMP) with real-time eye tracking to examine the retinal sensitivity of the central 50 x 50 arcminutes area using retinally stabilized increment stimuli (Tuten et al., 2012). This procedure was conducted on the same AOSLO platform used for retinal imaging and tracking, employing 840-nm light for retinal imaging and tracking, while a 10-arcmin blue stimulus (460-nm, created from a second laser source, SuperK Fianium FIU-15 with VARIA tunable filter, NKT Photonics, Denmark) was presented at targeted locations via the same raster scan. Retinal sensitivity at each location was measured using a yes-no Quest adaptive staircase procedure with 15 trials per location (Watson & Pelli, 1983). An example of the staircases from 3 locations is shown in Figure 4.1B. One-second AOSLO videos were recorded during each AOMP trial to precisely determine the stimulus position on the retina and assess tracking fidelity.

S-cone isolation was achieved similarly to the chromatic adaptation method described in Chapter 2. We utilized an external projector to create a yellow background (CIEx,y = [0.545, 0.451], 2024 cd/m^2). Transverse chromatic aberration (TCA) between 840-nm and 460-nm was psychophysically adjusted by overlaying a blue square from the 460-nm channel with a black decrement square from the 840-nm channel, and this TCA correction was applied to the stimulus location during the experiment (Harmening et al., 2012) .

At the conclusion of the experiment, the staircase results with estimated thresholds were evaluated by the examiner. If the highest threshold spot fell on the edge of the 5 x 5 test grid, another block of experiments with a 3x3 grid centered on the previously measured highest threshold spot was performed.

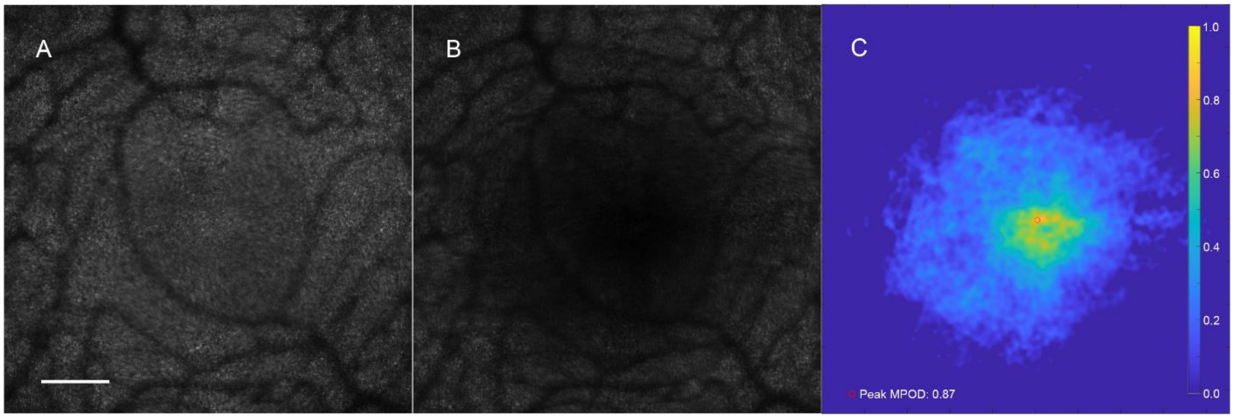

Figure 4.2 Macular Pigment Imaging and Analysis of One Normal Subject

Foveal maps imaged with 543 nm (A) and 488 nm (B) are presented in the figure. Both maps were seamlessly analyzed using R-SLAM and overlaid using the cross-correlation function in MATLAB. The macular pigment optical density (MPOD) map (C) displays the distribution of macular pigment at the macula, with a peak MPOD value of 0.87 in this subject. All 3 subfigures have the same image scale with the 30-arcminute scale bar. Imaging data are from the same subject in Figure 4.1.

4.3.2 Macular Pigment Imaging

Macular pigments of six subjects were imaged using dual-wavelength measurements guided by AOSLO visible light imaging at a separate session. We employed interleaved low-power imaging with 840-nm at every odd pixel line and visible light (543-nm or 488-

nm) at every even pixel line, enabling tracking in the 840-nm channel and imaging in the green or blue channel. The 488-nm light source was provided by a SuperK Fianium FIU-15 with a VARIA tunable filter, as described in a previous section. The defocus and intensity of the visible light imaging channel were optimized using a per-pixel rolling average of the last few stabilized frames.

We recorded one 3-second video at 4° eccentricity and nine 3-second videos at and around the fovea using 543-nm and 488-nm imaging lights separately. Additionally, background videos at each retinal location with both imaging lights were recorded to establish a baseline intensity level for each imaging condition. Throughout the imaging process, a red fixation dot was employed to guide the subject's gaze during imaging.

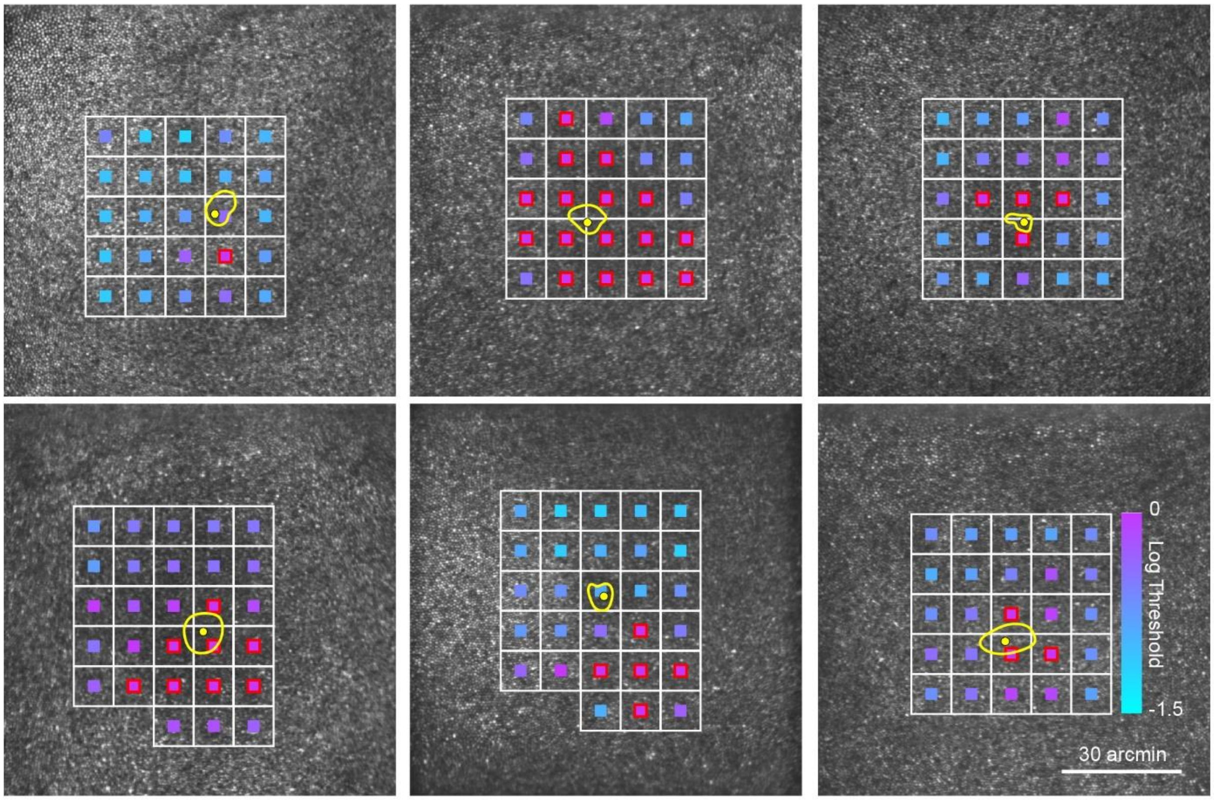

Figure 4.3 Adaptive Optics Microperimetry Results from All Normal Subjects

Each white box shows 10-arcmin stimulus size within the 5 x 5 stimulus grid. The colored square inside each test location indicates the threshold to blue stimulus for this retinal location. The areas with unmeasurable sensitivity (functional scotoma) are shown in bright purple and labeled with a red outline. As shown in Figure 4.1, the yellow dot surrounded by a contour represents the PRL location and 68% ISOA contour.

4.3.3 Data Analysis

The stimulus intensities and subject responses obtained from the QUEST-guided staircase for each location were utilized to determine the detection threshold. A psychometric function was fitted to identify the 75% visibility threshold utilizing the Palamedes toolbox (Prins & Kingdom, 2018). Subsequently, the AOMP results were superimposed onto the corresponding retinal images using Adobe Illustrator (Figure 4.1C).

In areas of the retina where subjects consistently reported "not seen" even with the highest stimulus intensity that was delivered, the threshold was not measurable within the test intensity range. Such areas were defined as S-cone scotomas. The number of S-cone scotomas was recorded from the S-cone sensitivity map. The displacement of the subject's corresponding S-cone preferred retinal locus (PRL) from Chapter 3 and the radius of scotoma areas were analyzed using the Pearson correlation function in MATLAB.

To obtain the macular pigment distributions, seamless retinal maps of both the infrared (IR) and blue channels at all tested retinal eccentricities were generated separately using R-SLAM to de-interleave the signals, as described in Chapter 3. The mean pixel value of the background videos was subtracted to generate radiometrically accurate retinal intensity maps.

Furthermore, the mean intensity ratio between the green and blue channels at 4-degree eccentricity was computed and applied to the foveal maps to offset any difference in image intensity between the green and blue channels (Equation 1). The foveal maps of the green and blue channels were cropped and overlaid at the exact same location and then blurred with a Gaussian filter with a standard deviation of 5 pixels. Blurring images with filters, such as a Gaussian filter, is necessary to reduce high-frequency noise, smooth the image, and improve alignment accuracy when overlaying images from different channels.

The ratio between the blurred green and blue foveal maps was converted to the logarithmic scale to compute the macular pigment optical density (Equation 2).

$$\mathrm{K} = \frac{\text{Mean Luminance}_{543\text{nm}} - \text{Background Luminance}_{543\text{nm}}}{\text{Mean Luminance}_{488\text{nm}} - \text{Background Luminance}_{488\text{nm}}}$$

Equation 1. Luminance Ratio between two imaging channels. Background luminance was adjusted.

$$\text{Macular Pigmental Optical Density} = log10\left(\frac{1}{2} * \frac{\text{Foveal Map}_{543\text{nm}}}{\text{K * Foveal Map}_{488\text{nm}}} \right)$$

Equation 2. Calculation of macular pigment optical density.

4.4 **Results**

Figure 4.3 illustrates the S-cone sensitivity findings for all six normal subjects overlaid onto their respective retinal maps. The grid of 5 x 5 with 10-arcminutes spacing delineates stimulus locations, where detection thresholds for blue stimuli are depicted using a color scale. Blue light intensity spans from 0.1% to 100%, represented logarithmically from -3 to 0. Five out of six subjects had the same highest intensity of 0.008 µW. However, Subject 10003L was unable to see the highest laser intensity, so the upper power range was adjusted to 0.025 µW for this subject. It's important to note that the sensitivity map of Subject 10003L was not calibrated to the same highest laser power as other subjects. Due to numerous locations with unmeasurable thresholds in this subject, adjusting the measurable thresholds retrospectively does not alter the finding of 16 out of 25 scotomatous areas (Figure 4.1A).

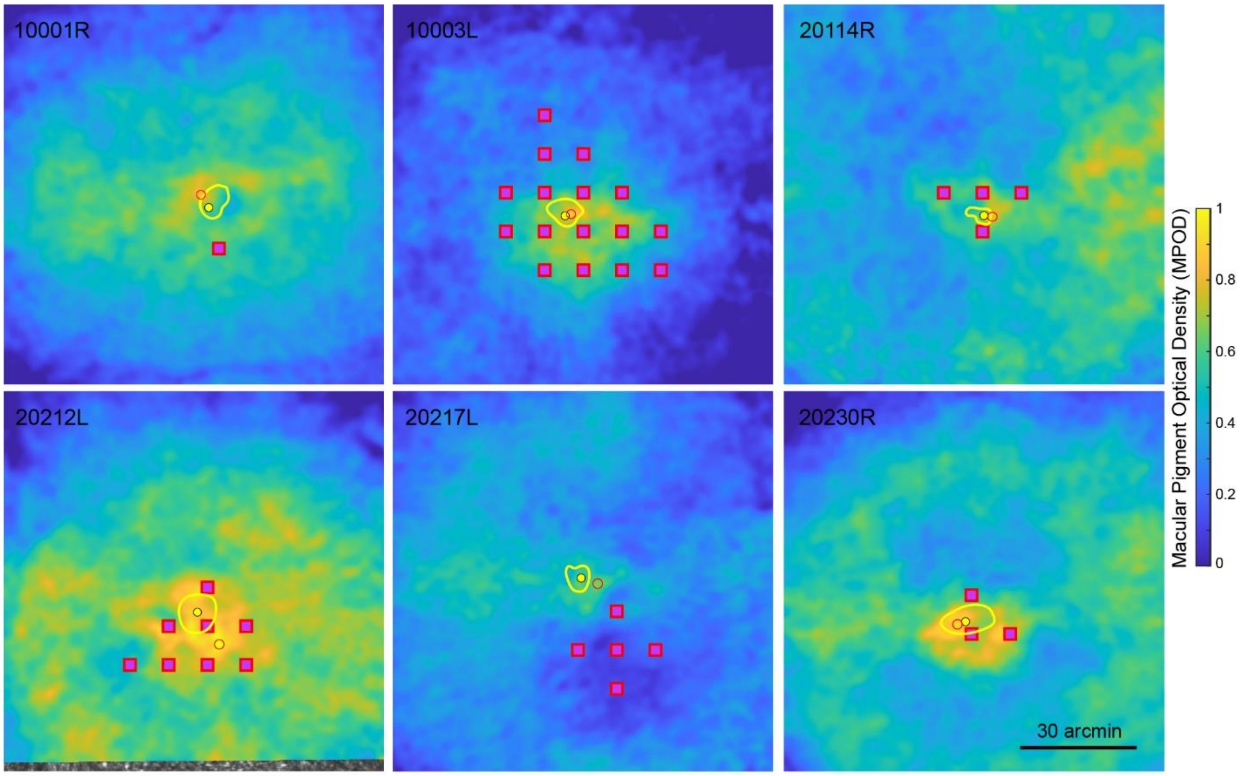

Figure 4.4 Macular Pigment Optical Density Maps

The S-cone scotomas are shown in purple squares with the red outline and the PRL was labeled as a yellow dot, same presentation as Figure 4.3. The color map is the macular pigment optical density map for each individual subject with warmer color showing higher optical density. The peak optical density is labeled the red circle. The relative distances between the PRL, S-cone scotoma and peak MPOD were visualized.

Threshold values for all subjects are plotted on a shared scale from -1.5 to 0, corresponding to intensities from 3.2% to 100%. Lower log thresholds indicate heightened sensitivity to blue stimuli, depicted by a more pronounced blue color; conversely, decreased sensitivity appears as a deeper purple on the color scale. Regions with unmeasurable thresholds are highlighted in bright purple with a distinct red outline, indicating instances where the subject consistently reported "not seen" when the stimulus was presented at 100% intensity. Across all subjects, a central region of diminished sensitivity to short-wavelength stimuli is evident, while parafoveal regions exhibit varying sensitivity to blue light. Among the six subjects, the number of S-cone scotomatous areas ranged from 1 to 16. These scotomatous areas correspond to diameters approximately ranging from 10 to 40 arcminutes. The preferred retinal locus (PRL) measured with decrement in the 840-nm laser channel is denoted by a yellow dot on the retinal map, illustrating its relative distance from the S-cone-free zone area. While the PRL locations in all subjects tend to be near the S-cone scotomatous areas, these two landmarks do not align perfectly.

Macular pigment optical density (MPOD) maps were generated for each subject, with peak MPOD values indicated by a red circle, ranging from approximately 0.6 to 1.0 optical density units. An example of the MPOD imaging and analysis is depicted in Figure 4.2. The overlay of S-cone sensitivity maps and macular pigment distribution maps revealed that the L/M-cone PRL aligns with the peak MPOD, but the S-cone-free zone (S-cone scotoma) does not always correspond to areas of dense macular pigment distribution (Figure 4.4).

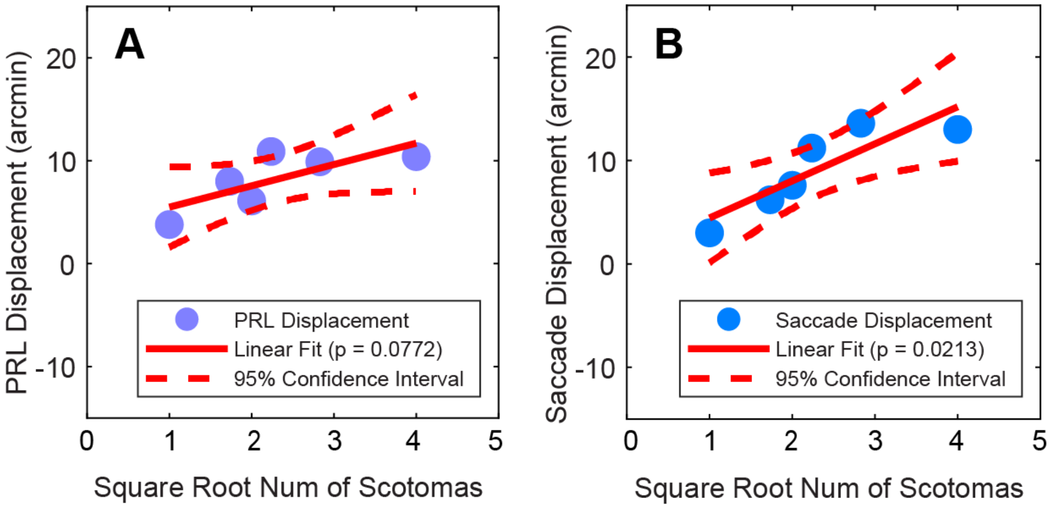

Figure 4.5 Relationship between Radius of Scotomatous Areas and Fixation Displacement

The X-axis represents the square root of the scotoma numbers, which better reflects the radius of the scotomatous areas. (A) The mean PRL displacement of six normal subjects and their AOMP results were analyzed using linear regression. Subjects with larger S-cone scotoma areas tend to have greater S-cone PRL displacement, although this statistical correlation was not significant. (B) The mean displacement of saccade landing endpoints was correlated with the number of S-cone scotomas. This linear correlation shows statistical significance.

The sPRL location and its displacement from the L/M-cone PRL measured in Chapter 3 were not plotted in Figure 4.4 due to the difference in test stimuli used in the two experiments: an externally aligned projector in Chapter 3 versus a co-aligned tunable laser in Chapter 4. Additionally, the stimulus sizes and optical quality differed significantly between the experiments. The Chapter 3's experiment used a threshold letter size for S-cone acuity, approximately 50 arcmin, adjusted with spherical and cylindrical correction, whereas the S-cone AOMP experiment in Chapter 4 used a 10-arcmin blue square stimulus with adaptive optics and transverse chromatic aberration (TCA) correction.

Quantitative analysis of S-cone-mediated PRL and saccade landing endpoint displacements as a function of the radius of the S-cone scotoma is shown in Figure 4.5. Subjects with larger S-cone scotoma areas tend to have greater S-cone PRL displacement, although this correlation was not statistically significant (Pearson correlation, $R^2 = 0.583$, $p = 0.0772$). However, the mean displacement of saccade landing endpoints was significantly correlated with the number of S-cone scotomas (Pearson correlation, $R^2 = 0.772$, $p = 0.0213$).

4.5 Discussion

This study is the first to functionally map the S-cone-free zone in normal subjects using adaptive optics-corrected and retinal-tracked microperimetry. Our results revealed that all normal subjects exhibited a central region of reduced sensitivity to short-wavelength stimuli. The areas of unmeasurable blue sensitivity varied among individuals, ranging from 1 to 16 out of 25 test locations. This corresponds to S-cone scotomatous areas with diameters approximately ranging from 10 to 40 arcmin. Subjects with larger S-cone PRL displacement, as shown in Chapter 3, tended to have bigger S-cone scotomas. These findings are consistent with limited existing histology reports that demonstrate variable foveal S-cone topography (Ahnelt, 1998; Curcio et al., 1991).

Our sample size consisted of 6 normal subjects with data on S-cone acuity, S-cone PRL displacement, and S-cone scotomas. The statistical analysis is limited by this small sample size. Although the correlation between S-cone PRL displacement of one visit and S-cone acuity is statistically significant, S-cone-mediated acuity is more related to the sampling limit of small bistratified ganglion cells rather than foveal S-cone topography. The correlation between S-cone PRL displacement and the radius of the S-cone scotoma is also constrained by the small sample size.

The estimation of S-cone scotomas has limitations, including the coarse scale of a 10-arcmin stimulus size, in contrast to previously reported psychophysical data, which used a 1.1-arcmin stimulus size (Williams et al., 1981a). Additionally, our stimulus duration of 200 ms is longer than the 50 ms used by Williams et al. While the shorter duration controlled for errors caused by fixational eye movements, our experimental paradigm incorporates real-time retinal tracking to correct for eye movement-related factors. Since S-cones are known to have slower kinetics than L/M-cones (Baudin et al., 2019), allowing a longer blue stimulation duration helps rule out the possibility that S-cone kinetics caused invisibility.

Due to the length of each experimental session, each participant could only complete one staircase of 15 trials per retinal location (25 locations in total). Using the S-cone isolation method with a bright yellow background and ensuring accurate stimulus delivery with real-time retinal tracking, each session lasted about 2 hours.

Our microperimetry results were not corrected for macular pigment optical density (MPOD) due to the coarse scale of the stimulus grid and the test stimulus intensity range, which led to unmeasurable thresholds in the foveal region. The test stimulus was set at 100% maximum intensity yet subjects still could not perceive the blue light at certain locations, making the stimulus staircase unadjustable by MPOD, leading to uncorrectable intensities. We overlaid the macular pigment optical density map with the S-cone sensitivity map and found that the locations of peak macular pigment optical density did not always overlap with areas of S-cone scotomas. Thus, the heterogeneity of functional scotomas to blue light cannot be solely explained by macular pigment distribution.

Future steps include repeating the sensitivity measurements at the same retinal locations and adding more trials per location, as the existing dataset consists of only 15 trials per location. Additionally, measuring S-cone sensitivity as a function of background luminance for each subject is necessary to validate S-cone isolation and optimize the stimulus intensity range. Ultimately, the S-cone sensitivity map should be corrected for MPOD to provide a true mapping of S-cone topography.

4.6 Conclusion

In conclusion, this study represents a pioneering effort to functionally map the S-cone-free zone in normal subjects using AOSLO microperimetry. Our findings demonstrate a central region of reduced sensitivity to short-wavelength stimuli in all normal subjects, with variable areas of unmeasurable blue sensitivity. The observed correlation between larger S-cone PRL displacement and larger S-cone scotomas, despite the small sample size, provides valuable insights into the relationship between S-cone PRL displacement and S-cone-free zone size. Limitations, such as the coarse stimulus scale and lack of MPOD correction, highlight the need for refined methodologies. Future research should aim to increase the number of trials per retinal location and incorporate MPOD corrections to achieve a more accurate mapping of S-cone topography. This study lays the groundwork for deeper understanding and more precise measurement techniques in the assessment of S-cone foveal topography.

5 References

Agaoglu, M. N., Fung, W., & Chung, S. T. L. (2022). Oculomotor responses of the visual system to an artificial central scotoma may not represent genuine visuomotor adaptation. *Journal of Vision*, *22*(10). https://doi.org/10.1167/jov.22.10.17

Ahnelt, P. K. (1998). The photoreceptor mosaic. *Eye (Basingstoke)*, *12*(3), 531–540. https://doi.org/10.1038/eye.1998.142

Ahnelt, P. K., Kolb, H., & Pflug, R. (1987). Identification of a subtype of cone photoreceptor, likely to be blue sensitive, in the human retina. *Journal of Comparative Neurology*, *255*(1). https://doi.org/10.1002/cne.902550103

Ammar, M. J., Scavelli, K. T., Uyhazi, K. E., Bedoukian, E. C., Serrano, L. W., Edelstein, I. D., Vergilio, G., Cooper, R. F., Morgan, J. I. W., Kumar, P., & Aleman, T. S. (2021). ENHANCED S-CONE SYNDROME: VISUAL FUNCTION, CROSS-SECTIONAL IMAGING, AND CELLULAR STRUCTURE WITH ADAPTIVE OPTICS OPHTHALMOSCOPY. *Retinal Cases and Brief Reports*, *15*(6). https://journals.lww.com/retinalcases/Fulltext/2021/11000/ENHANCED_S_CONE_SYNDROME__VISUAL_FUNCTION,.11.aspx

Anderson, Mullen, K. T., & Hess, R. F. (1991). Human peripheral spatial resolution for achromatic and chromatic stimuli: limits imposed by optical and retinal factors. *The Journal of Physiology*, *442*(1), 47–64. https://doi.org/10.1113/jphysiol.1991.sp018781

Anderson, R. S., Wilkinson, M. O., & Thibos, L. N. (1992). Psychophysical Localization of the Human Visual Streak. *Optom Vis Sci*, *69*(3), 171–174. https://doi.org/10.1097/00006324-199203000-00001

Anderson, Zlatkova, M. B., & Demirel, S. (2002). What limits detection and resolution of short-wavelength sinusoidal gratings across the retina? *Vision Res*, *42*(8), 981–990. https://doi.org/10.1016/s0042-6989(02)00013-5

Audo, I., Michaelides, M., Robson, A. G., Hawlina, M., Vaclavik, V., Sandbach, J. M., Neveu, M. M., Hogg, C. R., Hunt, D. M., Moore, A. T., Bird, A. C., Webster, A. R., & Holder, G. E. (2008). Phenotypic variation in enhanced S-cone syndrome. *Invest Ophthalmol Vis Sci*, *49*(5), 2082–2093. https://doi.org/10.1167/iovs.05-1629

Barash, S., Melikyan, A., Sivakov, A., & Tauber, M. (1998). Shift of visual fixation dependent on background illumination. *Journal of Neurophysiology*, *79*(5). https://doi.org/10.1152/jn.1998.79.5.2766

Baudin, J., Angueyra, J. M., Sinha, R., & Rieke, F. (2019). S-cone photoreceptors in the primate retina are functionally distinct from L and M cones. *Elife*, *8*. https://doi.org/10.7554/elife.39166

Bedggood, P., Daaboul, M., Ashman, R., Smith, G., & Metha, A. (2008). Characteristics of the human isoplanatic patch and implications for adaptive optics retinal imaging. *Journal of Biomedical Optics*, *13*(2). https://doi.org/10.1117/1.2907211

Bompas, A., & Sumner, P. (2009). Oculomotor distraction by signals invisible to the retinotectal and magnocellular pathways. *Journal of Neurophysiology*, *102*(4). https://doi.org/10.1152/jn.00359.2009

Bowers, N. R., Gautier, J., Lin, S., & Roorda, A. (2021). Fixational eye movements in passive versus active sustained fixation tasks. *Journal of Vision*, *21*(11), 16. https://doi.org/10.1167/jov.21.11.16

Bowmaker, J. K., & Dartnall, H. J. (1980). Visual pigments of rods and cones in a human retina. *The Journal of Physiology*, *298*(1). https://doi.org/10.1113/jphysiol.1980.sp013097

Brainard, D. H. (1997). The Psychophysics Toolbox. *Spat Vis*, *10*(4), 433–436. https://www.ncbi.nlm.nih.gov/pubmed/9176952

Bringmann, A., Syrbe, S., Görner, K., Kacza, J., Francke, M., Wiedemann, P., & Reichenbach, A. (2018). The primate fovea: Structure, function and development. *Progress in Retinal and Eye Research*, *66*, 49–84. https://doi.org/https://doi.org/10.1016/j.preteyeres.2018.03.006

Bush, R. A., Tanikawa, A., Zeng, Y., & Sieving, P. A. (2019). Cone ERG Changes During Light Adaptation in Two All-Cone Mutant Mice: Implications for Rod-Cone Pathway Interactions. *Investigative Opthalmology & Visual Science*, *60*(10), 3680. https://doi.org/10.1167/iovs.19-27242

Calkins, D. J. (2001). Seeing with S cones. In *Progress in Retinal and Eye Research* (Vol. 20, Issue 3). https://doi.org/10.1016/S1350-9462(00)00026-4

Castet, E., & Crossland, M. (2012). Quantifying eye stability during a fixation task: A review of definitions and methods. *Seeing and Perceiving*, *25*(5). https://doi.org/10.1163/187847611X620955

Chen, M., Cooper, R. F., Han, G. K., Gee, J., Brainard, D. H., & Morgan, J. I. (2016). Multi-modal automatic montaging of adaptive optics retinal images. *Biomed Opt Express*, *7*(12), 4899–4918. https://doi.org/10.1364/boe.7.004899

Coates, D. R., & Chung, S. T. L. (2016). Crowding in the S-cone pathway. *Vision Res*, *122*, 81–92. https://doi.org/10.1016/j.visres.2016.03.007

Cole, B. L. (2007). Assessment of inherited colour vision defects in clinical practice. In *Clinical and Experimental Optometry* (Vol. 90, Issue 3). https://doi.org/10.1111/j.1444-0938.2007.00135.x

Cooper, R. F., Wilk, M. A., Tarima, S., & Carroll, J. (2016). Evaluating Descriptive Metrics of the Human Cone Mosaic. *Investigative Opthalmology & Visual Science*, *57*(7), 2992. https://doi.org/10.1167/iovs.16-19072

Coppieters, F., Leroy, B. P., Beysen, D., Hellemans, J., De Bosscher, K., Haegeman, G., Robberecht, K., Wuyts, W., Coucke, P. J., & De Baere, E. (2007). Recurrent mutation in the first zinc finger of the orphan nuclear receptor NR2E3 causes autosomal dominant retinitis pigmentosa. *Am J Hum Genet*, *81*(1), 147–157. https://doi.org/10.1086/518426

Corbo, J. C., & Cepko, C. L. (2005). A Hybrid Photoreceptor Expressing Both Rod and Cone Genes in a Mouse Model of Enhanced S-Cone Syndrome. *PLoS Genet*, *1*(2), e11. https://doi.org/10.1371/journal.pgen.0010011

Crossland, M. D., Culham, L. E., Kabanarou, S. A., & Rubin, G. S. (2005a). Preferred Retinal Locus Development in Patients with Macular Disease. *Ophthalmology*, *112*(9), 1579–1585. https://doi.org/https://doi.org/10.1016/j.ophtha.2005.03.027

Crossland, M. D., Culham, L. E., Kabanarou, S. A., & Rubin, G. S. (2005b). Preferred retinal locus development in patients with macular disease. *Ophthalmology*, *112*(9). https://doi.org/10.1016/j.ophtha.2005.03.027

Curcio, C. A., & Allen, K. A. (1990). Topography of ganglion cells in human retina. *Journal of Comparative Neurology*, *300*(1). https://doi.org/10.1002/cne.903000103

Curcio, C. A., Allen, K. A., Sloan, K. R., Lerea, C. L., Hurley, J. B., Klock, I. B., & Milam, A. H. (1991). Distribution and morphology of human cone photoreceptors stained with anti-blue opsin. *J Comp Neurol*, *312*(4), 610–624. https://doi.org/10.1002/cne.903120411

Curcio, C. A., Sloan, K. R., Kalina, R. E., & Hendrickson, A. E. (1990). Human photoreceptor topography. *J Comp Neurol*, *292*(4), 497–523. https://doi.org/10.1002/cne.902920402

Dacey, D. M. (1993a). Morphology of a small-field bistratified ganglion cell type in the macaque and human retina. *Vis Neurosci*, *10*(6), 1081–1098. https://doi.org/10.1017/s0952523800010191

Dacey, D. M. (1993b). The mosaic of midget ganglion cells in the human retina. *J Neurosci*, *13*(12), 5334–5355. https://doi.org/10.1523/jneurosci.13-12-05334.1993

Dacey, D. M., & Lee, B. B. (1994). The “blue-on” opponent pathway in primate retina originates from a distinct bistratified ganglion cell type. *Nature*, *367*(6465), 731–735. https://doi.org/10.1038/367731a0

de Carvalho, E. R., Robson, A. G., Arno, G., Boon, C. J. F., Webster, A. A., & Michaelides, M. (2021). Enhanced S-Cone Syndrome: Spectrum of Clinical, Imaging, Electrophysiologic, and Genetic Findings in a Retrospective Case Series of 56 Patients. *Ophthalmol Retina*, *5*(2), 195–214. https://doi.org/10.1016/j.oret.2020.07.008

De Monasterio, F. M. (1978). Properties of ganglion cells with atypical receptive-field organization in retina of Macaques. *Journal of Neurophysiology*, *41*(6). https://doi.org/10.1152/jn.1978.41.6.1435

Dorris, M. C., Paré, M., & Munoz, D. P. (1997). Neuronal activity in monkey superior colliculus related to the initiation of saccadic eye movements. *Journal of Neuroscience*, *17*(21). https://doi.org/10.1523/jneurosci.17-21-08566.1997

Duncan, J. L., Liang, W., Maguire, M. G., Porco, T. C., Wong, J., Audo, I., Cava, J. A., Grieve, K., Kalitzeos, A., Kreis, J., Michaelides, M., Norberg, N., Paques, M., & Carroll, J. (2023). Change in cone structure over 24 months in USH2A-related retinal degeneration. *American Journal of Ophthalmology*. https://doi.org/https://doi.org/10.1016/j.ajo.2023.03.006

Duncan, J. L., Zhang, Y., Gandhi, J., Nakanishi, C., Othman, M., Branham, K. E., Swaroop, A., & Roorda, A. (2007). High-resolution imaging with adaptive optics in patients with inherited retinal degeneration. *Invest Ophthalmol Vis Sci*, *48*(7), 3283–3291. https://doi.org/10.1167/iovs.06-1422

Dunn, F. A., DellaSantina, L., Parker, E. D., & Wong, R. O. L. (2013). Sensory experience shapes the development of the visual system's first synapse. *Neuron*, *80*(5). https://doi.org/10.1016/j.neuron.2013.09.024

Ferris, F. L., Kassoff, A., Bresnick, G. H., & Bailey, I. (1982). New visual acuity charts for clinical research. *American Journal of Ophthalmology*, *94*(1). https://doi.org/10.1016/0002-9394(82)90197-0

Field, G. D., Gauthier, J. L., Sher, A., Greschner, M., Machado, T. A., Jepson, L. H., Shlens, J., Gunning, D. E., Mathieson, K., Dabrowski, W., Paninski, L., Litke, A. M., & Chichilnisky, E. J. (2010). Functional connectivity in the retina at the resolution of photoreceptors. *Nature*, *467*(7316), 673–677. https://doi.org/10.1038/nature09424

Foote, K. G., Loumou, P., Griffin, S., Qin, J., Ratnam, K., Porco, T. C., Roorda, A., & Duncan, J. L. (2018). Relationship Between Foveal Cone Structure and Visual Acuity Measured With Adaptive Optics Scanning Laser Ophthalmoscopy in Retinal Degeneration. *Investigative Opthalmology & Visual Science*, *59*(8), 3385. https://doi.org/10.1167/iovs.17-23708

Garafalo, A. V, Calzetti, G., Cideciyan, A. V, Roman, A. J., Saxena, S., Sumaroka, A., Choi, W., Wright, A. F., & Jacobson, S. G. (2018). Cone Vision Changes in the Enhanced S-Cone Syndrome Caused by NR2E3 Gene Mutations. *Investigative Ophthalmology & Visual Science*, *59*(8), 3209–3219. https://doi.org/10.1167/iovs.18-24518

Greenstein, V. C., Santos, R. A. V., Tsang, S. H., Smith, R. T., Barile, G. R., & Seiple, W. (2008). Preferred retinal locus in macular disease characteristics and clinical implications. *Retina*, *28*(9). https://doi.org/10.1097/IAE.0b013e31817c1b47

Greenstein, V. C., Zaidi, Q., Hood, D. C., Spehar, B., Cideciyan, A. V, & Jacobson, S. G. (1996). The enhanced S cone syndrome: an analysis of receptoral and post-receptoral changes. *Vision Res*, *36*(22), 3711–3722. https://doi.org/10.1016/0042-6989(96)00073-9

Haider, N. B., Demarco, P., Nystuen, A. M., Huang, X., Smith, R. S., McCall, M. A., Naggert, J. K., & Nishina, P. M. (2006). The transcription factor Nr2e3 functions in retinal progenitors to suppress cone cell generation. *Vis Neurosci*, *23*(6), 917–929. https://doi.org/10.1017/s095252380623027x

Harmening, W. M., Tiruveedhula, P., Roorda, A., & Sincich, L. C. (2012). Measurement and correction of transverse chromatic offsets for multi-wavelength retinal microscopy in the living eye. *Biomed Opt Express*, *3*(9), 2066–2077. https://doi.org/10.1364/boe.3.002066

Hendrickson, A., Bumsted-O'Brien, K., Natoli, R., Ramamurthy, V., Possin, D., & Provis, J. (2008). Rod photoreceptor differentiation in fetal and infant human retina. *Experimental Eye Research*, *87*(5). https://doi.org/10.1016/j.exer.2008.07.016

Hood, D. C., Cideciyan, A. V, Roman, A. J., & Jacobson, S. G. (1995). Enhanced S cone syndrome: evidence for an abnormally large number of S cones. *Vision Res*, *35*(10), 1473–1481. https://doi.org/10.1016/0042-6989(95)98727-q

Humanski, R. A., & Wilson, H. R. (1992). Spatial frequency mechanisms with short-wavelength-sensitive cone inputs. *Vision Research*, *32*(3). https://doi.org/10.1016/0042-6989(92)90247-G

Jacobson, S. G., Marmor, M. F., Kemp, C. M., & Knighton, R. W. (1990). SWS (blue) cone hypersensitivity in a newly identified retinal degeneration. *Invest Ophthalmol Vis Sci*, *31*(5), 827–838. https://www.ncbi.nlm.nih.gov/pubmed/2335450

Jacobson, S. G., Sumaroka, A., Aleman, T. S., Cideciyan, A. V, Schwartz, S. B., Roman, A. J., McInnes, R. R., Sheffield, V. C., Stone, E. M., Swaroop, A., & Wright, A. F. (2004). Nuclear receptor NR2E3 gene mutations distort human retinal laminar architecture and cause an unusual degeneration. *Hum Mol Genet*, *13*(17), 1893–1902. https://doi.org/10.1093/hmg/ddh198

Ji, Q., Bernucci, M. T., Liu, Y., Crowell, J. A., Miller, D. J., & Miller, D. T. (2023). *S-cone identification using AO-OCT cone structural measurements and support vector machine classifier*. https://doi.org/10.1117/12.2650609

Jonnal, R. S., Rha, J., Zhang, Y., Cense, B., Gao, W., & Miller, D. T. (2007). In vivo functional imaging of human cone photoreceptors. *Optics Express*, *15*(24). https://doi.org/10.1364/oe.15.016141

Kellner, U., Zrenner, E., Sadowski, B., & Foerster, M. H. (1993). Enhanced S cone sensitivity syndrome: Long-term follow-up, electrophysiological and psychophysical findings. *Clinical Vision Sciences*, *8*(5).

Kilpeläinen, M., Putnam, N. M., Ratnam, K., & Roorda, A. (2021). The retinal and perceived locus of fixation in the human visual system. *Journal of Vision*, *21*(11). https://doi.org/10.1167/jov.21.11.9

Klug, K., Herr, S., Ngo, I. T., Sterling, P., & Schein, S. (2003). Macaque Retina Contains an S-Cone OFF Midget Pathway. *The Journal of Neuroscience*, *23*(30), 9881–9887. https://doi.org/10.1523/jneurosci.23-30-09881.2003

Krauzlis, R. J., Goffart, L., & Hafed, Z. M. (2017). Neuronal control of fixation and fixational eye movements. *Philosophical Transactions of the Royal Society B: Biological Sciences*, *372*(1718), 20160205.

Krishnan, A. K., & Bedell, H. E. (2018). Functional changes at the preferred retinal locus in subjects with bilateral central vision loss. *Graefe's Archive for Clinical and Experimental Ophthalmology*, *256*(1). https://doi.org/10.1007/s00417-017-3818-3

Kwon, M., Nandy, A. S., & Tjan, B. S. (2013). Rapid and Persistent Adaptability of Human Oculomotor Control in Response to Simulated Central Vision Loss. *Current Biology*, *23*(17), 1663–1669. https://doi.org/https://doi.org/10.1016/j.cub.2013.06.056

Lassoued, A., Zhang, F., Kurokawa, K., Liu, Y., Bernucci, M. T., Crowell, J. A., & Miller, D. T. (2021). Cone photoreceptor dysfunction in retinitis pigmentosa revealed by optoretinography. *Proceedings of the National Academy of Sciences of the United States of America*, *118*(47). https://doi.org/10.1073/pnas.2107444118

Lee, B. B., Martin, P. R., & Valberg, A. (1989). Sensitivity of macaque retinal ganglion cells to chromatic and luminance flicker. *The Journal of Physiology*, *414*(1). https://doi.org/10.1113/jphysiol.1989.sp017685

Lee, S. C., Martin, P. R., & Grünert, U. (2019). Topography of Neurons in the Rod Pathway of Human Retina. *Investigative Opthalmology & Visual Science*, *60*(8), 2848. https://doi.org/10.1167/iovs.19-27217

Lennie, P., & Fairchild, M. D. (1994). Ganglion cell pathways for rod vision. *Vision Research*, *34*(4), 477–482. https://doi.org/10.1016/0042-6989(94)90161-9

Liang, J., Williams, D. R., & Miller, D. T. (1997). Supernormal vision and high-resolution retinal imaging through adaptive optics. *Journal of the Optical Society of America A*, *14*(11), 2884. https://doi.org/10.1364/josaa.14.002884

Lima, V. C., Rosen, R. B., & Farah, M. (2016). Macular pigment in retinal health and disease. In *International Journal of Retina and Vitreous* (Vol. 2, Issue 1). https://doi.org/10.1186/s40942-016-0044-9

Littink, K., Stappers, P., Riemslag, F., Talsma, H., Van Genderen, M., Cremers, F., Collin, R., & Van Den Born, L. (2018). Autosomal Recessive NRL Mutations in Patients with Enhanced S-Cone Syndrome. *Genes*, *9*(2), 68. https://doi.org/10.3390/genes9020068

Litts, K. M., Cooper, R. F., Duncan, J. L., & Carroll, J. (2017). Photoreceptor-Based Biomarkers in AOSLO Retinal Imaging. *Investigative Opthalmology & Visual Science*, *58*(6), BIO255. https://doi.org/10.1167/iovs.17-21868

Lock, T. M., Baizer, J. S., & Bender, D. B. (2003). Distribution of corticotectal cells in macaque. *Experimental Brain Research*, *151*(4). https://doi.org/10.1007/s00221-003-1500-y

Marcos, S., & Navarro, R. (1997). Determination of the foveal cone spacing by ocular speckle interferometry: Limiting factors and acuity predictions. *Journal of the Optical Society of America A*, *14*(4). https://doi.org/10.1364/josaa.14.000731

Marmor, M. F. (1989). Large rod-like photopic signals in a possible new form of congenital night blindness. *Doc Ophthalmol*, *71*(3). https://doi.org/10.1007/bf00170975

Marmor, M. F., Jacobson, S. G., Foerster, M. H., Kellner, U., & Weleber, R. G. (1990). Diagnostic Clinical Findings of a New Syndrome with Night Blindness, Maculopathy, and Enhanced S Cone Sensitivity. *American Journal of Ophthalmology*, *110*(2), 124–134. https://doi.org/10.1016/s0002-9394(14)76980-6

Marmor, M. F., Tan, F., Sutter, E. E., & Bearse Jr., M. A. (1999). Topography of cone electrophysiology in the enhanced S cone syndrome. *Invest Ophthalmol Vis Sci*, *40*(8), 1866–1873. https://www.ncbi.nlm.nih.gov/pubmed/10393063

Marrocco, R. T., & Li, R. H. (1977). Monkey superior colliculus: properties of single cells and their afferent inputs. *Journal of Neurophysiology*, *40*(4). https://doi.org/10.1152/jn.1977.40.4.844

Mazzoni, F., Novelli, E., & Strettoi, E. (2008). Retinal ganglion cells survive and maintain normal dendritic morphology in a mouse model of inherited photoreceptor degeneration. *Journal of Neuroscience*, *28*(52). https://doi.org/10.1523/JNEUROSCI.4968-08.2008

Mears, A. J., Kondo, M., Swain, P. K., Takada, Y., Bush, R. A., Saunders, T. L., Sieving, P. A., & Swaroop, A. (2001). Nrl is required for rod photoreceptor development. *Nature Genetics*, *29*(4), 447–452. https://doi.org/10.1038/ng774

Merigan, W. H., & Maunsell, J. H. R. (1990). Macaque vision after magnocellular lateral geniculate lesions. *Visual Neuroscience*, *5*(4). https://doi.org/10.1017/S0952523800000432

Messias, A., Reinhard, J., Cruz, A. A. V., Dietz, K., MacKeben, M., & Trauzettel-Klosinski, S. (2007). Eccentric fixation in Stargardt's disease assessed by Tübingen perimetry. *Investigative Ophthalmology and Visual Science*, *48*(12). https://doi.org/10.1167/iovs.06-0367

Metha, A. B., & Lennie, P. (2001). Transmission of spatial information in S-cone pathways. *Vis Neurosci*, *18*(6), 961–972. https://doi.org/10.1017/s095252380118613x

Milam, A. H., Rose, L., Cideciyan, A. V, Barakat, M. R., Tang, W. X., Gupta, N., Aleman, T. S., Wright, A. F., Stone, E. M., Sheffield, V. C., & Jacobson, S. G. (2002). The nuclear receptor NR2E3 plays a role in human retinal photoreceptor differentiation and degeneration. *Proc Natl Acad Sci U S A*, *99*(1), 473–478. https://doi.org/10.1073/pnas.022533099

Miller, D. T., & Kurokawa, K. (2020). Cellular-Scale Imaging of Transparent Retinal Structures and Processes Using Adaptive Optics Optical Coherence Tomography. In *Annual Review of Vision Science* (Vol. 6). https://doi.org/10.1146/annurev-vision-030320-041255

Mollon, J. D., & Polden, P. G. (1977). An anomaly in the response of the eye to light of short wavelengths. *Philosophical Transactions of the Royal Society of London. Series B, Biological Sciences*, *278*(960). https://doi.org/10.1098/rstb.1977.0038

Nakamura, P. A., Tang, S., Shimchuk, A. A., Ding, S., & Reh, T. A. (2016). Potential of Small Molecule–Mediated Reprogramming of Rod Photoreceptors to Treat Retinitis Pigmentosa. *Investigative Opthalmology & Visual Science*, *57*(14), 6407. https://doi.org/10.1167/iovs.16-20177

Nolan, J. M., Stringham, J. M., Beatty, S., & Snodderly, D. M. (2008). Spatial profile of macular pigment and its relationship to foveal architecture. *Investigative Ophthalmology and Visual Science*, *49*(5). https://doi.org/10.1167/iovs.07-0933

O'Brien, K. M. B., Cheng, H., Jiang, Y., Schulte, D., Swaroop, A., & Hendrickson, A. E. (2004). Expression of Photoreceptor-Specific Nuclear Receptor NR2E3 in Rod Photoreceptors of Fetal Human Retina. *Investigative Opthalmology & Visual Science*, *45*(8), 2807. https://doi.org/10.1167/iovs.03-1317

Østerberg, G. (1937). Topography of the Layer of Rods and Cones in the Human Retina. *Journal of the American Medical Association*, *108*(3). https://doi.org/10.1001/jama.1937.02780030070033

Pandiyan, V. P., Jiang, X., Kuchenbecker, J. A., & Sabesan, R. (2021). Reflective mirror-based line-scan adaptive optics OCT for imaging retinal structure and function. *Biomedical Optics Express*, *12*(9). https://doi.org/10.1364/boe.436337

Pandiyan, V. P., Maloney-Bertelli, A., Kuchenbecker, J. A., Boyle, K. C., Ling, T., Chen, Z. C., Park, B. H., Roorda, A., Palanker, D., & Sabesan, R. (2020). The optoretinogram reveals the primary steps of phototransduction in the living human eye. *Science Advances*, *6*(37), eabc1124. https://doi.org/10.1126/sciadv.abc1124

Patterson, S. S., Kuchenbecker, J. A., Anderson, J. R., Bordt, A. S., Marshak, D. W., Neitz, M., & Neitz, J. (2019). An S-cone circuit for edge detection in the primate retina. *Scientific Reports*, *9*(1). https://doi.org/10.1038/s41598-019-48042-2

Patterson, S. S., Mazzaferri, M. A., Bordt, A. S., Chang, J., Neitz, M., & Neitz, J. (2020). Another Blue-ON ganglion cell in the primate retina. In *Current Biology* (Vol. 30, Issue 23). https://doi.org/10.1016/j.cub.2020.10.010

Paulun, V. C., Schütz, A. C., Michel, M. M., Geisler, W. S., & Gegenfurtner, K. R. (2015). Visual search under scotopic lighting conditions. *Vision Research*, *113*. https://doi.org/10.1016/j.visres.2015.05.004

Poletti, M., Listorti, C., & Rucci, M. (2013). Microscopic eye movements compensate for nonhomogeneous vision within the fovea. *Current Biology*, *23*(17), 1691–1695. https://doi.org/10.1016/j.cub.2013.07.007

Polyak, S. L. (1941). *The retina.* Univ. Chicago Press.

Prahalad, K. S., & Coates, D. R. (2020). Asymmetries of reading eye movements in simulated central vision loss. *Vision Research*, *171*, 1–10. https://doi.org/https://doi.org/10.1016/j.visres.2020.03.006

Prins, N., & Kingdom, F. A. A. (2018). Applying the Model-Comparison Approach to Test Specific Research Hypotheses in Psychophysical Research Using the Palamedes Toolbox. *Front Psychol*, *9*, 1250. https://doi.org/10.3389/fpsyg.2018.01250

Provis, J. M., Dubis, A. M., Maddess, T., & Carroll, J. (2013). Adaptation of the central retina for high acuity vision: Cones, the fovea and the a vascular zone. *Progress in Retinal and Eye Research*, *35*, 63–81. https://doi.org/10.1016/j.preteyeres.2013.01.005

Putnam, N. M., Hofer, H. J., Doble, N., Chen, L., Carroll, J., & Williams, D. R. (2005). The locus of fixation and the foveal cone mosaic. *Journal of Vision*, *5*(7), 632–639. https://doi.org/10:1167/5.7.3

Redmond, T., Zlatkova, M. B., Vassilev, A., Garway-Heath, D. F., & Anderson, R. S. (2013). Changes in Ricco's area with background luminance in the S-cone pathway. *Optom Vis Sci*, *90*(1), 66–74. https://doi.org/10.1097/OPX.0b013e318278fc2b

Reinhard, J., Messias, A., Dietz, K., MacKeben, M., Lakmann, R., Scholl, H. P. N., Apfelstedt-Sylla, E., Weber, B. H. F., Seeliger, M. W., Zrenner, E., & Trauzettel-Klosinski, S. (2007). Quantifying fixation in patients with Stargardt disease. *Vision Research*, *47*(15). https://doi.org/10.1016/j.visres.2007.04.012

Reiniger, J. L., Domdei, N., Holz, F. G., & Harmening, W. M. (2021). Human gaze is systematically offset from the center of cone topography. *Current Biology*, *31*(18). https://doi.org/10.1016/j.cub.2021.07.005

Ripamonti, C., Aboshiha, J., Henning, G. B., Sergouniotis, P. I., Michaelides, M., Moore, A. T., Webster, A. R., & Stockman, A. (2014). Vision in Observers With Enhanced S-Cone Syndrome: An Excess of S-Cones but Connected Mainly to Conventional S-Cone Pathways. *Invest Ophthalmol Vis Sci*, *55*(2), 963. https://doi.org/10.1167/iovs.13-12897

Rohrschneider, K., Bültmann, S., & Springer, C. (2008). Use of fundus perimetry (microperimetry) to quantify macular sensitivity. In *Progress in Retinal and Eye Research* (Vol. 27, Issue 5). https://doi.org/10.1016/j.preteyeres.2008.07.003

Roman, A. J., Powers, C. A., Semenov, E. P., Sheplock, R., Aksianiuk, V., Russell, R. C., Sumaroka, A., Garafalo, A. V, Cideciyan, A. V, & Jacobson, S. G. (2019). Short-Wavelength Sensitive Cone (S-cone) Testing as an Outcome Measure for NR2E3 Clinical Treatment Trials. *Int J Mol Sci*, *20*(10), 2497. https://doi.org/10.3390/ijms20102497

Roorda, A., & Duncan, J. L. (2015). Adaptive Optics Ophthalmoscopy. *Annual Review of Vision Science*, *1*(1), 19–50. https://doi.org/10.1146/annurev-vision-082114-035357

Roorda, A., Romero-Borja, F., Donnelly Iii, W. J., Queener, H., Hebert, T. J., & Campbell, M. C. W. (2002). Adaptive optics scanning laser ophthalmoscopy. *Optics Express*, *10*(9), 405–412. https://doi.org/10.1364/OE.10.000405

Roorda, A., Sundquist, S., Solovyev, A., Ratnam, K., Lujan, B. J., Stone, E. M., & Duncan, J. L. (2010). Adaptive Optics Imaging Reveals Supernormal Cone Density in Enhanced S-Cone Syndrome. *Invest. Ophthalmol. Vis. Sci*, *51 eAbstract*(13), 2934.

Roorda, A., & Williams, D. R. (1999). The arrangement of the three cone classes in the living human eye. *Nature*, *397*, 520–522. https://doi.org/10.1038/17383

Rose, D., & Bex, P. (2017). Peripheral oculomotor training in individuals with healthy visual systems: Effects of training and training transfer. *Vision Research*, *133*, 95–99. https://doi.org/https://doi.org/10.1016/j.visres.2016.10.016

Rossi, E. A., & Roorda, A. (2010). The relationship between visual resolution and cone spacing in the human fovea. *Nat Neurosci*, *13*(2), 156–157. https://doi.org/10.1038/nn.2465

Rossi, E. A., Weiser, P., Tarrant, J., & Roorda, A. (2007). Visual performance in emmetropia and low myopia after correction of high-order aberrations. *Journal of Vision*, *7*(8), 14. https://doi.org/10.1167/7.8.14

Sabesan, R., Hofer, H., & Roorda, A. (2015). Characterizing the human cone photoreceptor mosaic via dynamic photopigment densitometry. *PLoS ONE*, *10*(12). https://doi.org/10.1371/journal.pone.0144891

Schiller, P. H., & Malpeli, J. G. (1977). Properties and tectal projections of monkey retinal ganglion cells. *Journal of Neurophysiology*, *40*(2). https://doi.org/10.1152/jn.1977.40.2.428

Schleufer, S., Pandiyan, V., Hazelton, B., Coates, D., & Sabesan, R. (2023). Poster Session II: Cone spacing and S-cone proportion is sufficient to describe varying S-cone regularity across the human central retina. *Journal of Vision*, *23*(15), 59. https://doi.org/10.1167/jov.23.15.59

Schleufer, S., Pandiyan, V. P., Bharadwaj, P., & Sabesan, R. (2022). Crystalline arrangement of S-cones in the central human retina. *Investigative Ophthalmology & Visual Science*, *63*(7), 2235 – F0443-2235 – F0443.

Sekiguchi, N., Williams, D. R., & Brainard, D. H. (1993). Efficiency in detection of isoluminant and isochromatic interference fringes. *Journal of the Optical Society of America A*, *10*(10). https://doi.org/10.1364/josaa.10.002118

Shenoy, J., Fong, J., Tan, J., Roorda, A., & Ng, R. (2021). R-SLAM: Optimizing Eye Tracking from Rolling Shutter Video of the Retina. *Proceedings of the IEEE International Conference on Computer Vision*. https://doi.org/10.1109/ICCV48922.2021.00481

Sincich, L. C., Sabesan, R., Tuten, W. S., Roorda, A., & Harmening, W. M. (2016). Functional Imaging of Cone Photoreceptors. In *Human Color Vision*. https://doi.org/10.1007/978-3-319-44978-4_3

Sohn, E. H., Chen, F. K., Rubin, G. S., Moore, A. T., Webster, A. R., & Maclaren, R. E. (2010). Macular Function Assessed by Microperimetry in Patients with Enhanced S-Cone Syndrome. *Ophthalmology*, *117*(6), 1199-1206.e1. https://doi.org/10.1016/j.ophtha.2009.10.046

Stevenson, S. B., Roorda, A., & Kumar, G. (2010). Eye Tracking with the Adaptive Optics Scanning Laser Ophthalmoscope. *Proceedings of the 2010 Symposium on Eye-Tracking Research & Applications*, 195–198. https://doi.org/10.1145/1743666.1743714

Stiles, W. S. (1949). Increment thresholds & the mechanisms of colour vision. *Documenta Ophthalmologica*, *3*(1). https://doi.org/10.1007/BF00162601

Stockman, A., & Sharpe, L. T. (2000). The spectral sensitivities of the middle- and long-wavelength-sensitive cones derived from measurements in observers of known genotype. *Vision Research*, *40*(13). https://doi.org/10.1016/S0042-6989(00)00021-3

Strettoi, E., Mears, A. J., & Swaroop, A. (2004). Recruitment of the Rod Pathway by Cones in the Absence of Rods. *The Journal of Neuroscience*, *24*(34), 7576. https://doi.org/10.1523/JNEUROSCI.2245-04.2004

Stromeyer, C. F., Kronauer, R. E., & Madsen, J. C. (1984). Adaptive processes controlling sensitivity of short-wave cone pathways to different spatial frequencies. *Vision Research*, *24*(8). https://doi.org/10.1016/0042-6989(84)90154-8

Sumner, P., Adamjee, T., & Mollon, J. D. (2002). Signals invisible to the collicular and magnocellular pathways can capture visual attention. *Current Biology*, *12*(15). https://doi.org/10.1016/S0960-9822(02)01020-5

Swanson, W. H. (1996). S-cone spatial contrast sensitivity can be independent of pre-receptoral factors. *Vision Research*, *36*(21). https://doi.org/10.1016/0042-6989(96)00047-8

Swaroop, A., Kim, D., & Forrest, D. (2010). Transcriptional regulation of photoreceptor development and homeostasis in the mammalian retina. *Nat Rev Neurosci*, *11*(8), 563–576. https://doi.org/10.1038/nrn2880

Szél, Á., Van Veen, T., & Röhlich, P. (1994). Retinal cone differentiation. *Nature*, *370*(6488), 336. https://doi.org/10.1038/370336a0

Thibos, L. N., Cheney, F. E., & Walsh, D. J. (1987). Retinal limits to the detection and resolution of gratings. *J Opt Soc Am A*, *4*(8), 1524–1529. https://doi.org/10.1364/josaa.4.001524

Timberlake, G. T., Sharma, M. K., Grose, S. A., Gobert, D. V., Gauch, J. M., & Maino, J. H. (2005). Retinal location of the preferred retinal locus relative to the fovea in scanning laser ophthalmoscope images. *Optometry and Vision Science*, *82*(3). https://doi.org/10.1097/01.opx.0000156311.49058.c8

Tuten, W. S., & Harmening, W. M. (2021). Foveal vision. *Current Biology*, *31*(11), R701–R703. https://doi.org/10.1016/j.cub.2021.03.097

Tuten, W. S., Tiruveedhula, P., & Roorda, A. (2012). Adaptive Optics Scanning Laser Ophthalmoscope-Based Microperimetry. *Optometry and Vision Science*, *89*(5), 563–574. https://doi.org/10.1097/opx.0b013e3182512b98

Upadhyay, A. K., Datta, S., Brabbit, E., Love, Z., Haider, N. B., & Arumugham, R. (2020). Preclinical efficacy of AAV5-Nr2e3 in the mouse model of Nr2e3 mutation associated inherited retinal degeneration. *Investigative Ophthalmology & Visual Science*, *61*(7), 4466.

Verdina, T., Greenstein, V. C., Sodi, A., Tsang, S. H., Burke, T. R., Passerini, I., Allikmets, R., Virgili, G., Cavallini, G. M., & Rizzo, S. (2017). Multimodal analysis of the Preferred Retinal Location and the Transition Zone in patients with Stargardt Disease. *Graefe's Archive for Clinical and Experimental Ophthalmology*, *255*(7). https://doi.org/10.1007/s00417-017-3637-6

Wald, G. (1967). Blue-blindness in the normal fovea. *Journal of the Optical Society of America*, *57*(11). https://doi.org/10.1364/JOSA.57.001289

Wang, Y., Bensaid, N., Tiruveedhula, P., Ma, J., Ravikumar, S., & Roorda, A. (2019). Human foveal cone photoreceptor topography and its dependence on eye length. *Elife*, *8*. https://doi.org/10.7554/elife.47148

Wang, Y., Wang, C., Ng, R., & Tuten, W. S. (2023). Contributed Session II: High-resolution assessment of saccadic landing positions for S-cone-isolating targets. *Journal of Vision*, *23*(15), 74. https://doi.org/10.1167/jov.23.15.74

Wang, Y., Vu, B. T., Wang, C., Ng, R., & Tuten, W. S. (2023). Preferred Retinal Locus of Fixation in the S-cone Pathway. *Investigative Ophthalmology & Visual Science*, *64*(8), 468.

Wang, Y., Wong, J., Duncan, J. L., Roorda, A., & Tuten, W. S. (2023a). Enhanced S-cone Syndrome, a Mini-review. In *Advances in Experimental Medicine and Biology* (Vol. 1415). https://doi.org/10.1007/978-3-031-27681-1_28

Wang, Y., Wong, J., Duncan, J. L., Roorda, A., & Tuten, W. S. (2023b). Enhanced S-Cone Syndrome: Elevated Cone Counts Confer Supernormal Visual Acuity in the S-Cone Pathway. *Investigative Ophthalmology and Visual Science*, *64*(10). https://doi.org/10.1167/iovs.64.10.17

Watson, A. B., & Pelli, D. G. (1983). QUEST: a Bayesian adaptive psychometric method. *Percept Psychophys*, *33*(2), 113–120. https://doi.org/10.3758/bf03202828

White, B. J., Kerzel, D., & Gegenfurtner, K. R. (2006). Visually guided movements to color targets. *Experimental Brain Research*, *175*(1), 110–126. https://doi.org/10.1007/s00221-006-0532-5

White, J. M., & Bedell, H. E. (1990). The oculomotor reference in humans with bilateral macular disease. *Investigative Ophthalmology & Visual Science*, *31*(6), 1149–1161.

Whitehead, A. J., Mares, J. A., & Danis, R. P. (2006). Macular pigment: A review of current knowledge. In *Archives of Ophthalmology* (Vol. 124, Issue 7). https://doi.org/10.1001/archopht.124.7.1038

Wilk, M. A., Dubis, A. M., Cooper, R. F., Summerfelt, P., Dubra, A., & Carroll, J. (2017). Assessing the spatial relationship between fixation and foveal specializations. *Vision Research*, *132*, 53–61. https://doi.org/https://doi.org/10.1016/j.visres.2016.05.001

Wilkinson, M. O., Anderson, R. S., Bradley, A., & Thibos, L. N. (2020). Resolution acuity across the visual field for mesopic and scotopic illumination. *Journal of Vision*, *20*(10), 7. https://doi.org/10.1167/jov.20.10.7

Williams, D. R., & Coletta, N. J. (1987). Cone spacing and the visual resolution limit. *Journal of the Optical Society of America A*, *4*(8). https://doi.org/10.1364/josaa.4.001514

Williams, D. R., MacLeod, D. I. A., & Hayhoe, M. M. (1981a). Punctate sensitivity of the blue-sensitive mechanism. *Vision Research*, *21*(9). https://doi.org/10.1016/0042-6989(81)90242-X

Williams, D. R., MacLeod, D. I., & Hayhoe, M. M. (1981b). Foveal tritanopia. *Vision Res*, *21*(9), 1341–1356. https://doi.org/10.1016/0042-6989(81)90241-8

Willmer, E. N. (1944). Colour of small objects [6]. In *Nature* (Vol. 153, Issue 3895). https://doi.org/10.1038/153774b0

Willmer, E. N., & Wright, W. D. (1945). Colour sensitivity of the fovea centralis. *Nature*, *156*(3950). https://doi.org/10.1038/156119a0

Wool, L. E., Packer, O. S., Zaidi, Q., & Dacey, D. M. (2019). Connectomic Identification and Three-Dimensional Color Tuning of S-OFF Midget Ganglion Cells in the Primate Retina. *J Neurosci*, *39*(40), 7893–7909. https://doi.org/10.1523/JNEUROSCI.0778-19.2019

Xiao, M., & Hendrickson, A. (2000). Spatial and temporal expression of short, long/medium, or both opsins in human fetal cones. *J Comp Neurol*, *425*(4), 545–559. https://www.ncbi.nlm.nih.gov/pubmed/10975879

Xu, H., & Tian, N. (2004). Pathway-Specific Maturation, Visual Deprivation, and Development of Retinal Pathway. *The Neuroscientist*, *10*(4), 337–346. https://doi.org/10.1177/1073858404265254

Yuodelis, C., & Hendrickson, A. (1986). A qualitative and quantitative analysis of the human fovea during development. *Vision Research*, *26*(6). https://doi.org/10.1016/0042-6989(86)90143-4

Yzer, S., Barbazetto, I., Allikmets, R., van Schooneveld, M. J., Bergen, A., Tsang, S. H., Jacobson, S. G., & Yannuzzi, L. A. (2013). Expanded clinical spectrum of enhanced S-cone syndrome. *JAMA Ophthalmol*, *131*(10), 1324–1330. https://doi.org/10.1001/jamaophthalmol.2013.4349

Zhang, C., Kim, Y. J., Silverstein, A. R., Hoshino, A., Reh, T. A., Dacey, D. M., & Wong, R. O. (2020). Circuit Reorganization Shapes the Developing Human Foveal Midget Connectome toward Single-Cone Resolution. *Neuron*, *108*(5), 905-918.e3. https://doi.org/10.1016/j.neuron.2020.09.014

Zhang, F., Kurokawa, K., Lassoued, A., Crowell, J. A., & Miller, D. T. (2019). Cone photoreceptor classification in the living human eye from photostimulation-induced phase dynamics. *Proceedings of the National Academy of Sciences*, *116*(16), 7951–7956. https://doi.org/10.1073/pnas.1816360116

Zlatkova, M. B., Coulter, E., & Anderson, R. S. (2003). Short-wavelength acuity: blue-yellow and achromatic resolution loss with age. *Vision Res*, *43*(1), 109–115. https://doi.org/10.1016/s0042-6989(02)00411-x